8-2015

Model Based Combustion Phasing Control for High Degree of Freedom Spark-Ignition Engines

Shu Wang
Clemson University

MODEL BASED COMBUSTION PHASING CONTROL FOR HIGH DEGREE OF FREEDOM SPARK-IGNITION ENGINES

A Dissertation
Presented to
the Graduate School of
Clemson University

In Partial Fulfillment
of the Requirements for the Degree
Doctor of Philosophy
Automotive Engineering

---

by
Shu Wang
August 2015

Accepted by:
Dr. Robert Prucka, Committee Chair
Dr. Zoran Filipi, Co-Chair
Dr. Pierluigi Pisu
Dr. Hussein Dourra

ABSTRACT

With more restrictive engine emissions regulations and higher energy prices, the modern engine is equipped with an increasing number of actuators to meet the fuel economy, drivability and emissions requirements. Although map-based engine control and calibration routines are state of the art, they become burdensome when the number of control degrees of freedom increases significantly. The increased system complexity motivates the use of model-based methods to minimize product development time and ensure calibration flexibility when the engine is altered during the design process. Model-based control has the potential to significantly reduce the labor, time and expense of engine calibration, as compared to state-of-the-art experimentally based methods.

In this research, physics-based models designed for real-time SI engine combustion phasing prediction and control are proposed. To realize real-time implementation of this system several models are derived; (1) a physics based internal residual gas mass prediction model, (2) a real-time cylinder pressure calculation model, (3) a two-step physics based turbulence intensity model, (4) a flame kernel development prediction model, and (5) a spark selection algorithm are subsequently developed. The complete physical models based combustion phasing prediction and control system are implemented into a rapid prototype ECU to realize real-time engine tests. Steady-state and transient engine test results show that the proposed system can accurately predict key variables and control the SI engine combustion phasing in real-time. The root-mean-square-error (RMSE) of the combustion phasing control over a wide range of operating conditions is 2-3 crank angle degrees.

ACKNOWLEDGMENTS

It is not possible to recognize all of the people who have made significant contributions to my research. I would like to acknowledge Professor Robert Prucka and Professor Zoran Filipi of the Clemson University International Center for Automotive Research. Their guidance and support throughout this process has significantly enhanced my life, professionally and personally. I truly thank them for providing me the opportunity to pursue my automotive engineer dream. I really appreciate the kind support and help from Dr. Baitao Xiao. His suggestions helped me quickly get involved in this project. I am also very thankful for David Mann, Gary Mathis and Frank Webb who helped me smoothly and efficiently completed my experimental tests.

Funding and technical support for this dissertation was provided by the Fiat Chrysler Automobiles. Specifically, I would like to thank Michael Prucka and Dr. Hussein Dourra of Fiat Chrysler Automobiles. Without their exceptional guidance and expertise, this project would not have been possible.

My team mates and friends have given invaluable support and encouragement. They have provided me with a great deal of motivation and energy, and I am very appreciative of their kindness. Finally, I am especially grateful to my family for their unconditional support and understanding throughout this difficult process. Go Tigers!

TABLE OF CONTENTS

Page

Table of Contents (Continued)

Page

LIST OF TABLES

LIST OF FIGURES

List of Figures (Continued)

Figure Page

List of Figures (Continued)

List of Figures (Continued)

Figure Page

List of Figures (Continued)

Figure Page

List of Figures (Continued)

List of Figures (Continued)

Figure Page

CHAPTER ONE

INTRODUCTION

1.1 The Importance of SI Engine Combustion Phasing Control

Combustion phasing is normally described by the mass burned fraction as a function of crank angle (Figure 1). There are several special points in the mass burned fraction curve, such as spark timing, CA10 (the 10% mass burned crank angle location), CA50 and CA90 [1]. Among them, CA50 is always of primary interest for the engine combustion analysis and control. It has often been used as the control target parameter (for example, keep CA50 around 6-10degATDC to reach maximum break torque (MBT) point). Spark timing is the primary actuator used to adjust the relative crank angle location of the combustion event. For example, advancing the spark timing will make the combustion event occur earlier and CA50 will advance on a crank angle basis.

Combustion phasing directly affects engine thermal efficiency and output torque [2-4]. Figure 2 shows the normalized engine efficiency and output torque as a function of CA50. For the CA50 sweep, there will be a point called MBT (CA50 around 8 deg ATDC in Figure 2) where the engine thermal efficiency and torque reach a maximum. Advancing the spark from MBT leads to higher heat transfer loss, and the expansion loss will increase with retarded spark. For the best fuel economy and torque output, it is desirable to control the engine combustion phasing as close to MBT as possible.

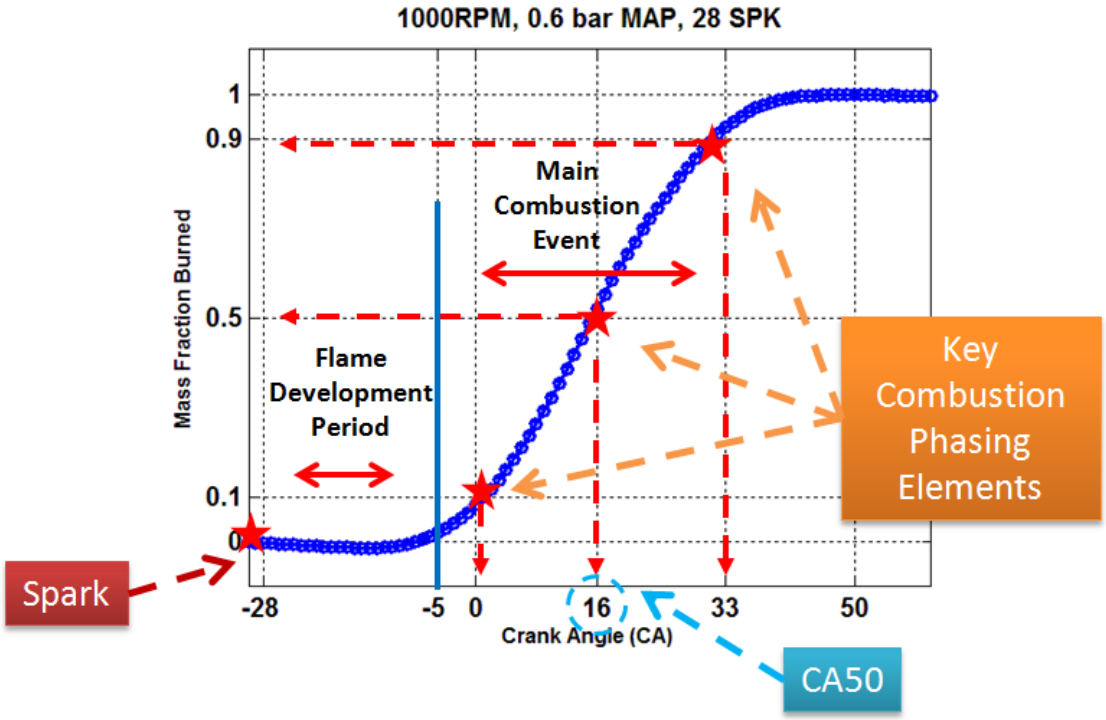

Figure 1: Combustion phasing control description

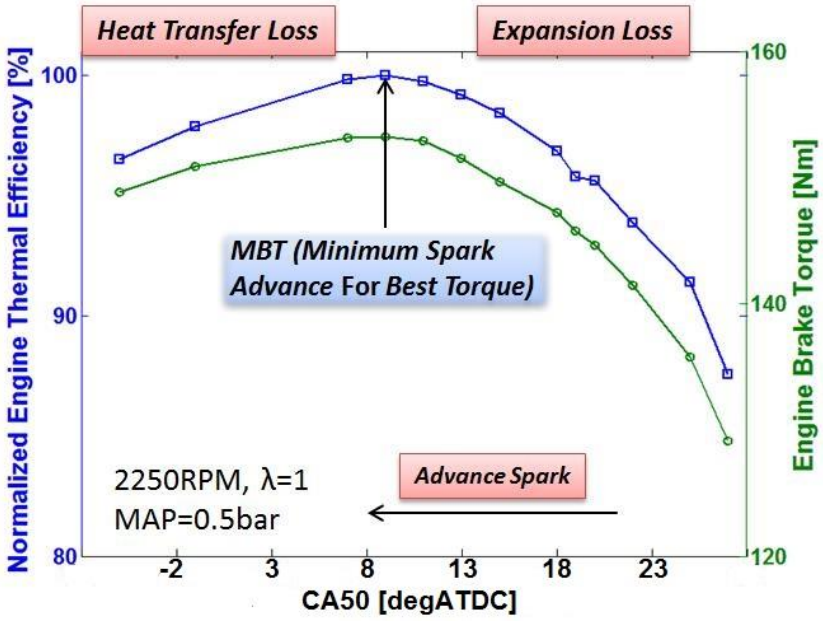

Figure 2: Combustion phasing effect on engine thermal efficiency and output torque

At some circumstances, like engine cold start, fuel economy is not the primary concern. Instead, reducing exhaust pollution is more critical [2,4-7]. To heat the catalyst to working temperatures faster, the combustion phasing is often retarded to produce higher exhaust gas temperatures. Possible side effects of late combustion phasing are increased cycle-by-cycle combustion variation and exhaust temperature induced catalyst damage (Figure 3).

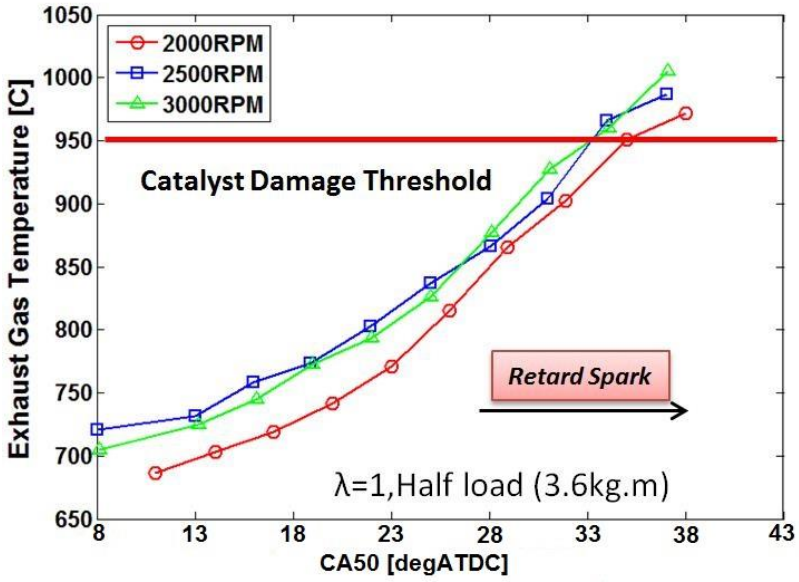

Figure 3: Combustion phasing effect on exhaust gas temperature

Combustion phasing also affects engine-out NO and HC concentration (Figure 4). Late combustion phasing reduces NO and HC (but too extensive spark retard might cause unstable combustion and increase HC concentration).

Combustion phasing has a strong relationship with engine knock and combustion stability [8-10]. Figure 5 shows the achievable CA50 with knock limitation. For some engine operation conditions, the combustion phasing cannot be advanced to MBT due to

knock limitations. Retarding combustion phasing will lead to the increasing of COV of IMEP which represents cycle-by-cycle variation (Figure 6).

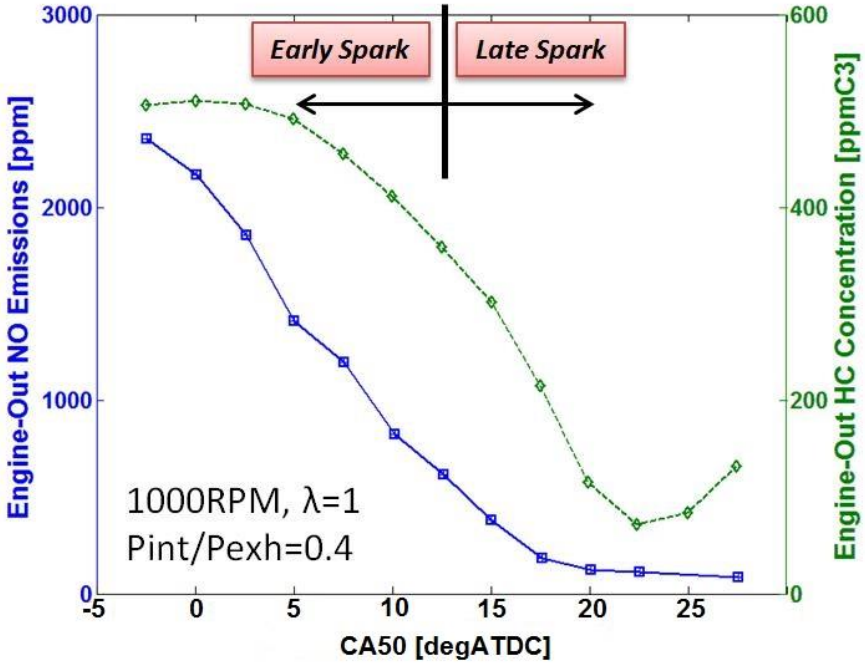

Figure 4: Combustion phasing effect on engine-out emissions

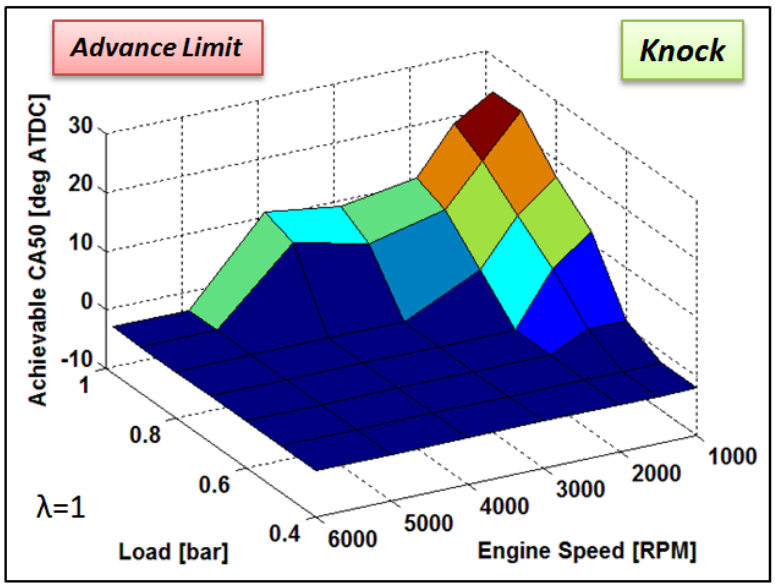

Figure 5: Combustion phasing relationship with engine knock

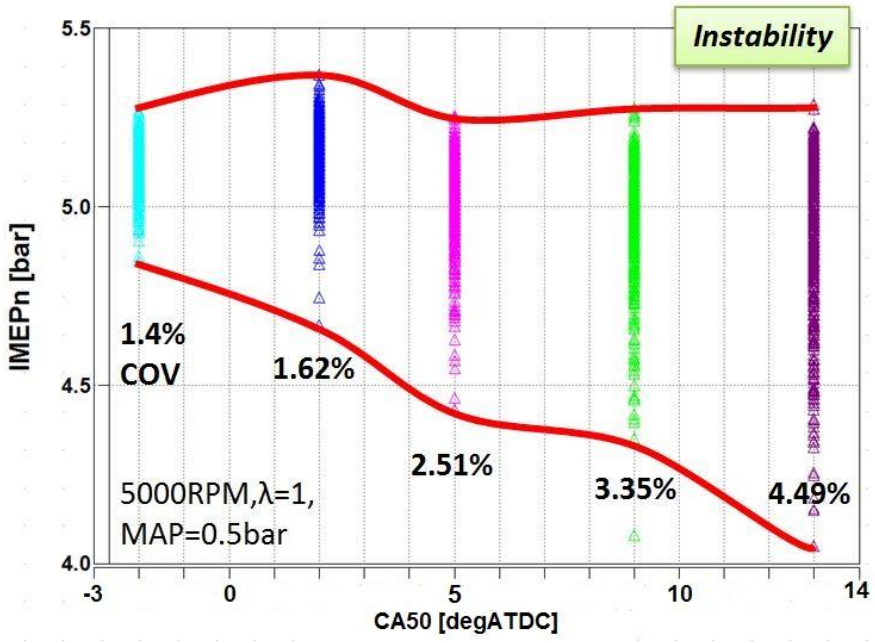

Figure 6: Combustion phasing influence on cycle-by-cycle combustion variation

From the above, the combustion phasing is critical to meet the requirements for fuel economy, emissions regulation, drivability and engine durability. Accurately controlling combustion phasing is a major focus for spark-ignition engines.

Fuel efficiency and emissions regulations stimulate development of spark-ignition (SI) engines that incorporate a large number of control actuators, like variable valve timing, external EGR, charge motion control valves, etc. Calibration and control of modern SI engines with an increasing number of actuators becomes more difficult due to significantly increased actuator set point combinations for a given engine operating condition. For these applications map-based calibration and control strategies become cumbersome, since their complexity increases significantly when control actuators are added to the system. Additionally, more actuators make transient calibration and control

more difficult. All of these considerations pave the way for model-based engine control algorithm development.

1.2 The Combustion Phasing Control Challenge

For the SI engine, spark timing is the last control actuator before combustion to affect combustion phasing. Proper ignition timing is extremely critical for combustion phasing, and it consequently decides fuel economy, emissions and engine durability [1-10]. For a given operating point, the proper spark timing is a strong function of all other actuator positions and this makes the spark timing prediction difficult, especially for the transient engine operation conditions.

The state of the art combustion phasing (spark timing) control methods use map-based feed forward algorithms [11-15]. Feedback loop is incorporated to back off timing if knock is detected. The map based methods us a design of experiments or full factorial map calibration based purely on experimental testing [13-14]. Test engines are operated under specific operating conditions to find out what is the proper spark timing for the engine control requirement. This method is accurate and no model is needed, but labor, testing time and cost increases exponentially with higher degree of freedom engines. A more efficient calibration method incorporates engine data-driven models with experimental testing [15-16]. An example model based calibration system is shown in Figure 7.

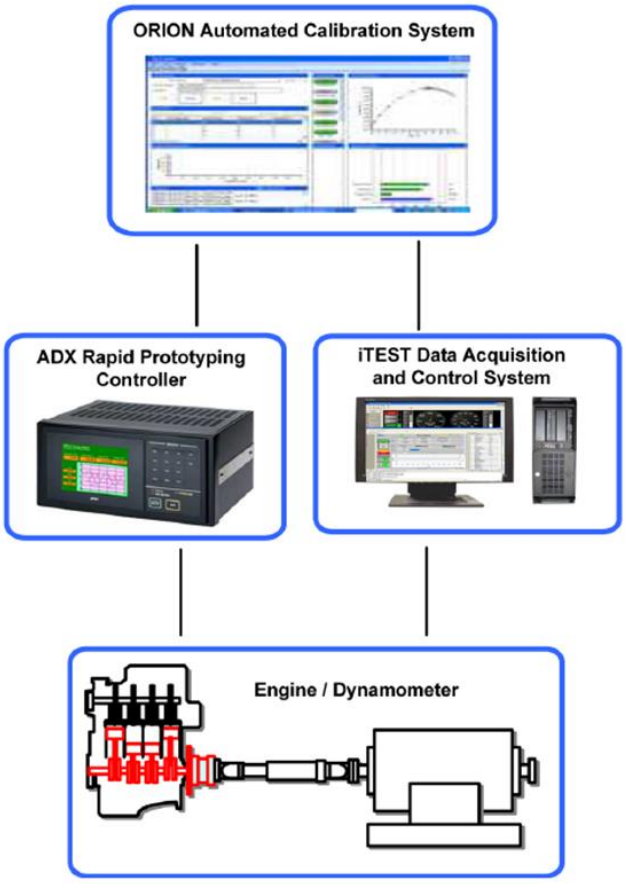

Figure 7: Model based calibration system

At the beginning of model based calibration, the engine factors and responses are defined and then the design of experiment (DoE) tool determines engine test points. The next step is the engine experiment execution to obtain the required engine test data. The last and the most important step is the statistical modeling. The engine test data are used to create the optimum control maps for the engine combustion phasing control. Compared with full factorial map calibration, the model based calibration method is faster. However, model-based calibration can still be cumbersome when applied to more

complex engine systems. Moreover, for transient control, a large amount of compensation maps are still needed and this is time and labor intensive.

Another combustion phasing control option is to use feedback based on combustion sensors (generally using cylinder pressure or ionization measurements) [17-21]. Then the measured combustion phasing value is compared with the target value to calculate the error which will be compensated by changing engine actuator settings (like spark timing).

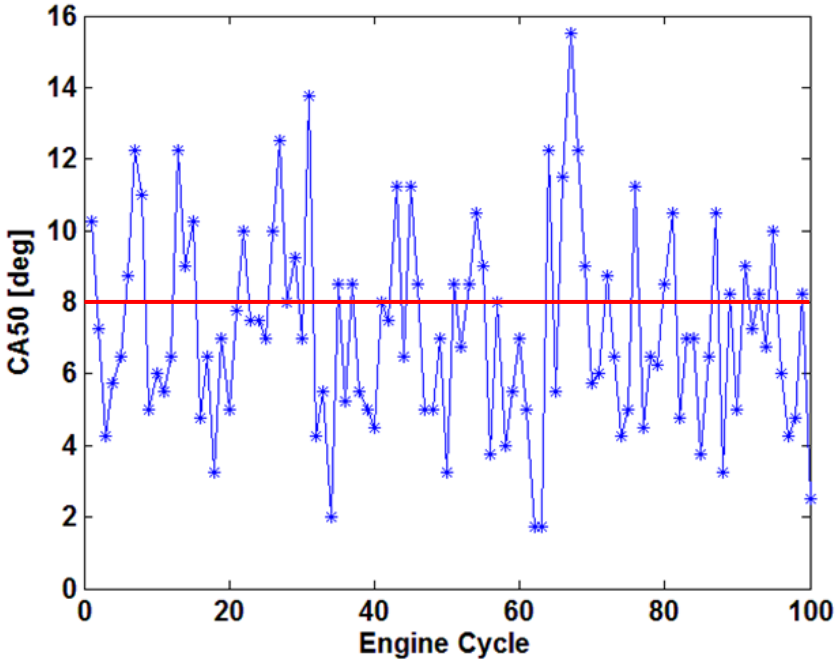

Figure 8: CA50 values for 100 consecutive engine cycles under a constant spark timing

There are several ways to measure the combustion phasing, for example cylinder pressure, ionization signal and etc. However, feedback combustion phasing control method has several shortcomings. First, there is additional expense associated with added sensors. The accuracy and robustness of the sensor signal can also be a concern.

Moreover, feedback control suffers from its delayed response characteristic. This might be acceptable for constant engine operation conditions, but during the transient operation a one-cycle delay can cause significant combustion phasing error. Figure 8 shows measured CA50 values for 100 consecutive engine cycles under a constant operation conditions. The average of the CA50 is about 7~8 degrees ATDC, but for each engine cycle CA50 randomly distributes around the average value.

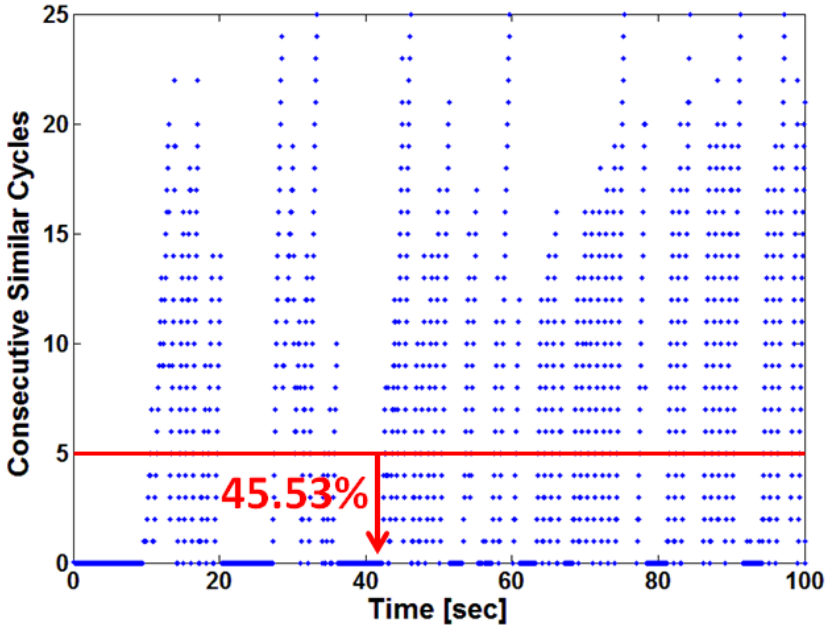

Figure 9: Consecutive similar engine cycles for the first 100 sec of UDDS driving cycle. 45% of engine cycles have five or fewer similar engine cycles directly preceding them, putting great emphasis on feed-forward spark timing control.

Combustion variation makes feedback control difficult since only one or two engine cycles are insufficient for the accurate combustion phasing prediction. This is amplified in transient conditions because the combustion phasing changes a lot under varying operation conditions. In the real world operation the engine is almost always

operated transiently [22]. Figure 9, shows drive-cycle simulation results from GT-Power. The figure plots consecutive ‘similar’ engine cycles for first 100 seconds of a UDDS driving cycle. Similar engine cycles are defined as and IMEP difference less than 5%. As mentioned above, feedback combustion phasing control requires several consecutive engine cycles’ results to determine a mean value. In Figure 9 around 45 percent of the all cycles are stable for less than five consecutive combustion events, making feedback combustion phasing control difficult to realize for a large portion of real-world operation.

1.3 Background Review

1.3.1 Proposed Combustion Phasing Control Algorithm and Combustion Model Selection

Figure 10 shows the proposed feed-forward physics-based combustion phasing control algorithm for this research. The inputs into the system are engine speed, manifold pressure, valve timings and ambient air temperature from existing engine sensors, and no more additional sensors are needed. Instead, models of physical processed will allow prediction of combustion duration. For this research, the actuator for the combustion phasing control is chosen as the spark timing, which is the last control actuator set prior to the combustion event.

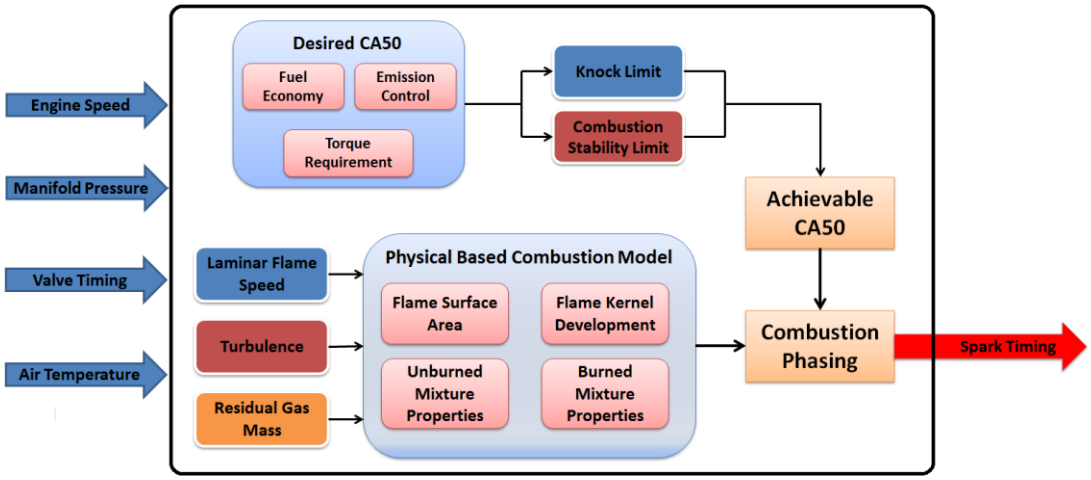

Figure 10: Control algorithm of the feed forward physical model based combustion phasing control strategy

The most critical part in this control system is the combustion duration prediction, which is calculated from the physics-based combustion model. The physics-based laminar flame speed, turbulence intensity and residual gas mass models will be the primary inputs models to the combustion model. Additionally, the flame surface area, flame kernel development prediction and mixture properties are critical for the combustion model itself.

Once the combustion duration/phasing is calculated the specific combustion phasing point, for this research CA50, is required to back predict the proper spark timing. Here, in this system, this point is called as achievable CA50. It is different from the desired CA50 due to engine knock and combustion stability limitations. The reality is that sometimes, e.g. low speed and high engine load, though the fuel economy oriented combustion phasing control might command to put the CA50 at MBT (Maximum Brake Torque), but engine knock will prevent the spark timing from reaching the MBT point.

Another example is engine cold start: the combustion phasing should be retarded to increase catalyst temperature and facilitate light-off, but too much retard will make the combustion highly variable or even generate misfire. Because of these reasons (and others) CA50 cannot always reach the desired position for best fuel economy.

The desired CA50 is decided based on the fuel economy, emission regulations and special engine torque requirements. Fuel economy considerations, favor running the engine at MBT timing. However, combustion at MBT might not bring out the best emissions. As a result, the fuel economy has to give its way to emission reduction at times. The special torque requirement might occur when an immediate torque change is needed. For instance, to realize better gear shifting, engine torque needs to match the requirement quickly and the combustion phasing could fulfill this requirement as mentioned in the previous sections. There are more examples, such as vehicle stability control and so on. Under these circumstances, neither of the fuel consumption and emission reduction is the primary concern. Instead, engine torque output becomes non-negotiable and it in turn decides combustion phasing.

As a critical part in the model based combustion phasing control system, combustion models are applied to represent the mixture reaction rates in the cylinder, capture abnormal combustion phenomenon (i.e. knock) and predict the formation of emissions. Different types of combustion models have been implemented into engine simulations. They could be categorized as 0D, quasi-D, 1D and 3D combustion models based on their computational power requirements and model predictive ability as shown in Figure 11.

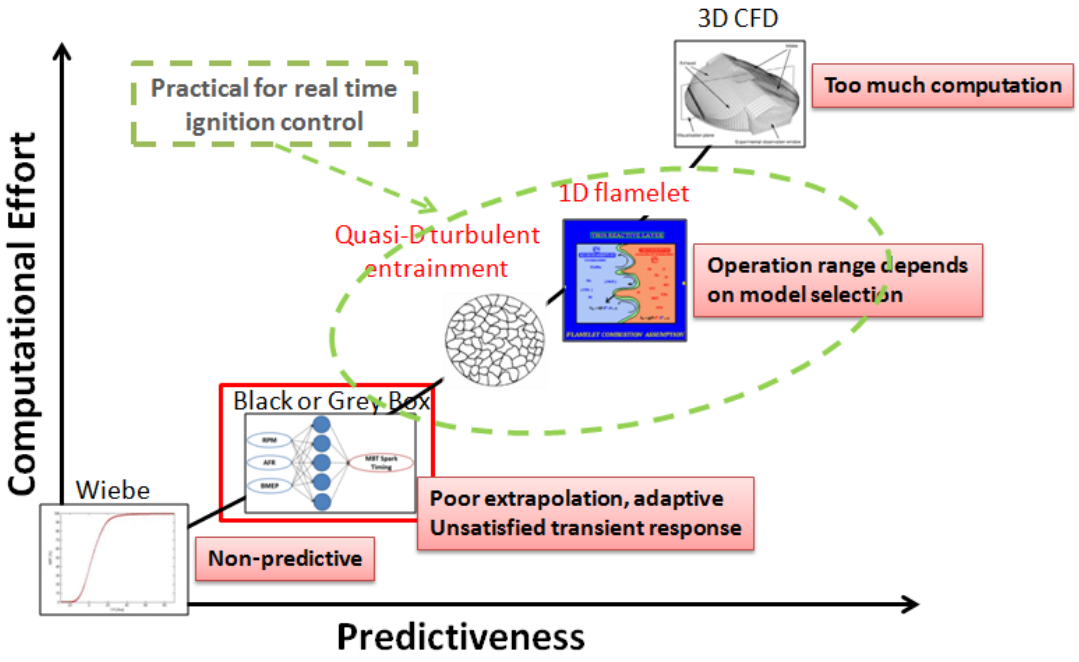

Figure 11: Combustion model classification and their predictiveness and computational effort

The Wiebe function [23-24] can be seen as a 0D combustion model. It utilizes critical combustion phasing points during the combustion process, like start of combustion, CA50, CA90, etc., and experimentally fit required coefficients to build up an equation that represents the mass burn rate during engine combustion process. It is the simplest combustion model and could be implemented into the 0-D engine simulation with time as the only independent variable. However, the predictive ability of the model is extremely limited due to its empirical based nature. To reduce the requirement for a large set of calibration data, researchers provided a method to predict parameters in Wiebe function based on the existing correlations of the laminar burning velocity. By comparing the relative change of the estimated laminar burning velocity at spark timing, the parameter changes in Wiebe function could be predicted [25]. However, as a totally empirical based combustion model without any physical meaning, the Wiebe function

cannot be applied to predict engine combustion process. Another type of fully empirical based combustion model is called Neural Network (NN) or Black Box based combustion model. NNs are trained based on the experiment data to set up the relationships between given inputs and outputs. The outputs of the NN applied to combustion model could be combustion duration [26-27], emissions [28-29] and etc. The shortcoming of the NN or other methods using complex equation fitting do not allow flexibility to make adjustments to a single aspect without completely retraining the model. To change this situation, researchers proposed semi-physical neural networks or grey box combustion models [30][31]. These models combine physics with neural networks (or black box) to increase the adaptive ability of the semi-physical combustion models.

The quasi-dimensional combustion model offers an opportunity to break away from semi-empirical models and admire predictiveness. The well-known and widely used approach for SI combustion is the turbulent flame entrainment combustion model, which is firstly proposed by Keck [32-33] and modified by Tabaczynski [34-35].The model assumes that fresh gas eddies are entrained in a spherical flame front and burn in a characteristic time [1-2][39-40]. During the turbulent entrainment process, the mass entrainment rate is decided by the unburned gas density, the flame front area, the laminar flame speed and the turbulence intensity. The burn-up rate within the reaction zone is affected by the entrained and the burned gas mass, the laminar flame speed and the Taylor micro-scale. The quasi-dimensional combustion model, it incorporates mixture flow parameters and geometrical aspects of the flame front interaction with the combustion chamber within the 0-D framework. The model is used for analysis and

engine design, but the new challenge is to realize the real-time calculation. The accuracy and adaptive ability of the combustion model depend on sub-models.

For the stratified SI engine combustion modeling, a new quasi-dimensional combustion calculation is proposed [41]. It is derived from the two-zone entrainment model. But due to the insufficient of two-zone treatment describing the inhomogeneous air/fuel composition, there are four unburned zones defined: a rich zone, a stoichiometric zone, a lean zone and a remaining air zone. Like the existing method, the burned zone is defined and all these zones are connected to each other by the calculated mixture mass flow rates. The mixture model considered the current geometry of the zones and the flame propagation was developed to fulfill the stratified combustion process. In [42], to predict the mass burning rates, a quasi-dimensional combustion model is proposed, which is based on flame stretch concepts and turbulent entrainment theory. The flame stretch sub-model assesses the flame response to combined effects of turbulent strain, curvature and non-unity Lewis number mixture. This model can be used to simulate the early flame development, flame propagation and flame termination periods. It does not consider the spark ignition processes and neglects the flame kernel formation. To better capture the detailed flame front shape, a 1D coherent flame model (CFM) combustion model is developed [43]. It is a 1D physical based combustion model for gasoline engine transient application. This CFM-1D model is simplified from the 3D CFD model (ECFM) for gasoline combustion [44]. For the CFM model, there are two zones in the combustion chamber: unburned and burned zones. The two zones are separated by a premixed turbulent flame front which is modeled by using a 1D adaptation of the 3D flame surface

density method. The chemical reactions happen in a very thin layer called flamelet. For this simplified 1D CFM model, there are some assumptions: mixture is homogenous, mixture is perfect gases (fresh air, fuel vapor and burned gases), stoichiometric combustion and there is no dependency on different variables space and the cylindrical combustion chamber. Its application to study gasoline engine transient operation has been demonstrated in [43] to achieve increased fidelity.

For the three dimensional combustion models, in [42][45], an improved DPIK model and G-equation combustion model are proposed. The flame kernel position is tracked by particles and the turbulent flow influences on the turbulent flame during combustion are concerned. The G-equation combustion model was modified and implemented into 3D code KIVA-3V. The G-equations (level set method) can track the propagation of the mean turbulent flame. To model the chemical reaction within the cells reacting, the flame surface density, the mean turbulent flame and the turbulent burning velocity are considered. But the detailed turbulent flame is ignored and species in cells in the burned gas behind the mean flame front location are assumed to be in chemical equilibrium. To decrease the computational efforts, the fine numerical resolution was found to be unnecessary, and the narrow band concept of Chopp [46] was applied. In [47], a universal engine combustion model called the GAMUT (G-equation for All Mixtures. A Universal Turbulent) is proposed. This methodology can be applied to premixed and non-premixed combustion regimes and partially premixed combustion. The level set method (G-equation) is a very powerful numerical technology that can be applied to analyze and compute interface motions. The application examples are the

shape recovery, the crystal growth calculation, two-phase flow, image processing and combustion [48]. Williams introduced the method to describe the flame propagation for a premixed air-fuel mixture in 1985. In this model, G-equations are applied to track the premixed turbulent flame propagation (e.g., for premixed and partially premixed combustion). The diffusion combustion which happens behind the premixed flame branched was modeled by using a modified characteristic time scale model. Combined with the Shell auto-ignition model, this model can be used to simulate premixed and diffusion combustion processes for the diesel combustion. A new three-zone combustion model was proposed to provide better correspondence of the numerical calculated results to the experimental data in a wide range of operation parameters for engines with different engine geometries [49]. The additional third zone is used for the simulation of the processes in the flame kernel volume inside the spark plug gap. It captures the detailed mechanism of chemical and thermal ionization interaction, heat transfer between electrodes and combustion products and the mass exchange between in-cylinder combustion products and the third zone. This three-zone model seems more adequate to simulate the real process of SI engine combustion. Chemical kinetics method for the simulation of combustion and behavior of combustion products in all zones gives a chance to accurately analyze the ionization process and confirm the two peaks of ion current.

Among all available SI combustion models, the quasi-dimensional turbulent flame entrainment model and 1D CFM are agreed to be most practical models for real time

control. They are able to capture the effect of key physical parameters of SI combustion, while offering a promise of real-time execution on modern ECU hardware.

1.3.2 Challenges and Approach

For the real-time engine combustion phasing control, the main challenge is the tradeoff between combustion phasing prediction accuracy and model complexity. As described above, the quasi-dimensional turbulent flame entrainment combustion model has the potential to realize real-time application. However, the accuracy of inputs to this combustion model significantly affects the combustion rate calculation accuracy. For example, the most important physical inputs for SI engine combustion are laminar flame speed and turbulence intensity. They significantly affect the flame entrainment process, the unburned gas burning speed and the flame front area wrinkling. At the same time, the flame kernel development process is a difficult area to accurately represent with simplified models. In order to realize the real-time engine combustion phasing prediction, accurate and control-oriented input models are required. To implement the real-time engine combustion phasing prediction, in this research, physics based control-oriented inputs models are developed and separately validated (shown in the following sections) and the combination of all the models are organized based on the proposed combustion phasing prediction algorithm.

Besides combustion phasing prediction, the combustion phasing control itself also remains a challenge. Due to the complexity of the physics based combustion phasing prediction system, it is very difficult to inverse all the models to determine spark timing based on a combustion phasing target. Instead, the spark timing determination needs to

depend on some test and trial methods. In this research, an efficient and accurate spark selection algorithm is proposed to realize the combustion phasing control.

1.4 Dissertation Outline

Figure 12 is an outline of the physics-based combustion phasing prediction and control system. This document describes each of the critical models, the processes to implement this combustion phasing prediction/control system in real-time engine, and provides validation results. This document is composed of nine chapters.

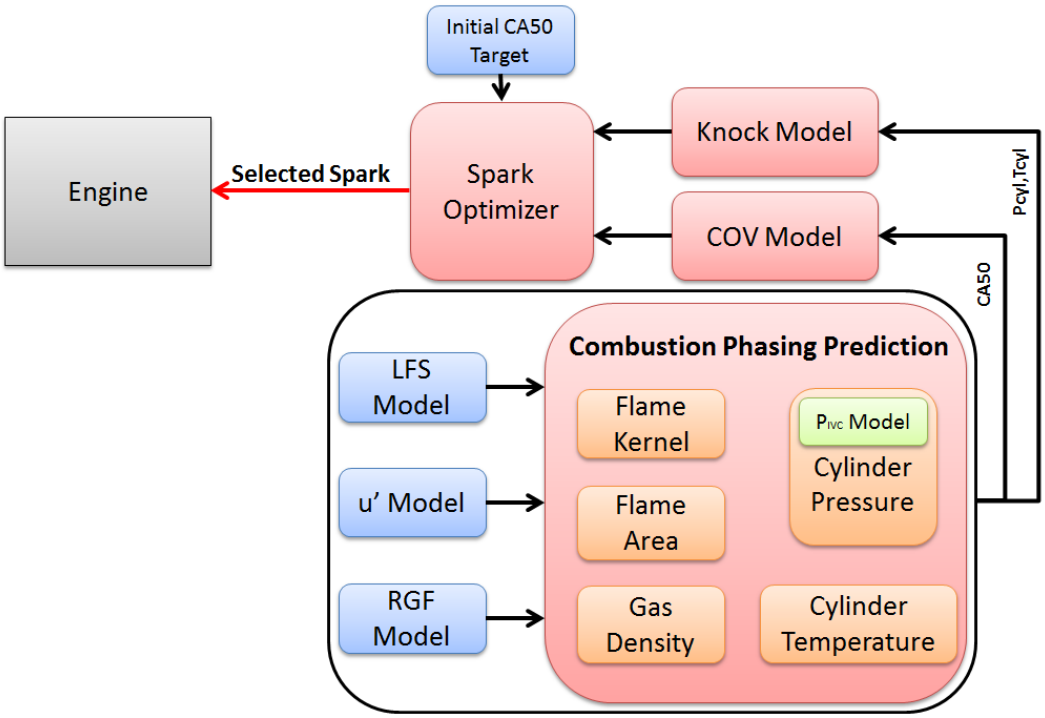

Figure 12: Outline of the physics-based combustion phasing prediction and control system

Chapter 1 presents the motivation for this research and introduces the background of the physics based combustion phasing prediction. Chapter 2 describes the experimental setup and data analysis techniques applied to acquire test data. The critical physics based

models that generate input for combustion phasing prediction are presented in Chapter 3. Chapter 4 describes the detailed combustion phasing prediction structure which includes flame kernel development duration prediction and combustion phasing calculation after start of combustion. Chapter 5 explains the SI engine combustion constraints (knock and combustion variation) and model development. To realize combustion phasing control, a spark selection method is required, as proposed in Chapter 6. Chapter 7 describes the implementation of these real-time physical models in the rapid-prototype environment and provides validation data. A cylinder pressure based feedback/adaptation method for combustion model inputs is described in Chapter 8. Finally, Chapter 9 provides thesis summaries, conclusions and proposed future work.

CHAPTER TWO

ENGINE SETUP AND DATA ACQUISITION SYSTEM

This work is carried out at the Clemson University - International Center for Automotive Research (CU-ICAR). The facility contains a FEV-Test Systems environmentally controlled 430 kW (576 hp) containerized engine dynamometer that was used for the experimental portions of this research. The test cell contains a sophisticated experiment management system for precise data acquisition and control of test objects (See Figure 13 and Figure 14).

Figure 13: FEV test cell control room and data acquisition systems.

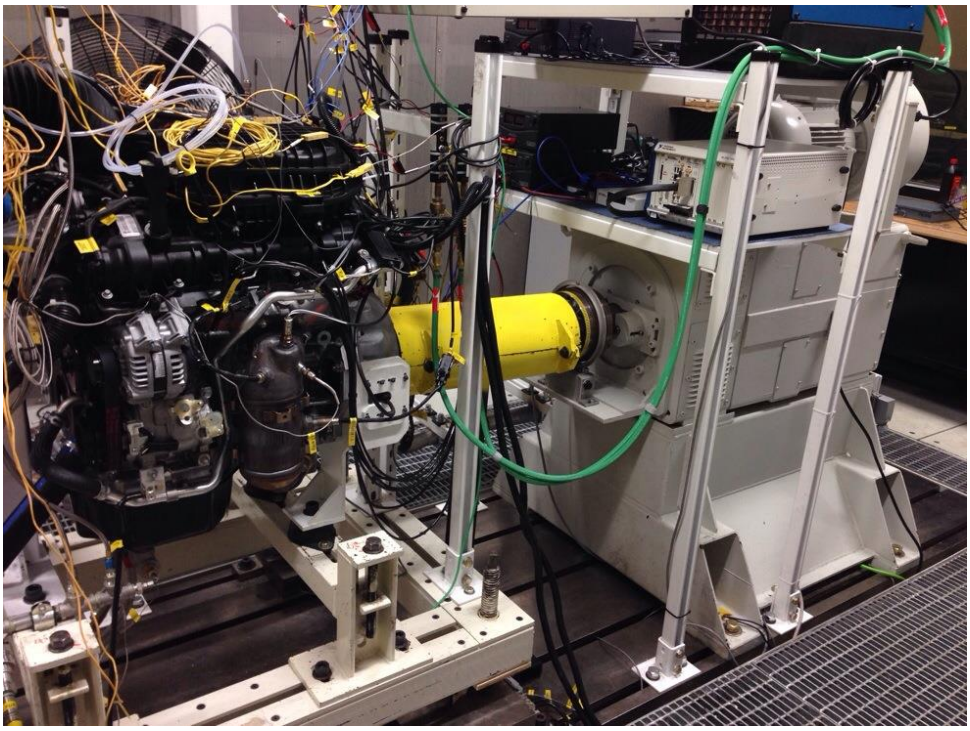

Figure 14: The FEV 430 kW transient AC dynamometer test cell with 3.6L V6 Pentastar engine.

2.1 Test Engine Description

The test engine is a naturally-aspirated 3.6 L port fuel injected V-6. The cylinder heads have two intake and two exhaust valves per cylinder and a pent-roof shaped combustion chamber (see Figure 15). The engine is equipped with oil-driven dual-independent valve phasing on both banks. A special flywheel (see Figure 16) was designed at Clemson University to connect the engine to the dynamometer driveshaft as to hold the crank angle encoder disk (AVL 365X). A summary of basic engine geometry is given in

Table 1.

Table 1: Engine Parameters

Fuel	Gasoline (87 Pump Octane)
Max Engine Speed	6400 RPM
Bore	96 mm
Stroke	83 mm
Compression Ratio	10.2
Connecting Rod Length	156.5 mm
Intake Valve Diameter	39 mm
Exhaust Valve Diameter	30 mm

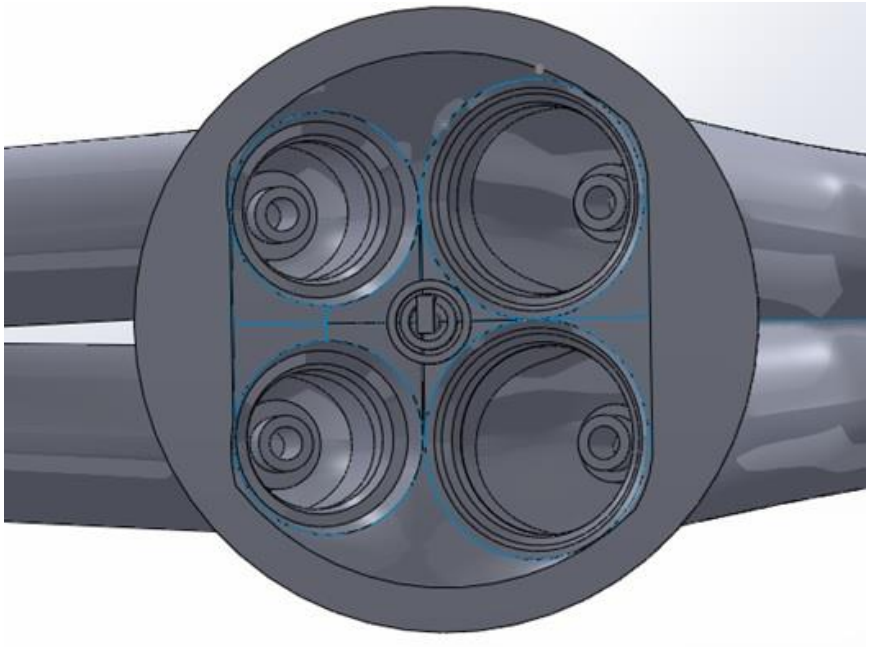

Figure 15: Approximate CAD Drawing of the Combustion Chamber

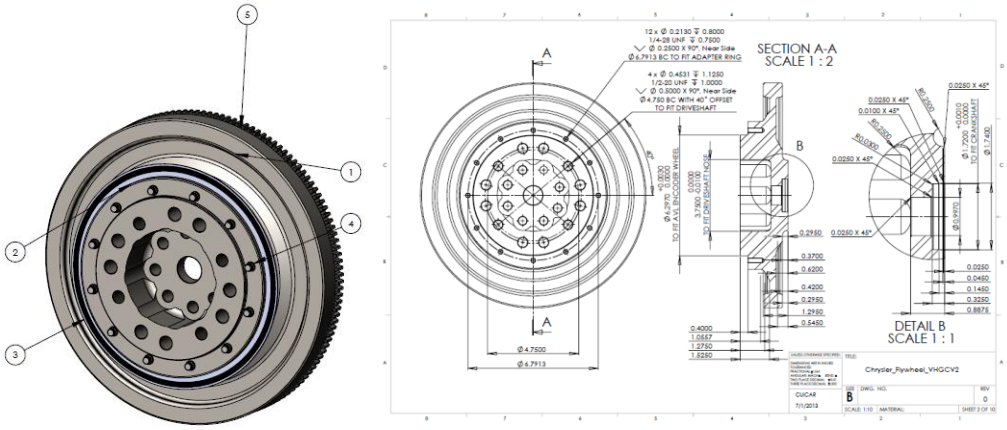

Figure 16: A custom flywheel was designed and built to connect the engine to the dynamometer driveshaft an hold the crank encoder disk.

2.2 Data Acquisition Setup

Combustion and gas exchange processes are the primary focus of experimental data collection to aid control model/algorithm development. Combustion analysis is performed using a 32 channel AVL 671 crank-angle resolved data acquisition system and AVL GH12D piezoelectric cylinder pressure sensors. The system is capable of sampling data in 0.025 crank angle degree intervals to properly capture all relevant combustion characteristics. Piezoresistive Kulite sensors are used for both intake and exhaust pressure measurements. The exhaust sensors are mounted in a specially designed fitting that is used to install them through water-jackets on the integrated exhaust manifold (see Figure 17). The exhaust sensors are cooled using a Miller TIG torch cooling system (Figure 18) to minimize signal drift when exposed to high temperatures. To support intake temperature modeling, four thermocouples have been installed in different locations in the engine intake system (Figure 19, the first two are visible). Another thermocouple has been installed to measure exhaust temperature (Figure 20). Besides one stock lambda

sensor, two more Bosch LSU 4.9 wide-band lambda sensors have been installed pre and post-catalyst (Figure 20).

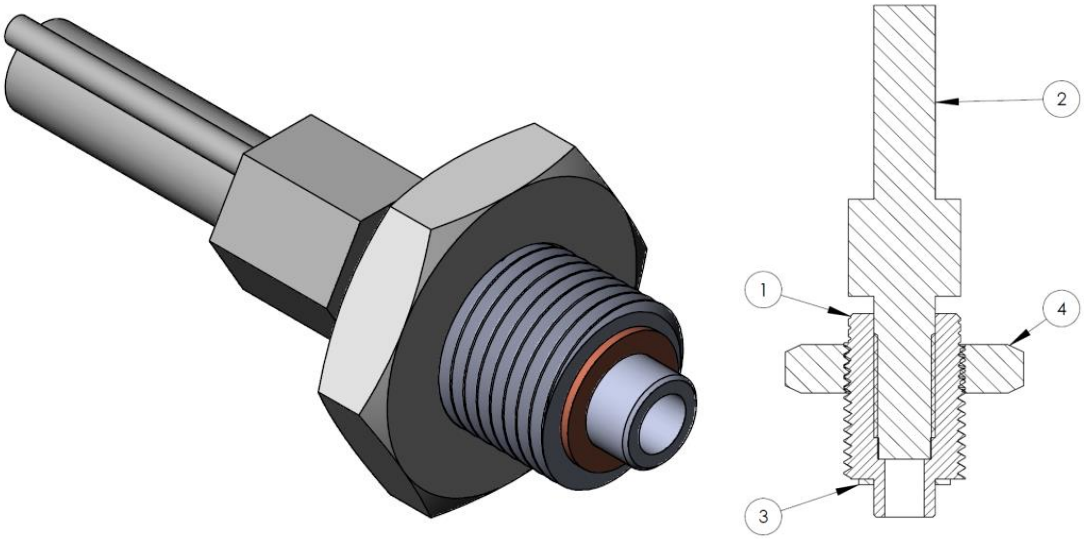

Figure 17: Custom fitting for the water-cooled exhaust sensors

Figure 18: Miller cool system for exhaust pressure sensor cooling

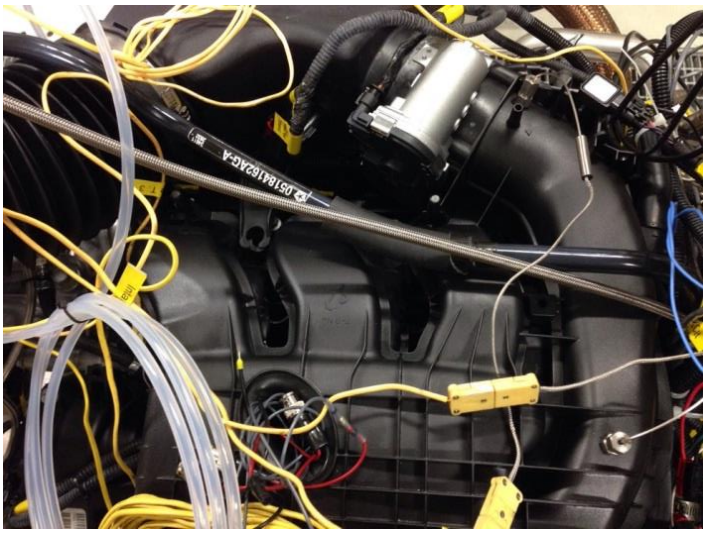

Figure 19: Intake are thermocouples (first two shown here, another two below intake manifold)

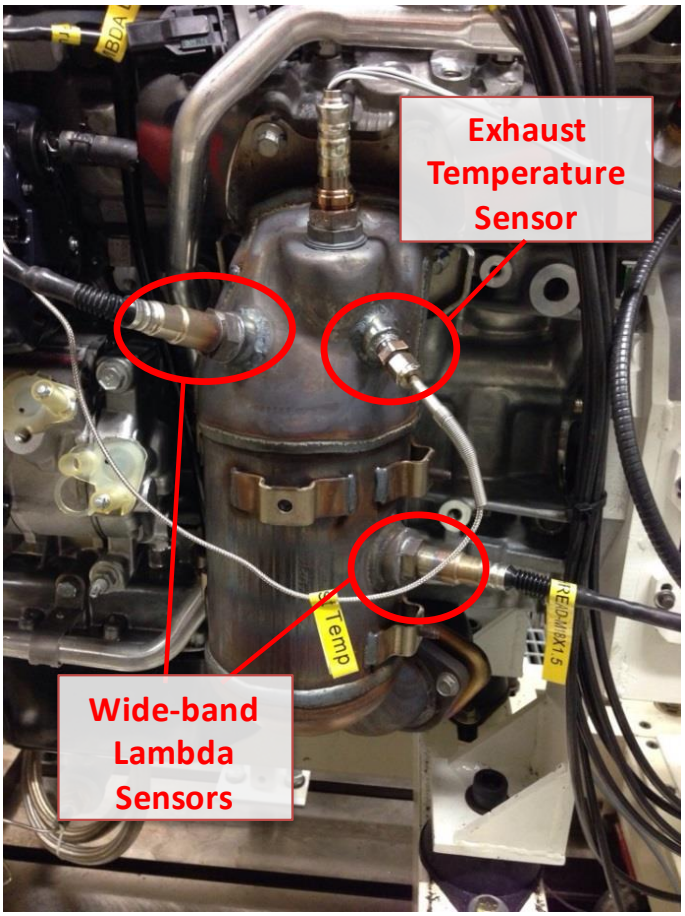

Figure 20: Exhaust temperature sensor and Bosch wide-band lambda sensors

AVL IndiCom software is used to monitor measured sensor signals from the data acquisition system cycle-by-cycle and record measured data. AVL Concerto software is used for combustion data analysis to provide in-cylinder temperatures, rate of heat release and other parameters. Crank angle resolved measurements of intake and exhaust port pressures are used with cylinder pressure for gas exchange analysis. A one-dimensional gas dynamic model of the combustion chamber, intake, and exhaust ports was built using AVL BOOST. This model was then imported into AVL Gas Exchange and Combustion Analysis (GCA) software for mass flow calculations across the intake and exhaust valves. The GCA software uses the experimentally measured intake and exhaust pressures as boundary conditions and calculates many difficult to measure gas exchange characteristics, such as internal residual gas fraction, and total in-cylinder mass.

2.3 Engine Control

An ETAS INTECRIO system is used to override the stock engine control system as-needed. The system allows for adjustment of engine actuators and is programmed using MATLAB/Simulink. Algorithm validation occurred experimentally on the dynamometer under steady-state and transient operating conditions. Steady-state operation (constant engine speed and load) is used for checking stability and accuracy of control models over a wide range of operating conditions. Transient tests (e.g. tip-in, tip-out, RPM sweep, etc) are utilized to verify if feed-forward control algorithms are functioning properly.

CHAPTER THREE

PHYSICS BASED INPUT MODELS FOR COMBUSTION PHASING PREDICTION

3.1 Combustion Rate Calculation Model Description

A quasi-dimensional turbulent entrainment combustion model is used for this research, which was originally proposed by Blizard and Keck [33] and then refined by Tabaczynski et al. [34-35]. This turbulent flame entrainment based combustion model assumes that the fresh mixture at the flame front is (1) entrained into small eddies and then (2) burned up in a characteristic time. Based on these assumptions, the flame entrainment and burned up processes are shown below as Equation 1 and 2 respectively.

$$\frac{dm_e}{dt} = \rho_{unburned} A_{flame} (u' + S_L) \tag{1}$$

$$\frac{dm_b}{dt} = \frac{m_e - m_b}{\tau} + \rho_{unburned} A_{flame} S_L \tag{2}$$

Equation 1 describes the unburned mass entrainment rate at the flame front. It is assumed the flame propagates through unburned charge along Kolmogorov scale vortices entraining turbulent eddies. The unburned mass entrainment rate is determined by unburned mixture density, flame front area, laminar flame speed and turbulence intensity. After unburned mixture entrainment, mass burn-up occurs at a rate described by Equation 2. Burn-up occurs at a characteristic time, τ, which is defined as the time to burn up an eddy at laminar flame speed. The eddy size is assumed to be Taylor microscale (λ) [34] and can be calculated by Equation 3.

$$\frac{\lambda}{L} = \sqrt{\frac{15}{\xi}} \left(\frac{u'L}{v}\right)^{-\frac{1}{2}} \tag{3}$$

The integral length scale, L, is utilized during the burn-up process. Prior to start of combustion, L is assumed to be the instantaneous chamber height [36]. After start of combustion the unburned mixture is compressed at a rate based on the rapid distortion theory [37]. The rapid distortion theory is applied when the timescale of turbulence distortion is much shorter than large eddy turnover or decay timescales [38]. The characteristic length scale calculation is shown as Equation 4. L_o and ρ_{uo} are defined as the instantaneous chamber height and unburned gas density at start of combustion.

$$L = L_o \left(\frac{\rho_{uo}}{\rho_{unburned}}\right)^{\frac{1}{3}} \tag{4}$$

3.2 Physics Based Input Models

As shown in Figure 21 the important physical inputs, laminar flame speed, turbulence intensity and residual gas mass, have significant effects on combustion related physical factors like flame kernel development, flame propagation, flame area surface and combustion stability.

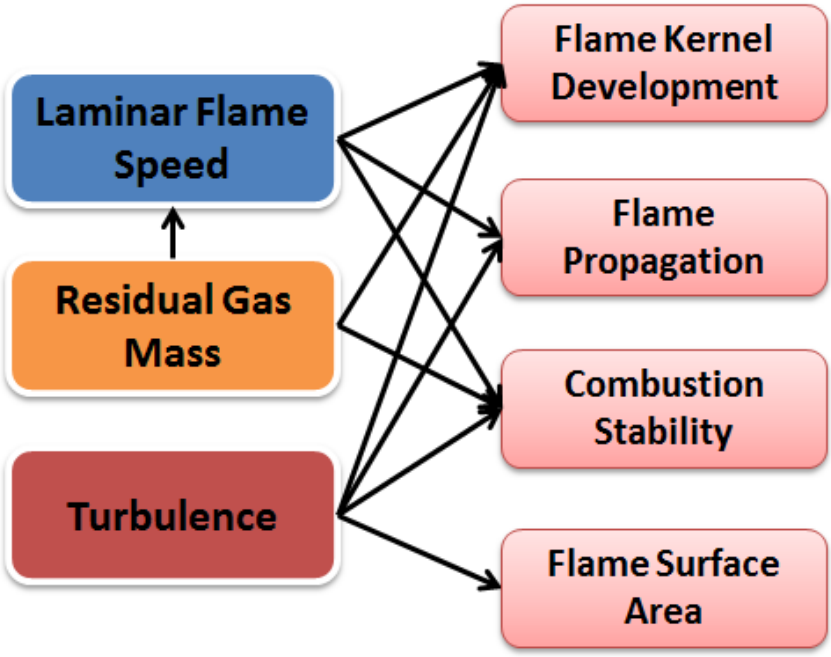

Figure 21: Input model effects on combustion

For laminar flame speed, it affects flame kernel development after ignition and the following flame propagation by influencing unburned mixture entrainment process and entrained eddy burning velocity. Its effect on combustion stability is described in [61] and could be combined with turbulence intensity to decide engine combustion stable operation zone. As for residual gas mass, it is the burned gas from last engine cycle and has effects on laminar flame speed, flame kernel development and combustion variability. Too much residual gas could significantly reduce combustion rate and increase the variability of combustion. The turbulence intensity also has a lot of influence on the flame kernel development, flame propagation, combustion stability and flame surface area. At the beginning of the combustion, in cylinder turbulence could help increase the kernel development rate. However, too much turbulence could destroy the

kernel [1]. Higher turbulence levels could help increase both unburned mixture entrainment and eddy burning velocity. Also, the turbulence will wrinkle the flame front surface and change the surface area [43]. The following sections will detail describe the physical based modeling these inputs models and show the model prediction results.

3.2.1 Residual Gas Mass Prediction Model

Residual gas mass/fraction prediction is essential for engine control in high degree of freedom engine to hit better fuel economy and drivability. Existing RGF calculation models have different methods from semi-empirical correlations (for example Fox [62], Shayler [63-64], Amer and Zhong [65] and Kale [66]) to three-dimensional CFD-based simulation calculations (Senecal [67]). Semi-empirical residual gas prediction models are popular for engine control purpose due to their simplified model form and reduced computational efforts. They allow fast residual gas fraction/mass estimation and even realize real-time calculation in ECU. The reference residual gas fraction/mass values for developing semi-physical models can be acquired from the experimental data from test engine by using in-cylinder CO_2 measurement method or calculated from virtual engine models (GT-Power) simulation.

The widely used semi-empirical residual gas fraction prediction model proposed by Fox et al. [62] separates residual gas into two terms: burned gas from backflow into cylinder during valve overlap and trapped residual gas inside cylinder due to clearance volume. These two parts combined together is the total predicted residual gas. Fox RGF model uses cross valve air flow rate model and ideal cycle analysis, and requires inputs as intake manifold pressure, exhaust manifold pressure, air/fuel ratio, compression ratio,

engine speed and overlap factor (OF) which is a function of valve profile and piston motion. The experimental RGF data is used to calibrate the constants in model. This semi-empirical model could realize real-time RGF prediction, but the accuracy and robustness of the model cannot be guaranteed when it is applied to wide engine operation range. The model is overly-sensitive to OF for small valve overlap. Moreover, the model fails to capture the gas dynamic effect on intake and exhaust manifold pressure and to consider the valve overlap center line effect on residual gas backflow. Shayler [63] developed a residual gas fraction model in 2000 based on intake and exhaust manifold pressure ratio, compression ratio, AFR, cylinder intake volumetric efficiency and EGR percentage. Different from Fox model, Shayler's model does not contain empirical fit constants. In 2004, Shayler improved the model to better predict RGF under high valve overlap conditions [64]. The results show a slight improvement is gained, however the residual gas backflow is under-estimated for low engine speeds, yielding low RGF calculation. In 2006, Amer and Zhong refined Shayler's model by replacing an constant in Shayler's model with a variable, called the "density modifier term" (DMT), to better capture engine speed, overlap volume, volumetric efficiency and exhaust cam location effects [65]. DMT equation contains 25 constants and is generated from a non-linear regression fit by using experiment or simulation RGF data. The model predictions seem to be more accurate, but the fitting process is very complicated and this reduces the adaptive ability of the model and weakens the robustness of the model. In 2013, Kale et al. improved the Fox RGF model by means of isolation and characterization of the gas exchange physical processes [66]. For this improved model, the overlap factor considers

the phasing of intake and exhaust valves with respect to the piston motion. The OF has been separated into speed dependent OF_s and non-speed dependent OF_{ns}. Then, there two overlap factors are fitted based on results from GT-Power simulation.

Consistent with literature, the residual gas in this research is defined as the in-cylinder combustion products from last engine cycle. The total residual gas mass consists of two parts: (i) burned gas from backflow into cylinder during valve overlap period and (ii) trapped residual prior to valve overlap due to cylinder clearance volume . The equation to define residual gas mass is shown as Equation (5.

$$m_r = \int_{IVO}^{EVC} \dot{m}_{backflow} dt + m_{trapped} \tag{5}$$

For the residual gas mass from backflow (first part in Equation (5, the intake manifold pressure, exhaust manifold pressure, intake and exhaust valve timings, valve profiles and engine speed are important physical factors affecting its value. As for the trapped residual mass (second term in Equation (5, the engine geometry, for example engine displacement and compression ratio, and burned gas density are critical.

During valve overlap period, both intake and exhaust valves are open. Intake manifold, exhaust manifold and cylinder become a system where the gas mixture can freely flow across valves due to pressure differences. For this research, the gas flow is assumed to be incompressible. According to Bernoulli's principle, the mass flow rate through an orifice for the incompressible flow can be represented as Equation (6 shown below.

$$\dot{m} = C \cdot A \cdot \sqrt{2\rho(P_1 - P_2)} \tag{6}$$

In Equation (6, C is the valve flow coefficient, A is the effective area that can be calculated from valve lift and timing and ρ is the mixture density. P_1, P_2 are pressures on each side of the valve and P_1 is the higher pressure. The larger the pressure difference between P_1 and P_2, the higher the mass flow rate across the valve. Therefore, pressure difference between the intake and exhaust manifold pressure is a main factor to drive the residual gas backflow.

3.2.1.1 Valve Profile and Timing Effect

The effective area, as an input for Equation (6, is critical for residual gas mass prediction. It is separated into intake valve and exhaust valve terms. For intake part, the area is defined as integration of the band area between the intake valve head and the valve seat on engine block from intake valve opening (IVO, as SAE standard valve lift larger than 0.15mm) to overlap centerline (OLC) where intake and exhaust valves have the same lift (shown in Figure 22). Similarly, the exhaust part is the flow area integration from OLC to exhaust valve closing (EVC, as SAE standard valve lift smaller than 0.15mm). These two parts together represent the total effective flow area A. The calculation model is shown as Equation (7).

$$A = \int_{IVO}^{IV=EV} D_i \cdot L_i d\theta + \int_{IV=EV}^{EVC} D_e \cdot L_e d\theta \tag{7}$$

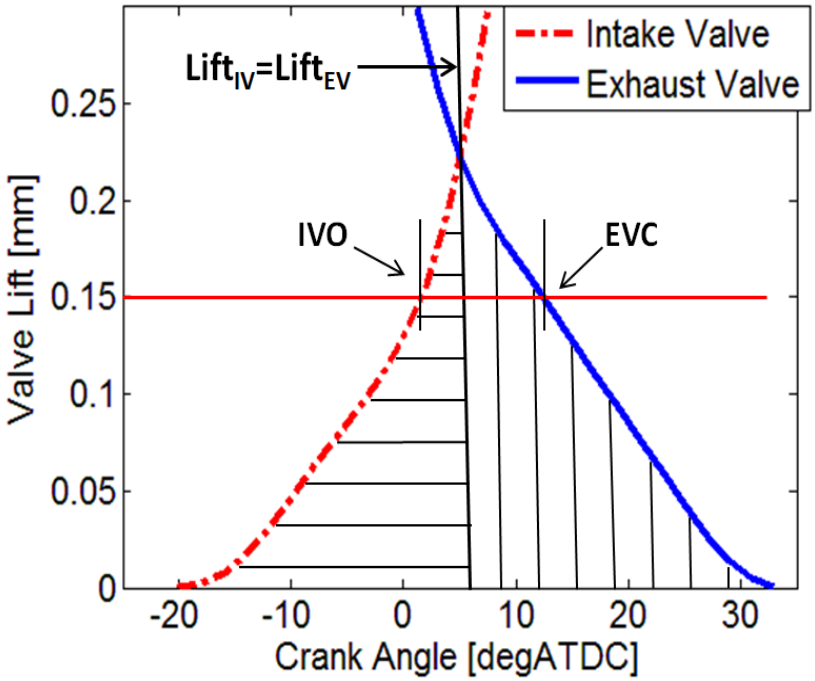

Figure 22. Intake and exhaust valve profiles during overlap. Valve overlap centerline (OLC) is defined as the crank angle location where intake and exhaust lifts are equal.

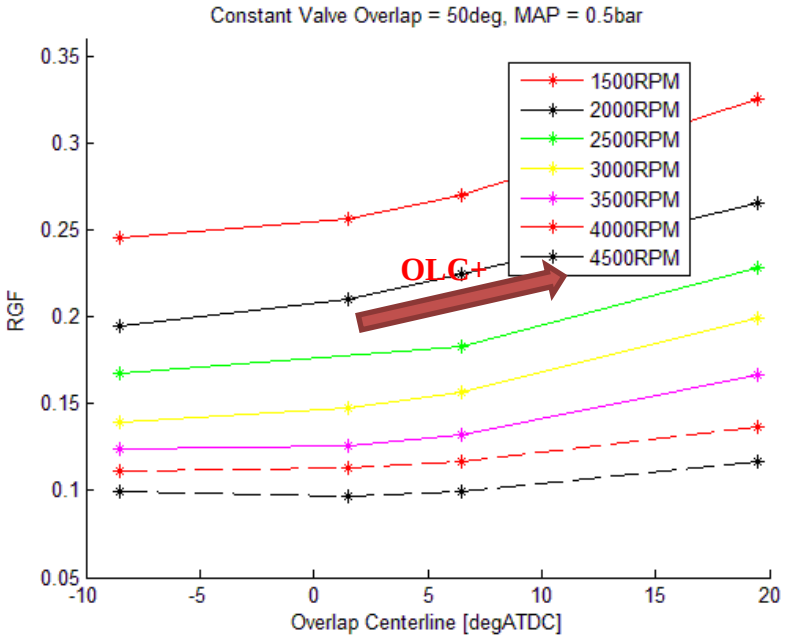

Figure 23: Valve overlap centerline effect on residual gas fraction for different engine speeds

Besides overlap effective flow area, location of the valve overlap centerline is another important factor for residual gas backflow rate. With a same effective area value, the different OLCs have difference residual gas mass values (shown in Figure 23) because moving of the overlap centerline corresponds to different piston motion.

To capture the OLC effect, the physical overlap volume (OLV) is introduced (Equation (8)). It is the cylinder volume difference between intake valve opening and exhaust valve closing (overlap period).

$$OLV = V_{EVC} - V_{IVO} \tag{8}$$

3.2.1.2 Engine Speed and Geometry Effect

According to Equation (5), the time for overlap period is needed to calculate backflow residual gas mass. With the same overlap crank angle duration, higher engine speed has shorter time for burned gas backflow, so the residual gas mass/fraction value will be smaller (shown in Figure 24). The RGF dropping at 1500rpm is due to gas dynamic effect which will be described in detail in the following part.

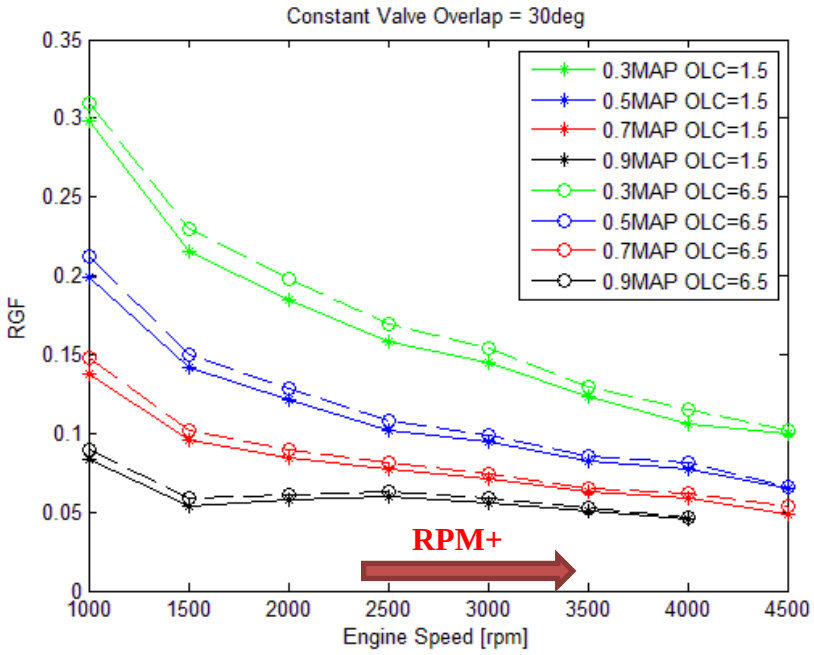

Figure 24: Engine speed effect on residual gas fraction for different engine MAP and OLC

The second term in Equation (5) is the trapped residual gas mass in cylinder which is decided by engine clearance volume and burned gas density. The engine clearance volume can be calculated by engine compression ratio and displacement (Equation (9)). Here V_d is engine displacement, r_c is compression ratio and V_c is cylinder clearance volume. Once the cylinder clearance volume is calculated, the trapped residual gas mass can be calculated based on gas density (estimated based on cylinder exhaust pressure and ideal gas law) and volume.

$$V_c = \frac{V_d}{r_c - 1} \tag{9}$$

3.2.1.3 Gas Dynamic Effect

As mentioned in the previous part, intake and exhaust manifold pressures are critical for the residual gas backflow rate calculation (Equation (6). Based on fluid mechanics, when intake and exhaust gases pass through the intake and exhaust system, they create dynamic pressure waves. The phenomenon can be seen in Figure 25. The pressures are measured with half degree crank angle resolution transducers. The average intake and exhaust manifold pressures are 0.98 bar and 1.1 bar respectively, but for every different crank angle, the pressure values are different. During valve overlap period, shown in Figure 25 shadow window, intake and exhaust pressure values can be very different from the average value. The gas dynamic effects on pressures during overlap can be observed clearly in Figure 26 and Figure 27, especially for intake pressure. However, in real world, for engine control, commonly only average intake manifold pressure (MAP) is available from the engine sensor. Hence, gas dynamics need to be modeled.

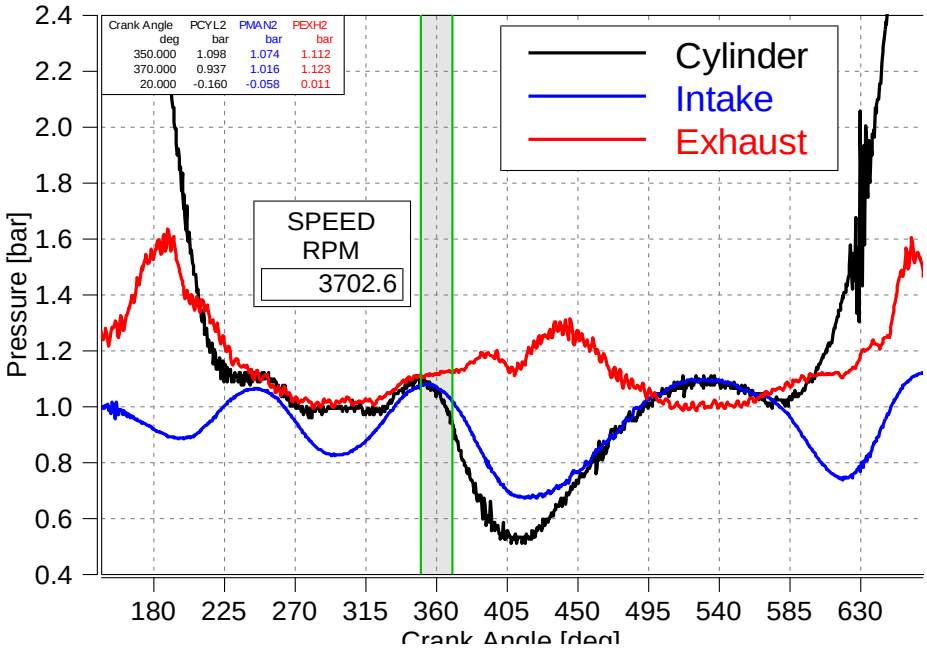

Figure 25: Intake, exhaust and cylinder pressure waves during a whole engine cycle

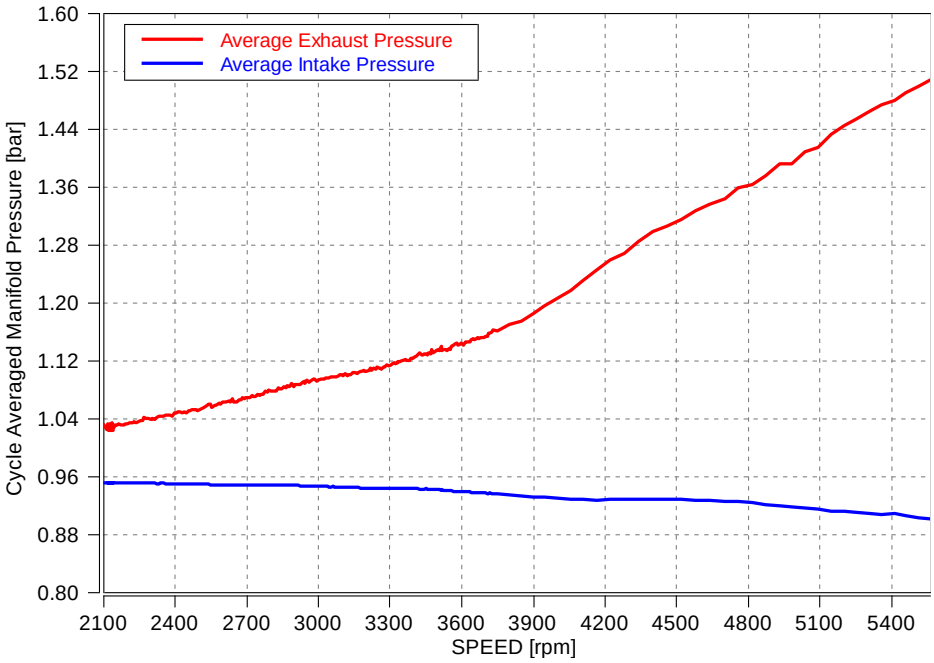

Figure 26: Average Intake, exhaust manifold pressures for different engine speeds

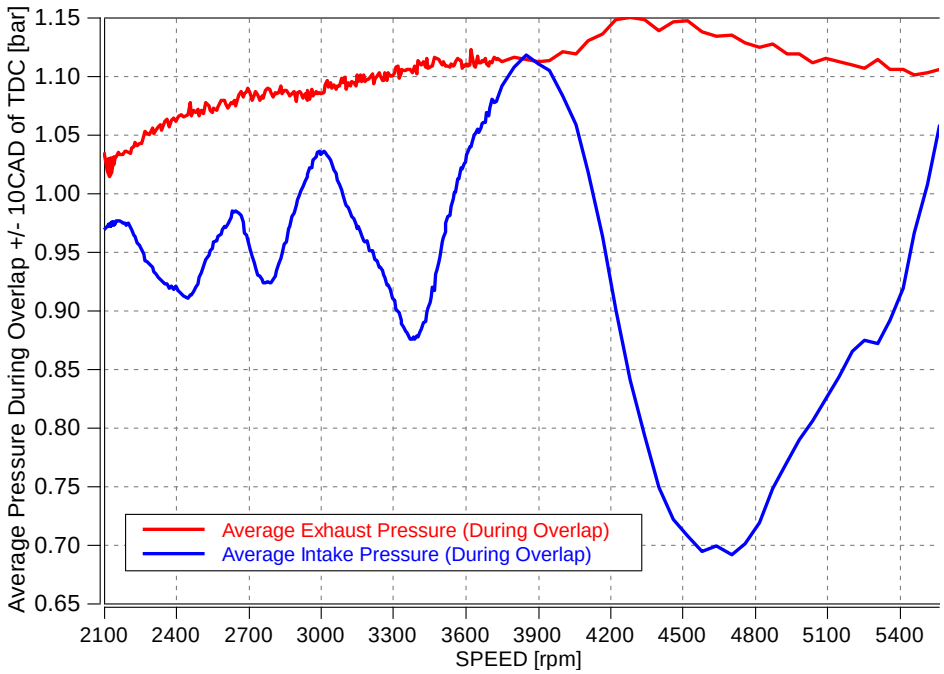

Figure 27: Average Intake, exhaust manifold pressures during valve overlap for different engine speeds

Firstly, to capture the gas dynamic effects on intake and exhaust pressure values during overlap, the pressure difference between intake/exhaust average pressures during whole cycle and during overlap is needed. Figure 28 shows this pressure differences for intake and exhaust for different engine speed under wide open throttle (WOT) operation condition. This engine speed effect on pressure differences can be stored as the reference pressure $P_{iOL}(RPM)$ and $P_{eOL}(RPM)$.

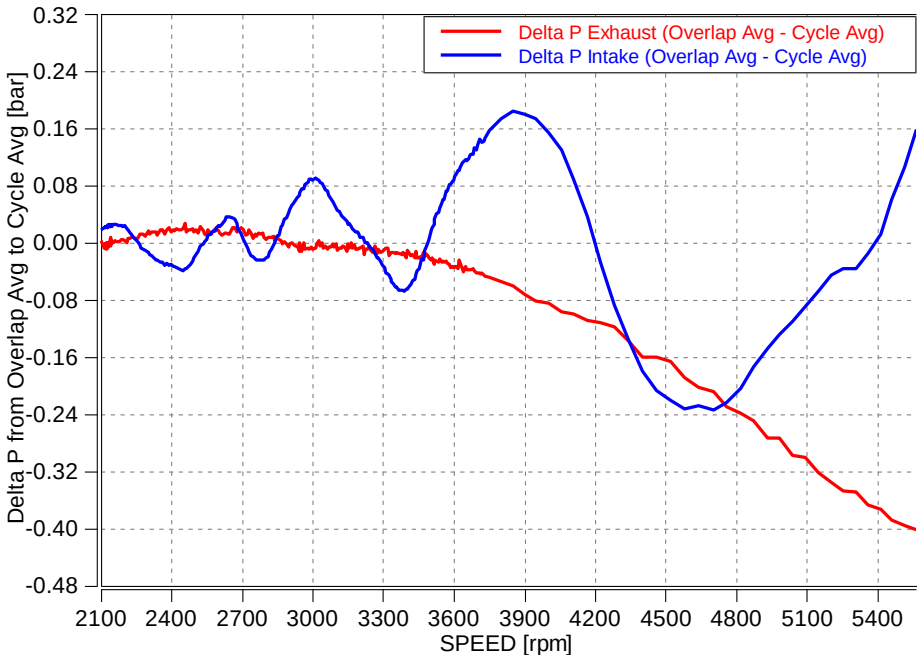

Figure 28: Pressure difference between average intake, exhaust manifold pressures and intake, exhaust pressures during valve overlap for different engine speeds

Besides engine speed effect on gas dynamics, engine load (MAP) can be another physic affecting gas dynamic waves. Figure 29 shows the normalized crank angle resolution intake manifold pressure waves for different engine MAPs at 4000RPM. The waves clearly show that higher engine load increases gas dynamic wave magnitude and this trend can be modeled by a MAP related multiplier M_{MAP}. The MAP effect on exhaust gas dynamic during overlap is relatively small (<1Kpa).

Moreover, the valve timings also affect the intake/exhaust manifold pressure during overlap. Figure 30 and Figure 31 show the ICL (intake valve centerline location) and ECL (exhaust valve centerline location) effects on intake and exhaust overlap period pressures. ICL and ECL are defined as the intake and exhaust valve maximum lift crank angle location.

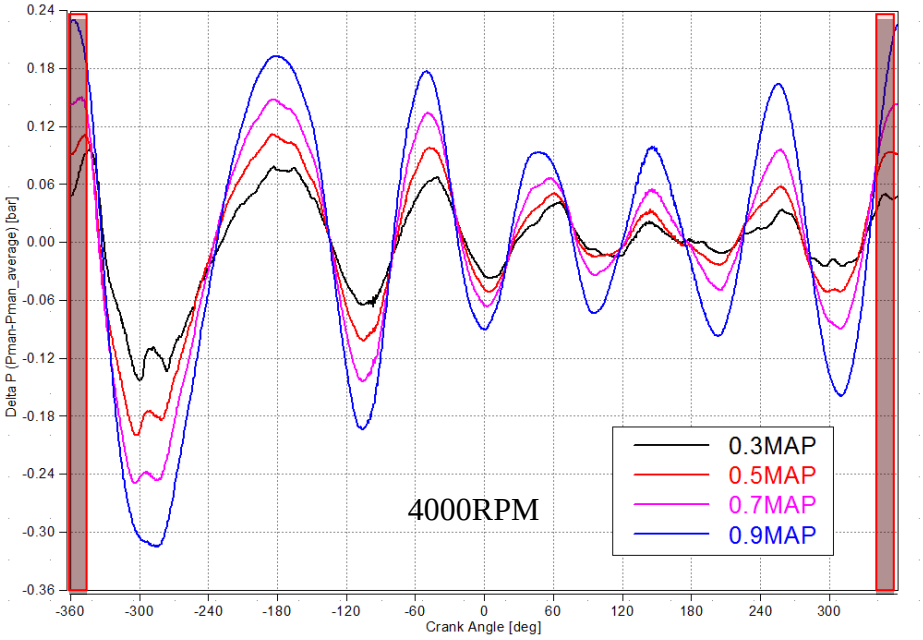

Figure 29: Normalized intake manifold pressure waves for different engine load at 4000RPM

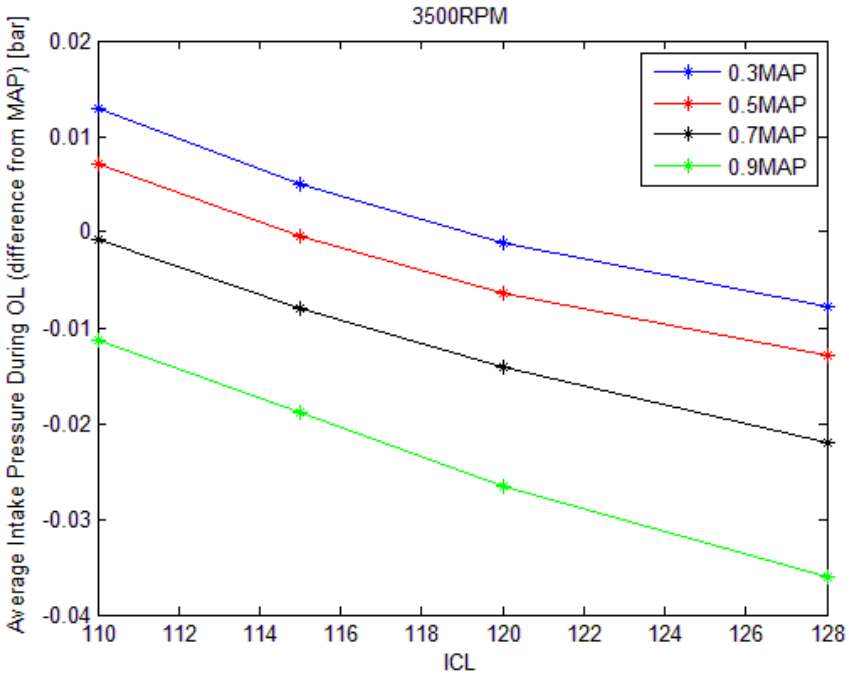

Figure 30: Intake valve timing effect on intake pressure difference during overlap

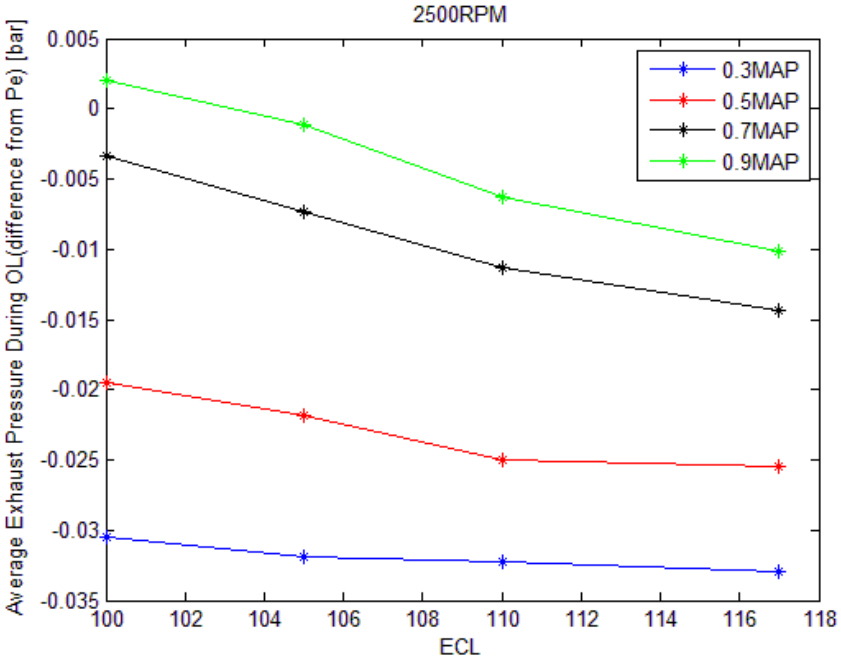

Figure 31: Exhaust valve timing effect on exhaust pressure difference during overlap

The valve timing effects can be assumed as linear with different slope for different engine loads. This valve timing effects can be modeled as P_{iOL}(ICL) and P_{eOL}(ECL).

Combining the engine speed, engine load and valve timing effects together, the intake/exhaust gas dynamic model shown as Equation (10) and Equation (11).

$$Pi_{OL} = M_{MAP} \cdot Pi_{OL}(RPM) + Pi_{OL}(ICL) \quad (10)$$

$$Pe_{OL} = Pe_{OL}(RPM) + Pe_{OL}(ECL) \quad (11)$$

3.2.1.4 Residual Gas Mass Model

Based on the previous discussion, the residual gas mass from backflow during valve overlap period is determined from pressure difference between intake and exhaust

manifold, valve timing and profile, engine speed and burned gas density. Then the backflow residual gas mass can be modeled as Equation (12).

$$m_{backflow} = C1 \cdot \sqrt{\rho \cdot (P_e - P_i)} \cdot A_{flow} \cdot \frac{OLV}{\mathrm{N}} \tag{12}$$

As to the trapped residual gas mass $m_{trapped}$, it is calculated from engine clearance volume and burned gas density (Equation (13)).

$$m_{trapped} = C2 \cdot \rho \cdot V_c \tag{13}$$

From Ideal Gas Law which is shown as Equation (14), the burned gas density can be calculated from exhaust pressure and temperature (Equation (15)). Then combine backflow residual gas and trapped residual gas together, the residual gas mass prediction is modeled as Equation (16).

$$PV = mRT \tag{14}$$

$$\rho_{burned} = \frac{P_e}{RT_e} \tag{15}$$

$$RGM = C1 \cdot \sqrt{(P_e/RT_e) \cdot (P_e - P_i)} \cdot A_{flow} \cdot \frac{OLV}{\mathrm{N}} + C2 \cdot \left(\frac{P_e}{RT_e}\right) \cdot V_c \tag{16}$$

Add intake and exhaust gas dynamic effects (Pi_{OL} and Pe_{OL}) in the model, the RGM model is shown as Equation (17).

$$RGM = C1 \cdot \sqrt{(P_e/RT_e) \cdot ((P_e + Pe_{OL}) - (P_i + Pi_{OL}))} \cdot A_{flow} \cdot \frac{OLV}{\mathrm{N}} + C2 \cdot \left(\frac{P_e}{RT_e}\right) \cdot V_c \tag{17}$$

The constants C_1 and C_2 need to be fitted to finish the RGM model. In Equation (17), C_1 and C_2 are the only two unknown parameters and they can be obtained by using linear fit with experimental data. To calculate the constants C_1 and C_2, the linear polynomial fit is applied and Figure 32 shows the results.

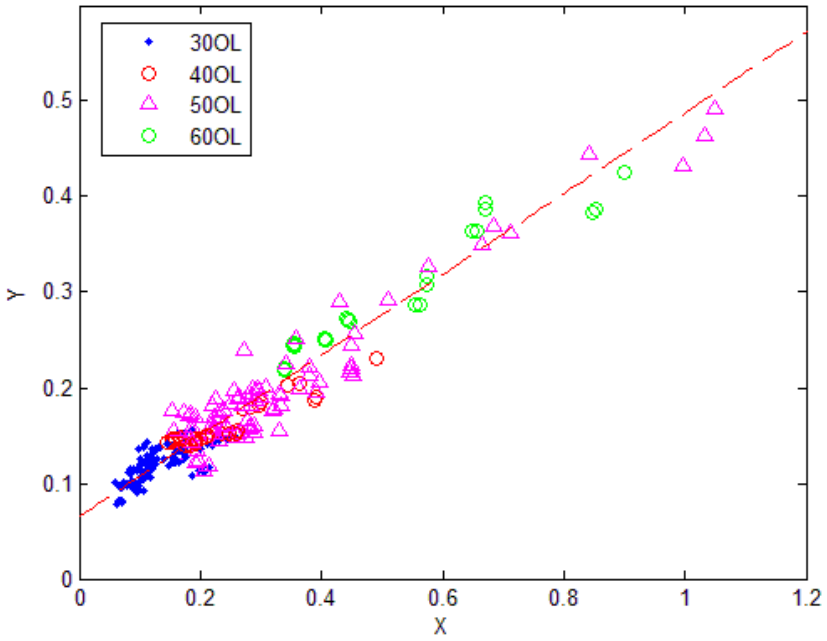

Figure 32: Linear polynomial fitting result for constants C1 and C2 in RGM model

X in x-axis is $\sqrt{(P_e/RT_e)\cdot((P_e+Pe_{OL})-(P_i+Pi_{OL}))}\cdot A_{flow}\cdot OLV/(N\cdot(P_e\cdot\frac{V_c}{RT_e}))$ **and Y in y-axis represents** $RGM/(P_e\cdot V_c/RT_e)$**. The experimental data set shown in Figure 32 covers engine speed from 1000RPM to 4500RPM, MAP from 0.3bar to 0.9bar, valve overlap from 30deg to 60deg. The linear polynomial fitting result is shown in**

Table 2.

Table 2: Linear Polynomial Fitting for RGM Model

Constant C1	0.4225
Constant C2	0.0651
R square	0.8927
Root-Mean-Square-Error	0.03245

The following Figure 33 shows the residual gas mass SIMULINK model which will be implemented into ETAS rapid prototype ECU ES910. The ETAS system can transfer the SIMULINK model to codes that can run in ECU by INTECRIO. Then the RGM results can be read and record by using ETAS INCA.

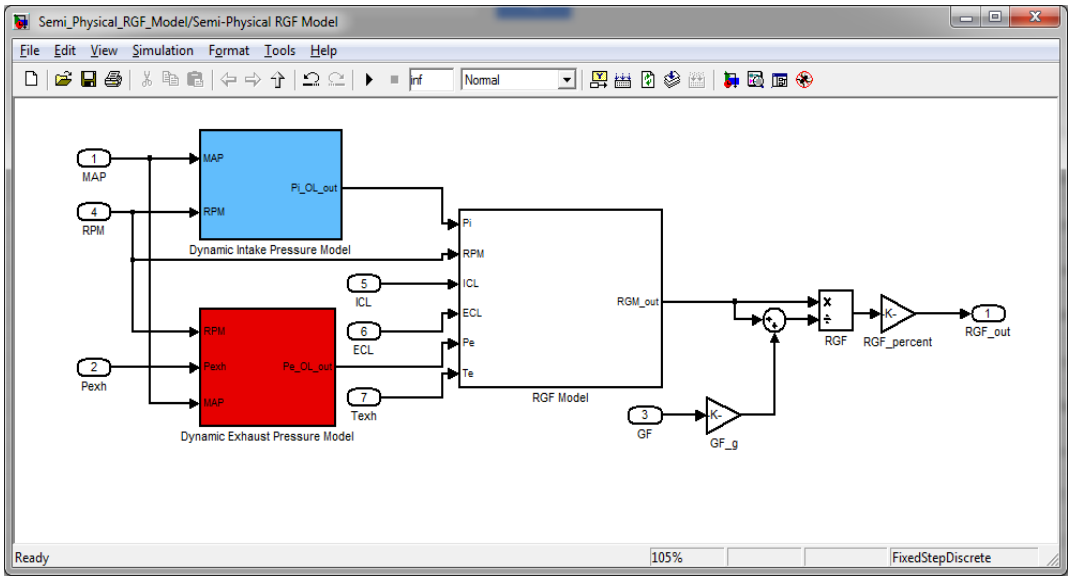

Figure 33: Residual Gas Mass Prediction Model (SIMULINK Model)

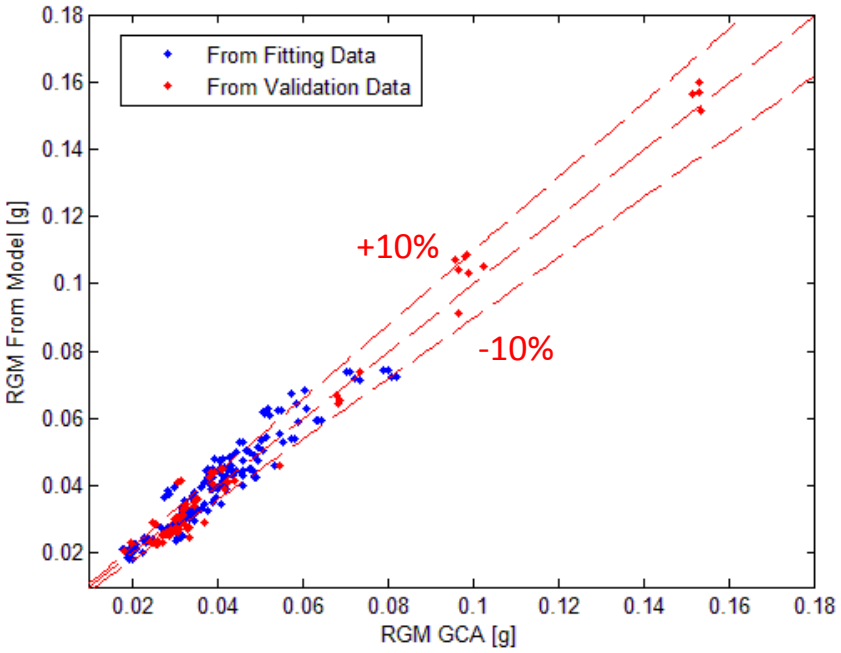

Figure 34: Off-line RGM model validation

Figure 34 shown above is the off-line residual gas mass prediction model validation results. Part of the validate data are from fitting data set and others are only used to validate the RGM model. In this figure, the comparison between RGM from reference data and from model prediction is shown and the dash lines represents the +10% and -10% error zone. 400 data points cover engine speed from 1000RPM to 4500RPM, MAP from 0.3bar to 0.9bar, valve overlap from 30deg to 60deg. The Root Mean Square Error (RMSE) is 0.0072g. The maximum error is 0.011g.

3.2.2 Laminar Flame Speed Prediction Model

The laminar flame speed is an important intrinsic property of combustible fuel, air, and burned gas mixture. It is defined as the velocity, relative to and normal to the flame front, with which unburned gas moves into the front and is transformed to the

products under laminar flow conditions [1]. Under the pressure and temperature in the common engine operation conditions, laminar flame speed is measured in spherical constant volume vessels by propagating a laminar flame radially outward from the vessel center. The laminar burning velocity is then given by Equation (18).

$$S_L = \frac{dm_b/dt}{A_f \rho_u} \tag{18}$$

Laminar flame speed model as a sub-model for the combustion phasing prediction model plays a critical role. For example, for the quasi-dimensional flame entrainment combustion model, laminar flame speed is an important input for both the flame entrainment and burn up predictions.

According to Heywood [1], laminar flame speed is defined as a function of unburned mixture thermodynamic properties and composition, only. The Equation (19) shows the physical based laminar flame speed model. In the laminar flame speed model, the reference laminar flame speed $S_{L,0}$ is defined by the Equation (20). It related to fuel property and air-to-fuel ratio. With considering the residual gas effects on the laminar flame speed, the complete form of the laminar flame speed model is shown as Equation (21).

$$S_L = S_{L,0}\left(\frac{T_u}{T_0}\right)^{\alpha}\left(\frac{p}{p_0}\right)^{\beta} \tag{19}$$

where $\alpha = 2.4 - 0.271\emptyset^{3.51}, \beta = -0.357 + 0.14\emptyset^{2.77}$

$$S_{L,0} = B_m + B_{\emptyset}(\emptyset - \emptyset_m)^2 \tag{20}$$

$$S_L(x_b) = S_L(x_b = 0)(1 - 2.06x_b^{0.77}) \quad (21)$$

The Table 3 below shows fuel property related parameters for different fuels.

Table 3:Fuel property parameters for different fuels

Fuel	$\emptyset_m$	B_m	$B_\emptyset$
Methanol	1.11	36.9	-140.5
Propane	1.08	34.2	-138.7
Isooctane	1.13	26.3	-84.7
Gasoline	1.21	30.5	-54.9

Besides fuel properties effects, it can be seen the laminar flame speed also depends on the gas pressure, temperature and residual gas fraction. Unfortunately, the production engines often do not have cylinder pressure and temperature sensors. Another input, the residual gas fraction, is difficult to measure even for the experiment engine lab, let alone for the normal production engines. Due to these limitations, the inputs sub-models are badly needed.

3.2.2.1 Semi-physical cylinder pressure model

In order to model the cylinder pressure, the first step is to figure out the important physics that will strongly affect the cylinder pressure. Figure 35 shows the important physics. The engine speed will affect pressure drop across intake valves and also the gas dynamic wave. Manifold pressure decides the initial pressure condition in the manifold and valve time together with gas dynamics affect the intake pressure at intake valve closing (IVC).

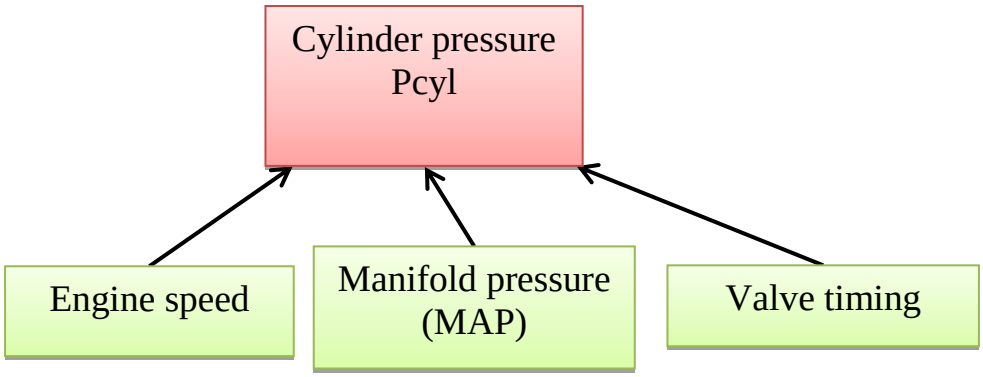

Figure 35: Important physical factors for cylinder pressure

After intake valves closing, the compression of the mixture can be seen as isotropic and cylinder pressure can be calculated based on the ideal gas law and this makes the initialization cylinder pressure at IVC critical for the subsequent cylinder pressure prediction. The following part will focus on the modeling of the cylinder pressure at IVC.

3.2.2.2 Cylinder pressure at IVC

Cylinder pressure at IVC will be strongly affected by engine speed, manifold pressure (MAP) and intake valve timing. In order to model the pressure at IVC, the analysis of the important physical factors' effect on the cylinder pressure at IVC will be presented first.

For instance, engine speed effects on P_{IVC} are shown in Figure 36. The y-axis is normalized cylinder pressure at IVC which is the pressure difference between the actual cylinder pressure at IVC and average manifold pressure (MAP). P_{IVC} will be higher for the retard of the intake valve closing and for different IVC, the engine effect on P_{IVC} is

similar. To capture the engine speed effect, the black curve with triangle markers is stored as the basic PIVC line (Figure 37).

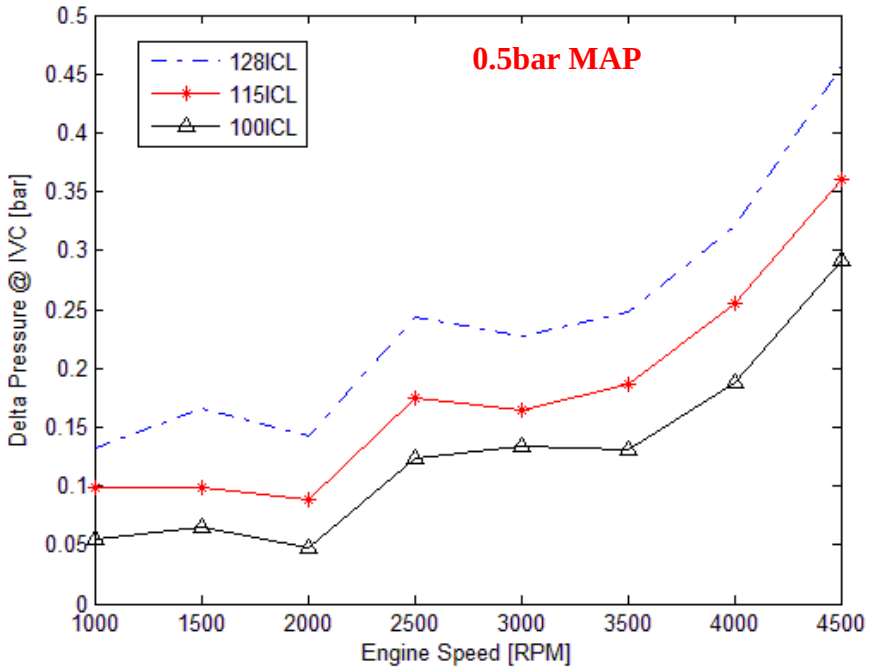

Figure 36: Engine speed effect on PIVC for different intake valve timing under 0.5 bar MAP operation in the test cell

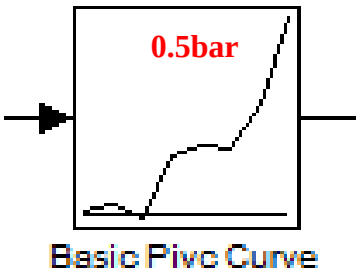

Figure 37: Basic PIVC line (look up table in SIMULINK)

After storing the basic PIVC line, the manifold pressure effect on PIVC should be considered. In Figure 38, it shows engine speed effect on PIVC under different manifold

pressures with the same intake valve timing. For different MAPs, the engine speed effect trends are similar, but here MAP will lead to higher normalized PIVC due to the heavier gas dynamic effects. Equation (22) is to capture these difference caused by different MAPs.

$$P_{IVC,MAP} = (0.085MAP^2 + 0.0345MAP + 0.0169) \quad (22)$$

To model the intake valve closing effect on PIVC. Figure 38 shows the intake valve closing timing effect on PIVC.

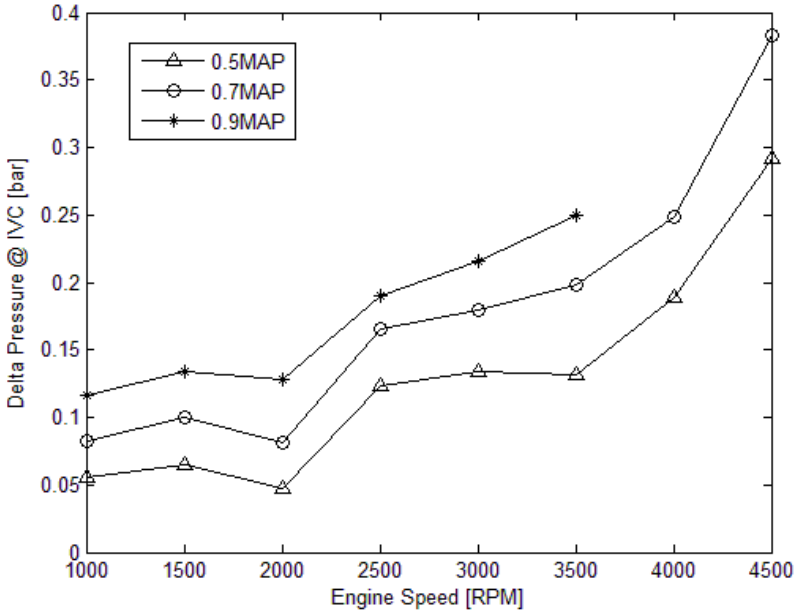

Figure 38: Engine speed effect on PIVC for different MAP with the same intake valve timing

ICL is short for Intake valve centerline, which is the crank angle location of the peak lift of the intake valve. It is used to represent the intake valve timing. From Figure 39 and Figure 40, it can be seen cylinder pressure at IVC has a relatively linear

relationship with intake valve timing. However the slopes of the linear lines are different for each engine speed and manifold pressure.

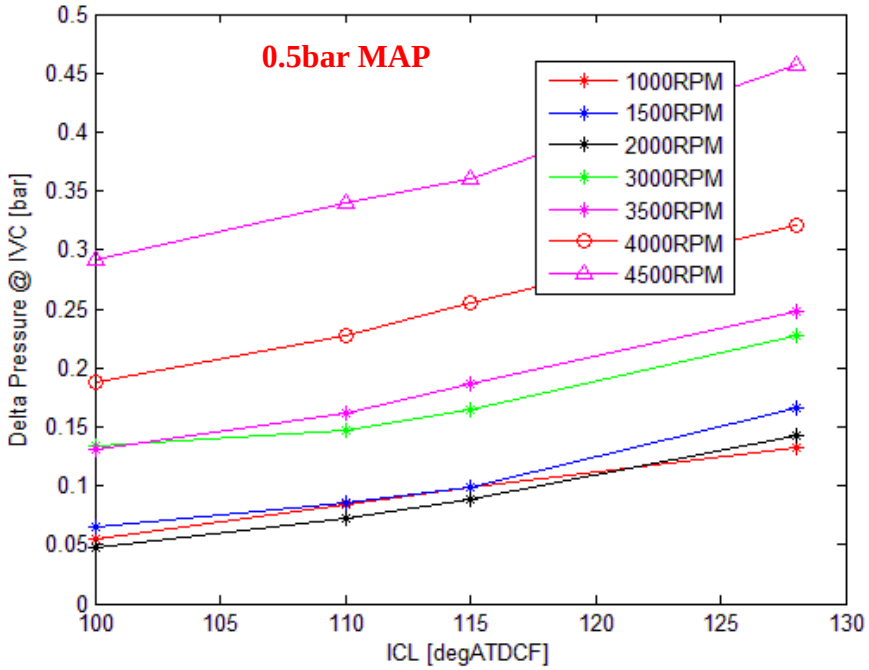

Figure 39: Intake valve timing effect on PIVC for different engine speeds under 0.5 bar MAP

$$Slope_{MAP} = 0.007991MAP^2 - 0.0033MAP + 0.002393 \quad (23)$$

$$Slope_{RPM} = RPM \cdot (0.003036MAP + 0.000494) \quad (24)$$

Equation (23) captures the MAP effect on the intake valve timing effect line slope and Equation (24) models engine speed effect on the intake valve timing effect slope.

After modeling all the important physical factors effects on P_{IVC}, the complete semi-physical P_{IVC} model is shown below (Equation (25)). The first part in the equation is intake valve timing effect. Next lookup table captures engine speed effect, and the last part is manifold pressure (MAP) effect.

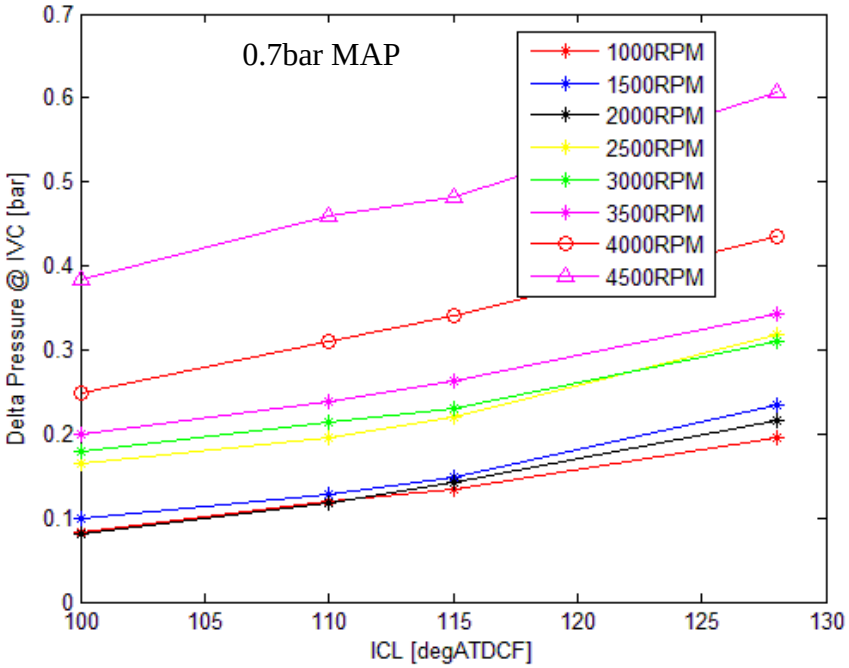

Figure 40: Intake valve timing effect on PIVC for different engine speeds under 0.7 bar MAP

$$P_{IVC} = (ICL - 100) \cdot (Slope_{MAP} + Slope_{RPM}) + \text{Basic PIVC Curve} + (0.085MAP^2 + 0.0345MAP + 0.0169) \quad (25)$$

3.2.2.3 Cylinder pressure during compression

Once the cylinder pressure at intake valve closing has been calculated, the cylinder pressure values at other instances during compression can be predicted based on the ideal gas law. The Equation (26) shows the cylinder pressure calculation algorithm.

$$P_{cyl} = P_{IVC}(\frac{V_{IVC}}{V_{cyl}})^{\gamma} \quad (26)$$

In the Equation (26), P_{IVC} is generated from the previous model, V_{cyl} can be calculated according to the crank angle location and the compression polytrophic coefficient γ is assumed to be 1.32.

3.2.2.4 Semi-physical cylinder pressure prediction model validation

The semi-physical cylinder pressure prediction model validated and the results are shown in Figure 41. The validation data set is under wide range of engine speed, manifold pressure and intake valve timing. The cylinder pressure values shown as blue dots in Figure 41 are cylinder pressures at 40 degree before TDC firing. The X-axis is the measured cylinder pressure and the y-axis is calculated cylinder pressure from the semi-physical prediction model. The solid red line is the ideal/no error line and two dash red lines represent +10% and -10% error limitations.

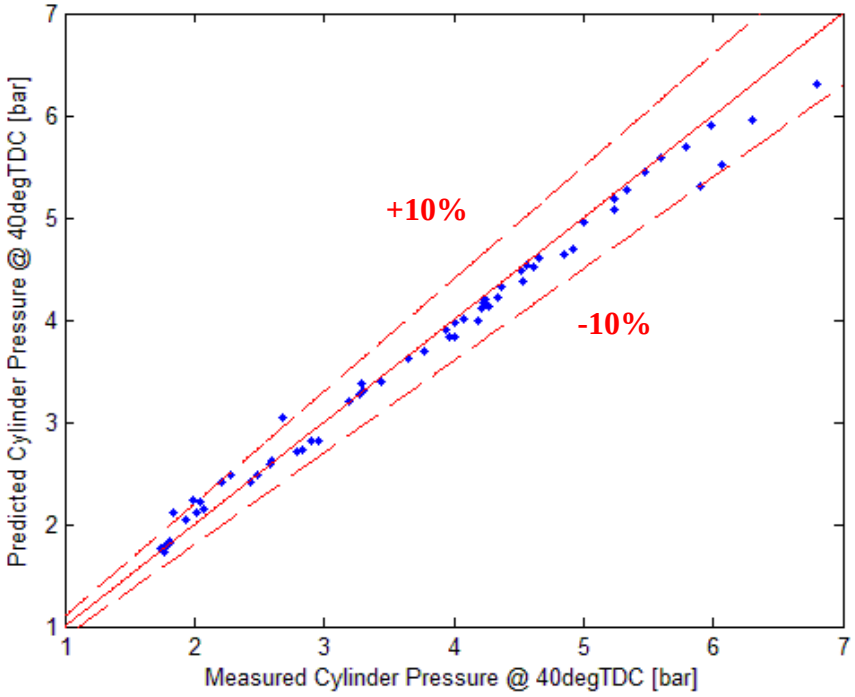

Figure 41: Semi-physical cylinder pressure prediction model validation

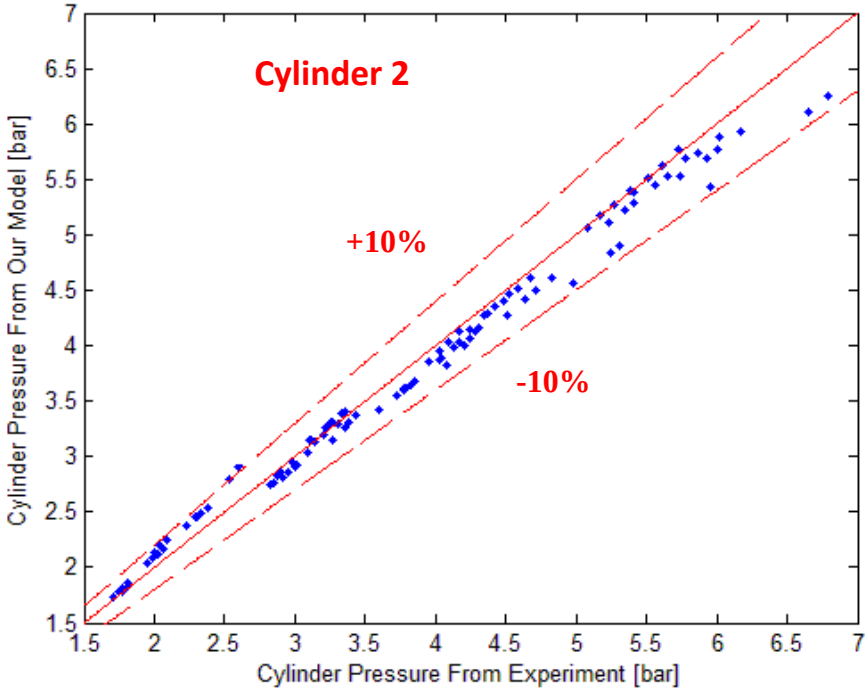

Figure 42: Semi-physical cylinder pressure prediction model validation for cylinder 2

To validate the adaptive ability of the cylinder pressure prediction model, the model has been applied to the other two cylinders (cylinder 2 and cylinder 6) on the same bank with cylinder 4. The results are shown in Figure 42 and Figure 43.

From the Figure 42 and Figure 43, the results show that applying the cylinder pressure model based on experiment data from cylinder 4 could obtain very accurate prediction for the other cylinders. It validates the adaptive ability of this semi-physical cylinder pressure model. It is very important for the production engine application because this cylinder pressure model could adapt to production engines with small differences from manufacturing.

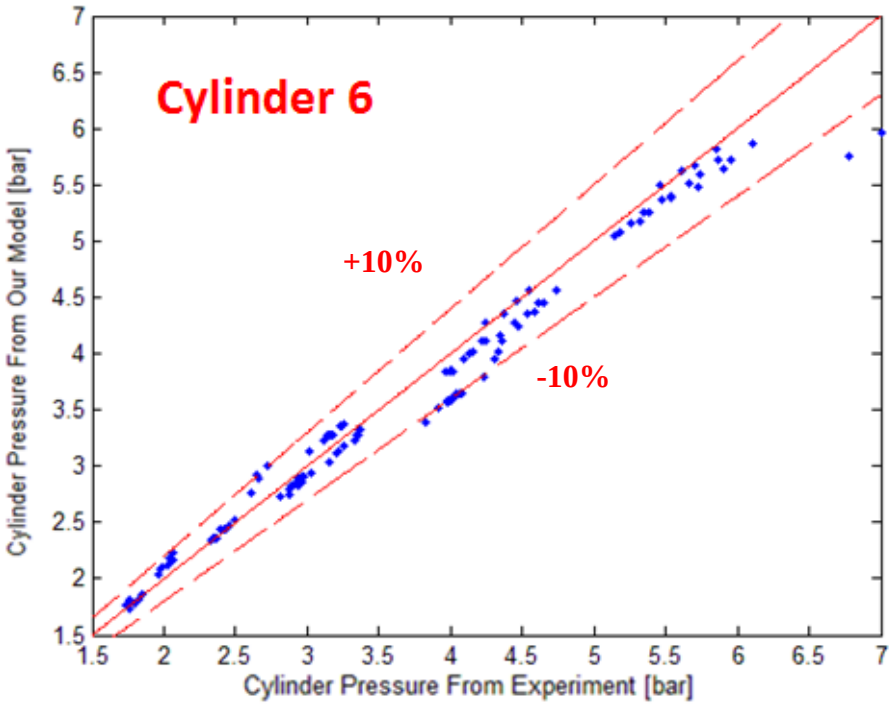

Figure 43: Semi-physical cylinder pressure prediction model validation for cylinder 6

3.2.2.5 In-cylinder mixture temperature model

Based on Ideal Gas Law (Equation (27)), in-cylinder mixture temperature can be calculated from cylinder pressure, in-cylinder mass, cylinder volume and gas constant R.

$$PV = mRT \tag{27}$$

Cylinder pressure can be predicted based on the semi-physical cylinder pressure model shown above, R is a constant, volume can be calculated from crank angle location and in-cylinder mass consists of intake air (from existing ECU prediction model), fuel (from existing ECU model) and residual gas (from previous RGM model).

After obtaining the data for required inputs, we can use Equation (19)-(21) to predict the laminar flame speed.

3.2.3 Turbulence Intensity Prediction Model

Turbulence Intensity u' is defined as the root-mean-square of the turbulent velocity fluctuations in cylinder. It is critical for the combustion and flame propagation for spark ignition engines [68-70]. For example, the quasi-dimensional flame entrainment combustion model, turbulence intensity is an important term in both flame entrainment and burn up periods [39].

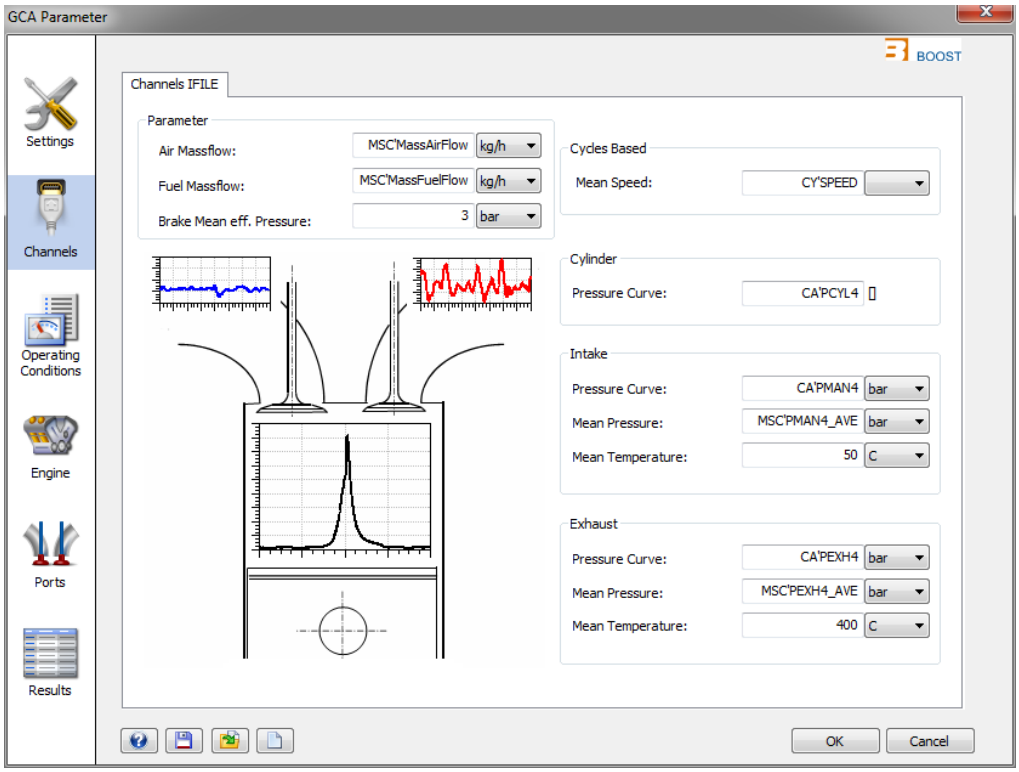

Figure 44: Input channel setting page of AVL GCA.

The turbulence intensity reference values are generated from AVL Concerto GCA. GCA is mainly applied to realize Combustion Analysis and Gas Exchange Analysis by using measured manifolds pressures, cylinder pressures, fuel flow and engine

geometry parameters, as in Figure 44. For GCA, it uses experiment data to calculate turbulence intensity by applying the widely used physical based K-k equation (energy cascade) [70]. This method is a turbulence energy cascade model: the mean flow kinetic energy is supplied into the cylinder chamber from valves and converted into turbulent kinetic energy through the turbulence dissipation. Then, the turbulent kinetic energy is converted into heat through the viscous dissipation progress. The model equations are shown below (Equation (28)-(31)).

$$\frac{dK}{dt} = \frac{1}{2}\dot{m}_{in}{u_{in}}^2 - P + K\frac{\dot{m}_{ex}}{m} + K\frac{\dot{\rho}_u}{\rho_u} \tag{28}$$

$$\frac{dk}{dt} = P - m\varepsilon + k\frac{\dot{m}_{ex}}{m} + k\frac{\dot{\rho}_u}{\rho_u} \tag{29}$$

$$P = 0.3307 c_t \frac{K}{L}\sqrt{\frac{k}{m}} \tag{30}$$

$$K = \frac{1}{2}mU^2 \quad k = \frac{3}{2}mu'^2 \quad \varepsilon = \frac{u'^3}{L} \tag{31}$$

In Equation (28), K is the mean flow kinetic energy, $\dot{m}_{in}$ is the gas mass from intake valves and $\dot{m}_{ex}$ is gas mass flow out of cylinder through exhaust valves. u_{in} is the gas flow velocity into the cylinder, $\dot{\rho}_u$ is the unburned gas density and P is the turbulence production term. Similarly, in Equation (29), it shows the time rate of change of turbulent kinetic energy. There m is in-cylinder total mass and ε represents turbulent dissipation rate which is decided by the turbulence intensity and geometric length scale.

3.2.3.1 Model Description

The physical based control-oriented turbulence intensity prediction model consists of two parts: the first part (shown as the blue in Figure 45 is a semi-physical turbulence intensity prediction model for early combustion stage, for example CA0-CA10. The red box in Figure 45 represents a physical based crank resolution turbulence intensity prediction model which is applied to calculate turbulence intensity values for the rapid combustion period. The aim of this two-stage turbulence intensity model is to simplify the model calculation process but still maintain the accuracy of the model.

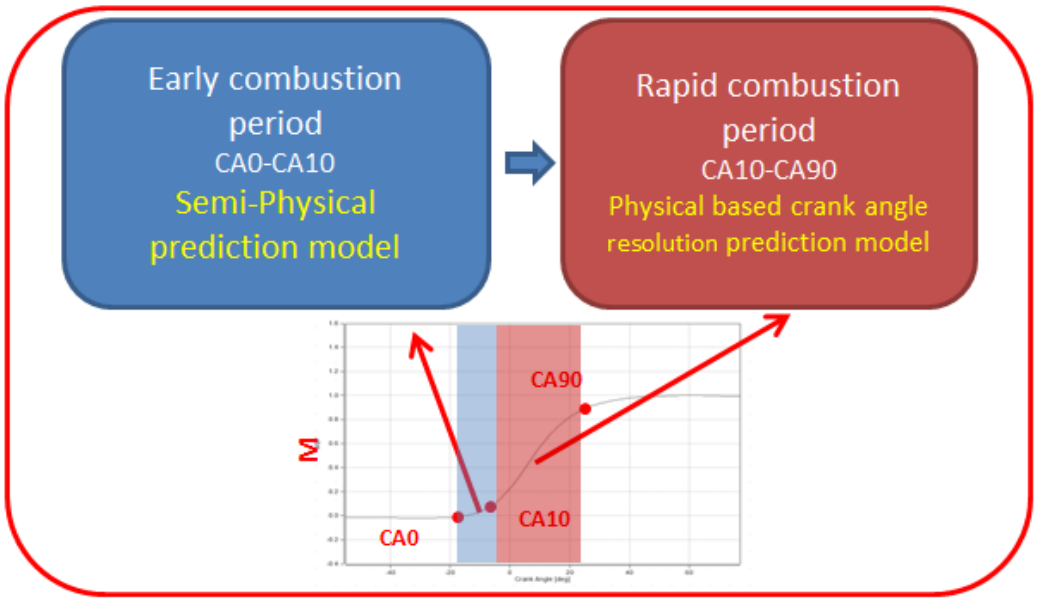

Figure 45: Physical based control-oriented turbulence intensity prediction model algorithm

3.2.3.2 Stage 1: Semi-physical Turbulence Intensity Model

The semi-physical turbulence intensity model for early combustion stage, it refers to the crank angle resolution turbulence intensity values from GCA calculation by using

experiment data to analyze how the important physics (Figure 46) affect the value of turbulence intensity under early combustion stage.

The reference turbulence intensity value at early combustion stage is the average of turbulence intensity values from CA05-CA10 because Prucka [68] mentioned that the turbulence intensity values during the early combustion period is relatively very stable and this trend can be seen in Figure 47. After obtaining the reference turbulence intensity values, the next section will separately show the physics effects on the turbulence intensity and equations used to model all these physics effects.

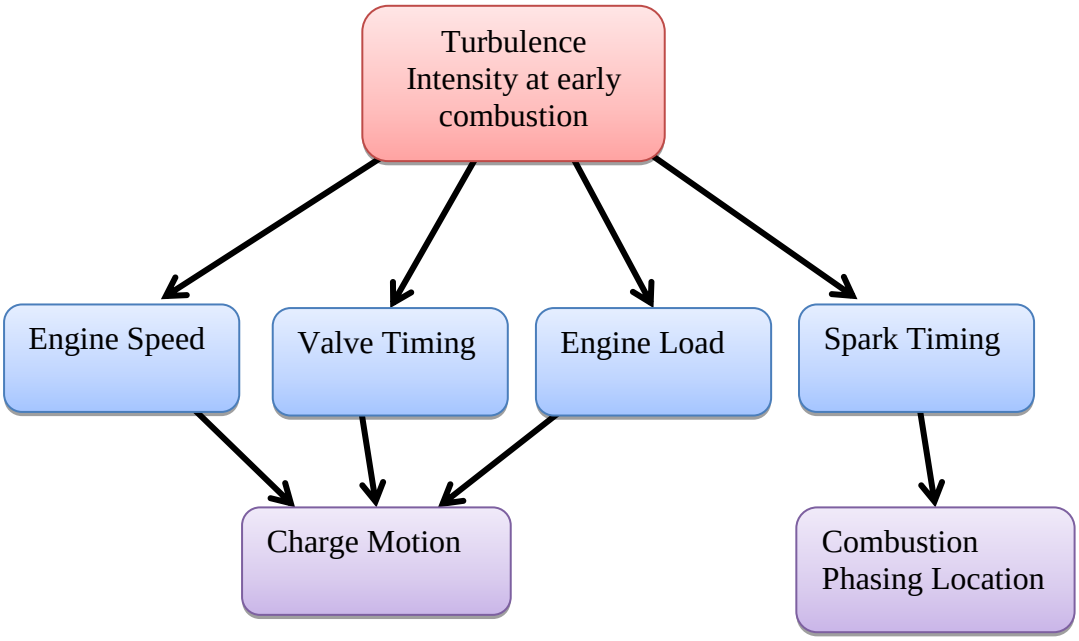

Figure 46: Important physics for turbulence intensity at early combustion

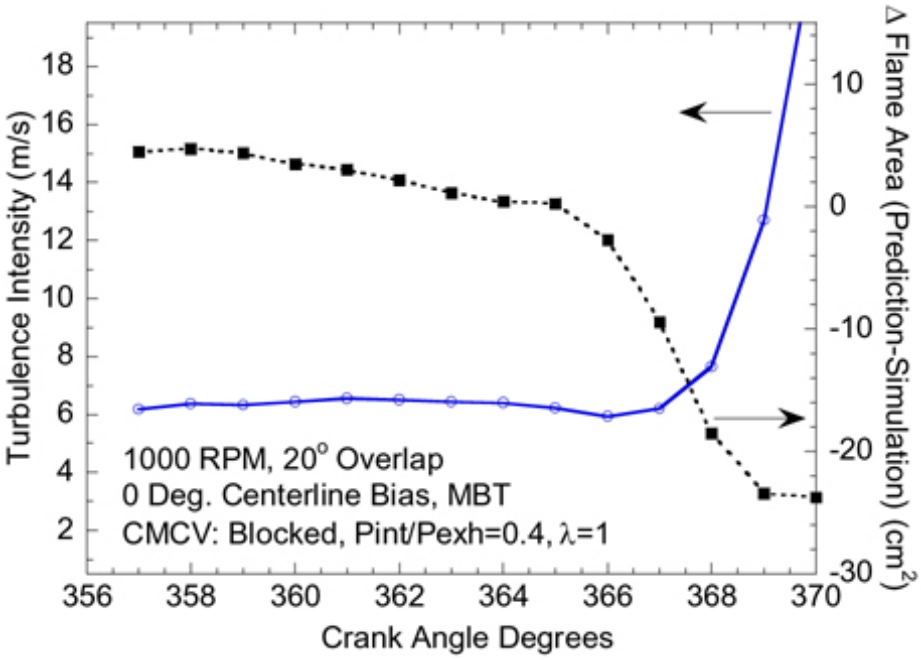

Figure 47: Back-calculated turbulence intensity

The engine effect on the turbulence intensity at early combustion: it is known that the piston motion has strong effect on the gas flow in cylinder. Higher engine speed means more gas will be sucked into cylinder in a certain time period and gas flow velocity across valves will be higher. The increased intake flow velocity and heavier in-cylinder gas motions lead to higher turbulence intensity at early combustion stage. In Figure 48, for different MAPs, turbulence intensity has a relative linear relationship with engine speed and higher mean piston speed will increase the value of turbulence intensity at the beginning of combustion. Based on this trend, the engine speed effects on turbulence intensity can be modeled (Equation (32)), then the turbulence intensity prediction model which only captures engine speed effects (at some certain engine operation conditions) is shown as Equation (33).

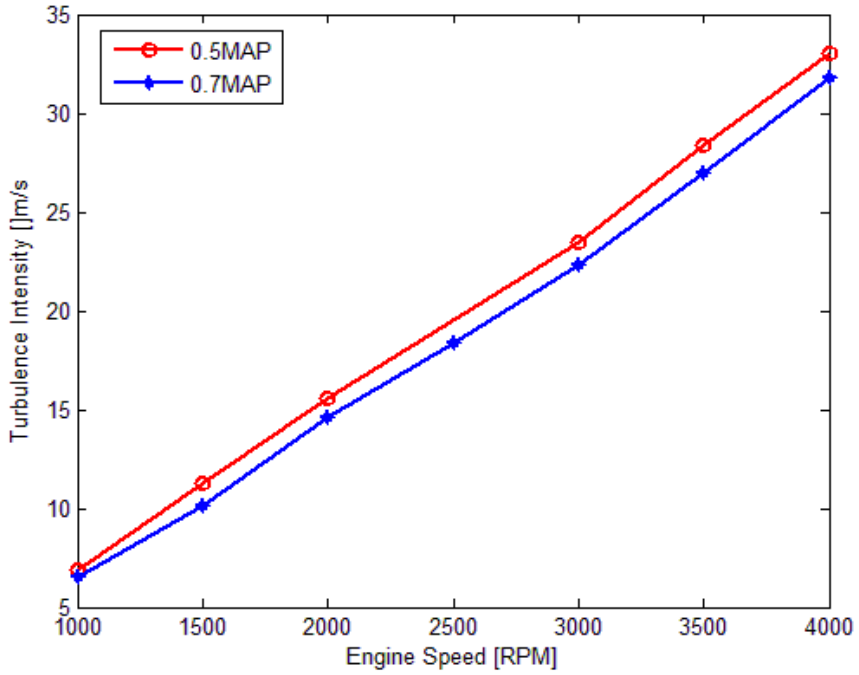

Figure 48: Engine speed effects on turbulence intensity under different MAPs

$$Slope_{RPM} = 0.008378 \tag{32}$$

$$TI_{RPM} = 0.008378 \cdot RPM - 2.275 \tag{33}$$

Secondly, the manifold pressure (MAP) effects on the turbulence intensity. In Figure 49, the MAP effects on turbulence intensity under different engine speed can be seen as a straight line however the slopes are different for each engine speed. Based on the experiment data, the MAP effects can be captured with Equation (34) and the turbulence intensity model added MAP effect is shown as Equation (35).

$$Slope_{MAP} = -(0.0008 \cdot RPM + 1.902) \tag{34}$$

$$TI_{MAP} = TI_{RPM} + Slope_{MAP} \cdot (MAP - 0.5) \tag{35}$$

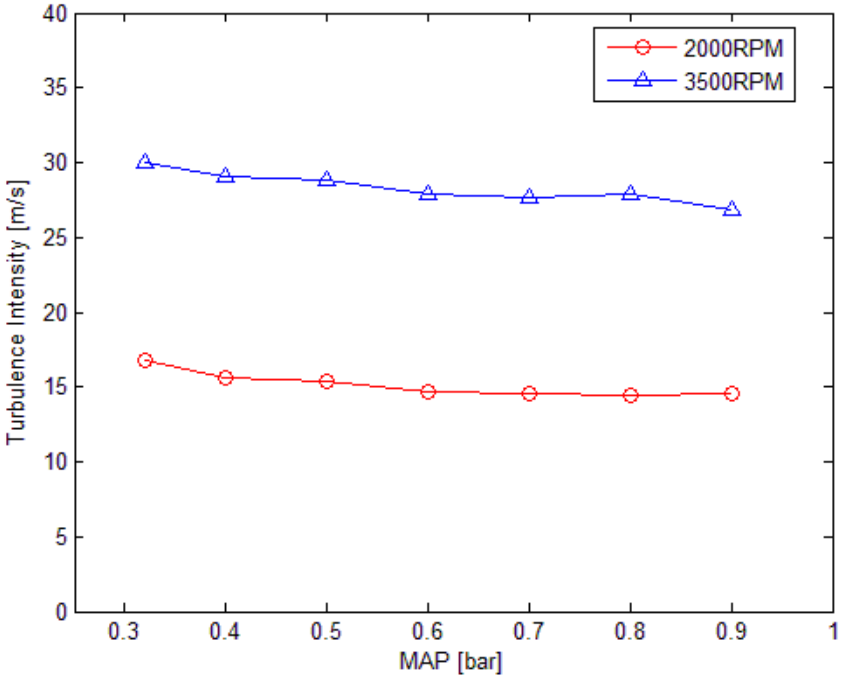

Figure 49: Manifold pressure effects on turbulence intensity with different engine speeds

Spark timing is another important physical effect on turbulence intensity. In

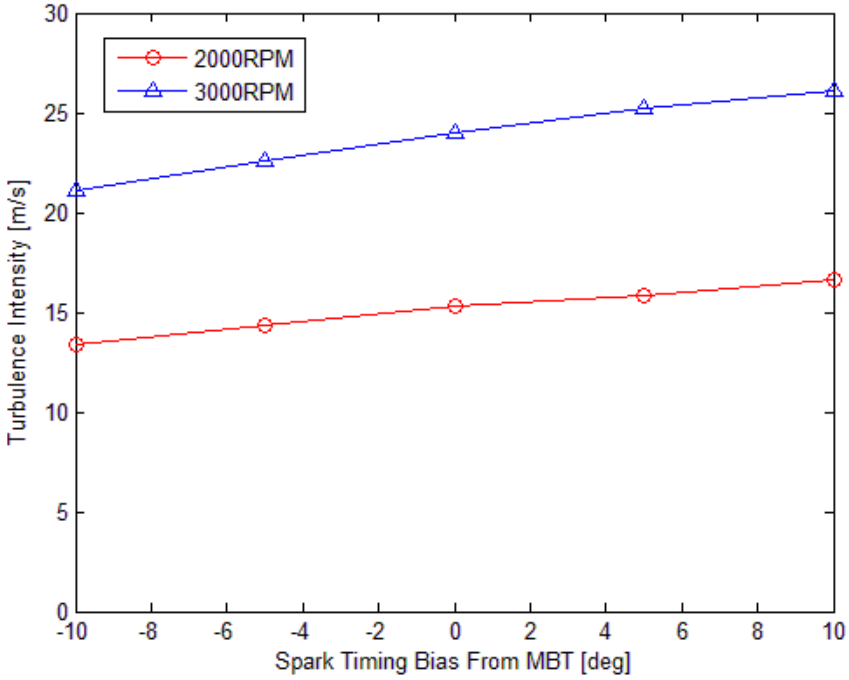

Figure 50, spark timing bias is the spark timing difference from MBT spark timing. The unit of spark timing bias is degree and positive value means advancing spark from MBT spark timing. From

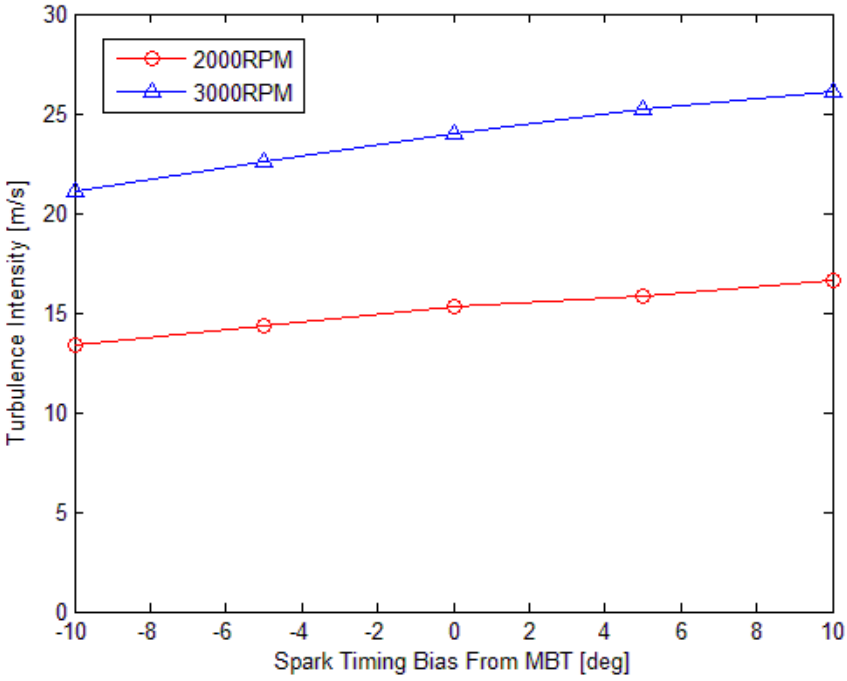

Figure 50, the spark timing bias has a relatively linear relationship with turbulence intensity and advancing spark from MBT sparking timing leads to higher turbulence intensity values. When advance the spark, the combustion will happen relatively earlier, so the cascade of the turbulent kinetic energy will be less and there will be higher turbulence intensity. Similarly, based on the experiment data, the spark bias can be modeled (Equation (36)) and the updated turbulence intensity model with spark effect is shown as Equation (37).

$$Slope_{SPK} = 0.000096 \cdot RPM - 0.0353 \tag{36}$$

$$TI_{SPK} = TI_{MAP} + Slope_{SPK} \cdot (SPK - SPK_{MBT}) \tag{37}$$

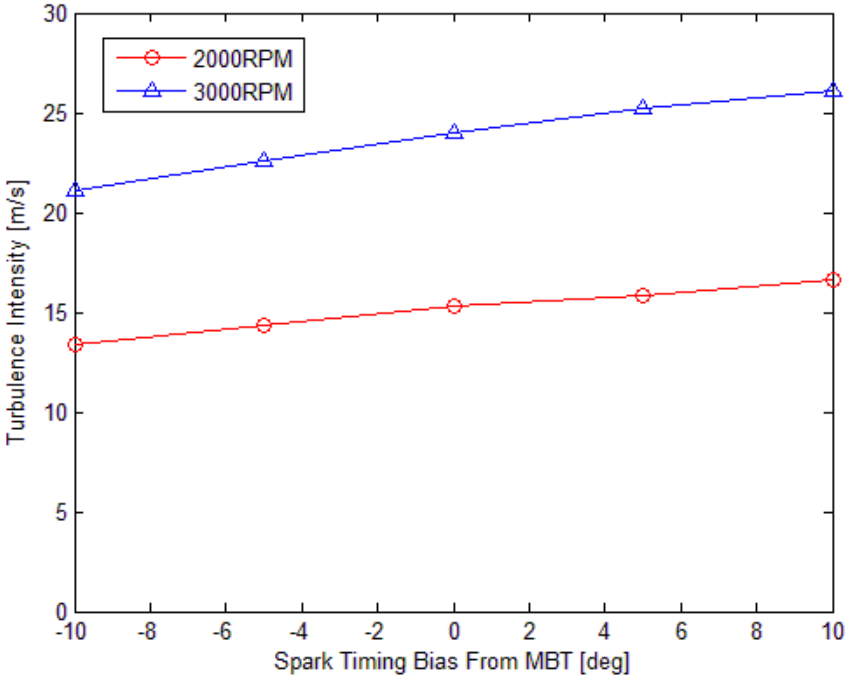

Figure 50: Spark Timing Bias effects on turbulence intensity under different engine speeds

The valve timing effects (Figure 51) on turbulence intensity is mainly the intake valve closing (IVC) timing effects on turbulence intensity because the location of IVC will affect the intake gas flow condition together with piston motion.

After capturing all the important physical factors' effects on turbulence intensity at early combustion stage, this semi-physical turbulence intensity prediction model is finished. To validate the accuracy of the model, Figure 52 and Figure 53 shows the turbulence intensity comparison between this semi-physical model and reference data set.

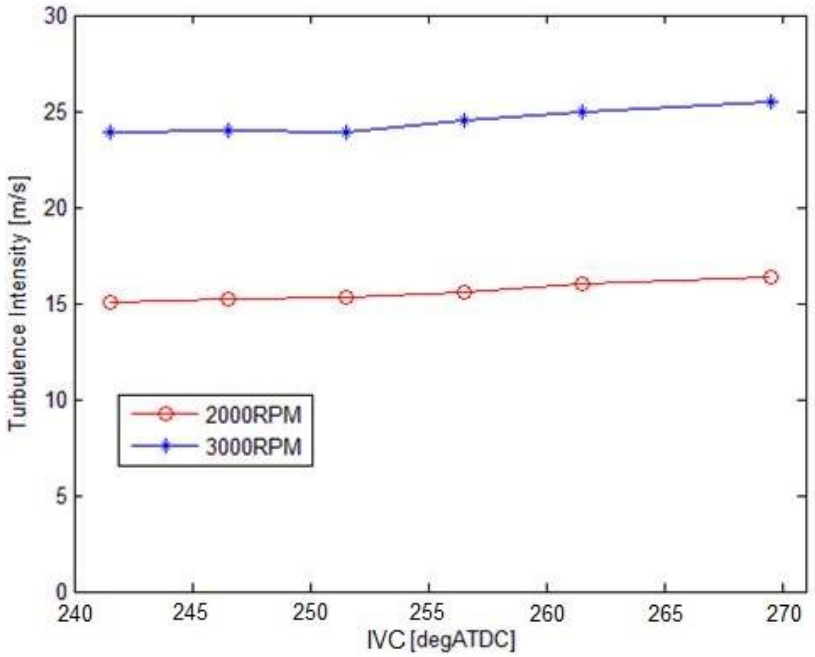

Figure 51: Intake valve timing effects on turbulence intensity under different engine speeds

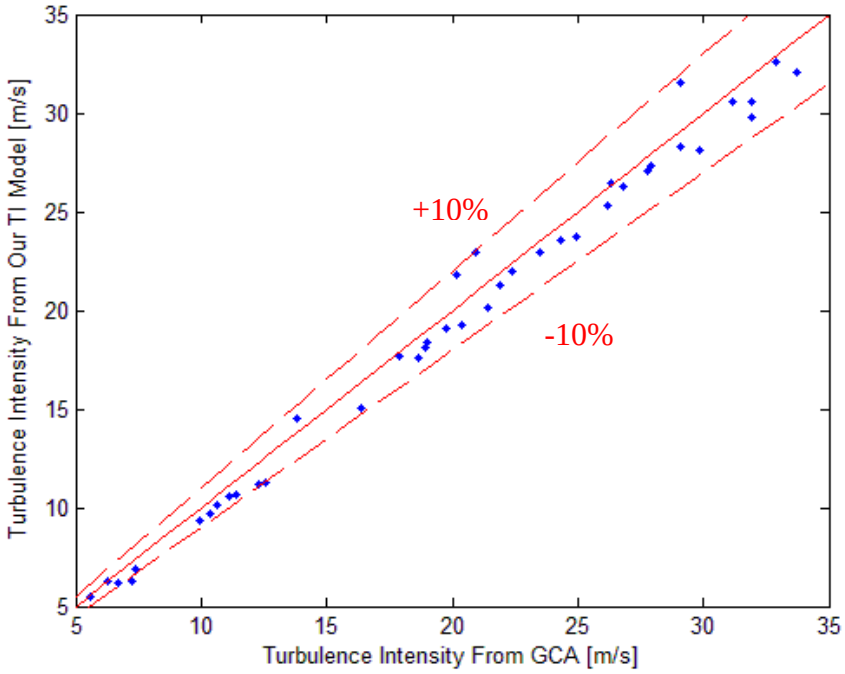

Figure 52: Turbulence intensity prediction model validation (modeling data set)

Data in Figure 52 are the same data used for the modeling. Solid red line is the ideal 0 error line and two red dash lines represents the +10% and -10% error limitation. The comparison results shown in Figure 52 could validate the accuracy of the turbulence intensity prediction model.

Data in Figure 53 are validation data which are totally different from the modeling data. As before, solid red line is the ideal 0 error line and the two red dash lines represents the +10% and -10% error limitation. The comparison results shown in Figure 53 verify the accuracy of the prediction model.

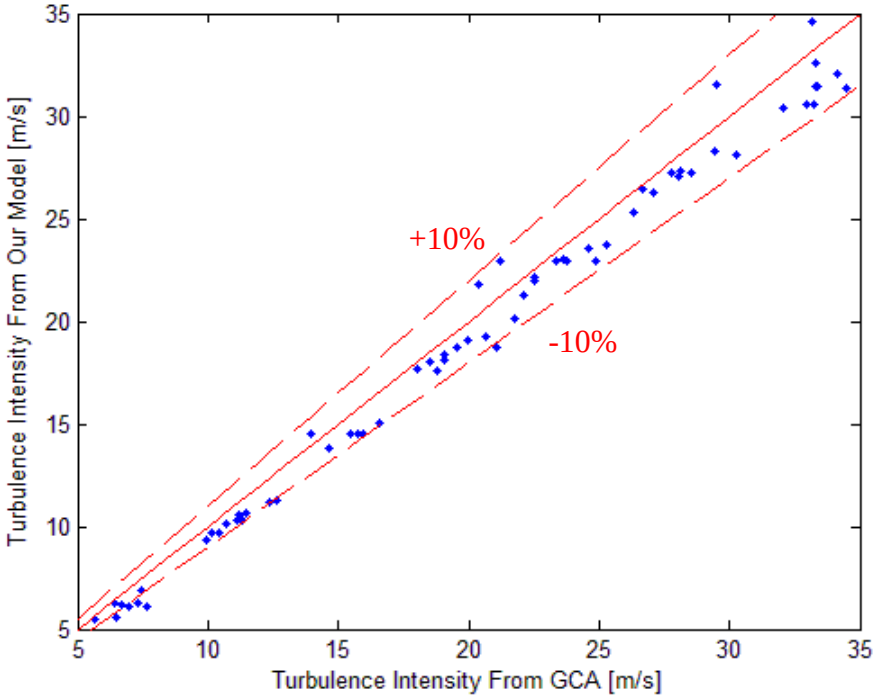

Figure 53: Turbulence intensity prediction model validation (validation data set)

3.2.3.3 Stage 2: Physical Based Crank Angle Resolution Turbulence Intensity Model

When the combustion begins and gets into the rapid burn period, crank-angle by crank-angle turbulence intensity values are required as an important input for the combustion model. Here the crank angle resolved turbulence intensity model is based on the K-k equations and simplified for the rapid burn combustion period.

According to Poulos [70], the production term in Equation (30) is assumed to be zero, which means there is no turbulence kinetic energy generated from mean flow kinetic energy. During the combustion period, valves are closed, so there is no mass flow in or out of cylinder and the mass flow rate term becomes zero. The unburned gas density can be calculated based on the combustion progress and flame propagation.

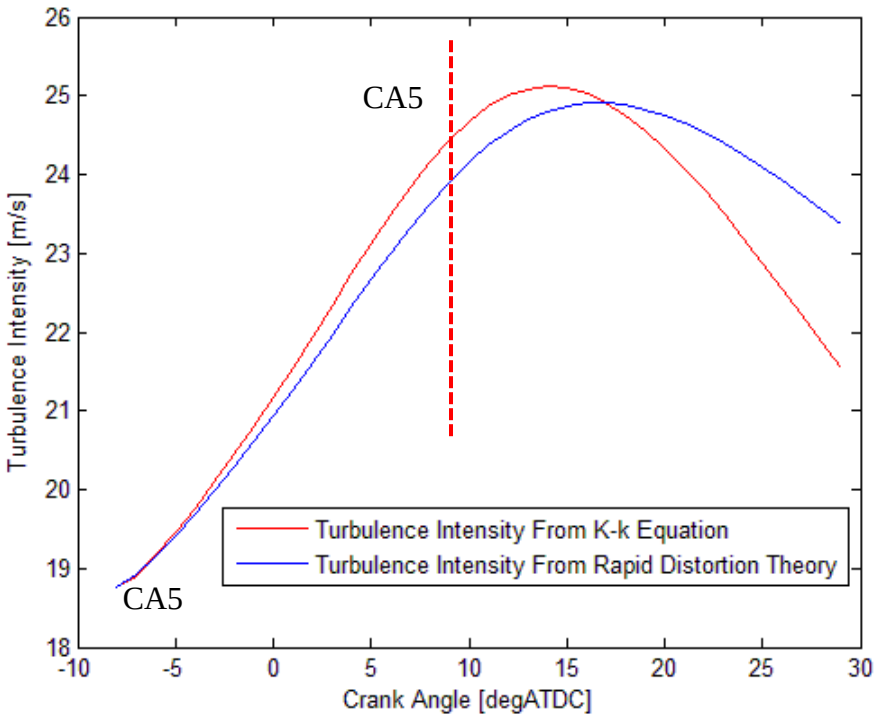

Figure 54: Turbulence intensity model prediction from two models

According to Heywood [1], after combustion begins, the unburned gas density is four times as burned gas density. This assumption helps resolve burned and unburned gas density based on gas burned mass and instantaneous cylinder volume. In Figure 54, the red curve shows an example of the crank angle turbulence intensity calculation results. The blue curve in Figure 54 shows the turbulence intensity results from another kind of turbulence intensity prediction model which is based on the rapid-distortion theory proposed by Tabaczynski [34]. The rapid-distortion theory is a statistic theory and it ignores interactions between eddies [35]. Compared with turbulence energy dissipation model (K-k equations), the rapid-distortion theory assumes the turbulence dissipation to be zero which means the $m\varepsilon$ term in Equation (30) is zero. This assumption brings in some error for sure, but due to its simple form and small computational effort, it is very popular and widely applied. The turbulence intensity calculation results from two models show that from the start of combustion to CA50, where we focus the most, the two models' prediction results are close.

3.2.4 Flame Front Area

For this research the flame is assumed to propagate spherically from the spark plug gap through the unburned mixture. The flame will contact the cylinder head, piston and cylinder walls with increasing burned gas radius. Based on geometric calculations, the flame front area is defined by Equation (38).

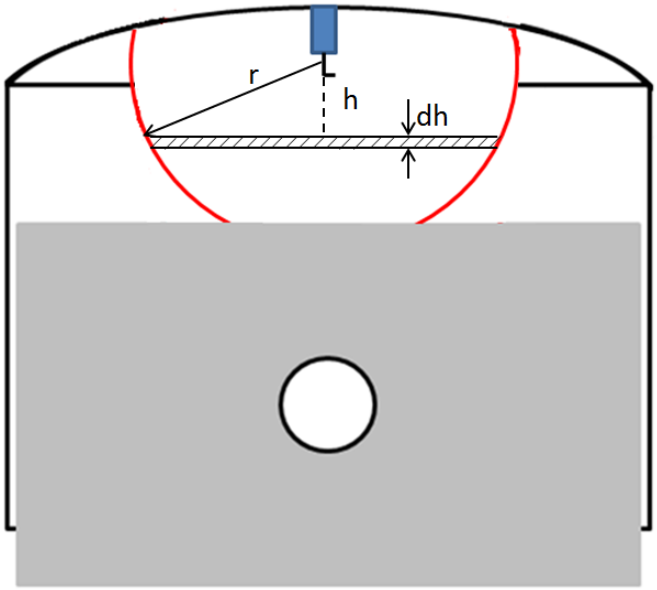

Figure 55: Flame geometry and contact with cylinder

$$A_{flame} = \int 2\pi\sqrt{r^2 - h^2} \cdot dh \tag{38}$$

As shown in Figure 55, r is the flame radius and h is the distance to the flame center. Flame front area can be calculated by integrating circular band areas with height dh. In this research, flame thickness is assumed 3mm and the flame radius r can be calculated from burned gas radius r_b plus flame thickness. Burned gas radius has a relationship with burned gas volume as shown in Equation (39). Burned gas volume is calculated from burned mass and burned mixture density.

$$V_b = \int \pi(r_b^2 - h^2) \cdot dh \tag{39}$$

In order to reduce computational effort by crank angle-by-crank angle burned gas radius and flame front area calculation, an artificial neural network is trained for burned gas radius prediction and flame front area at each crank angle is interpreted from a geometrically calculated lookup table (Figure 56), which is based on Equation (38).

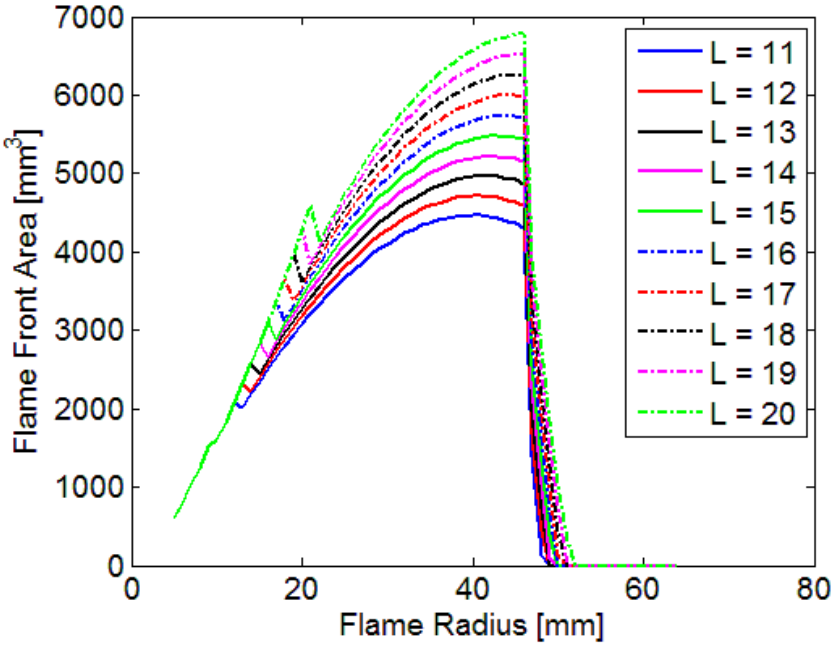

Figure 56: Flame front area lookup table

3.2.5 Unburned Gas Density

After start of combustion, the in-cylinder mixture can be separated into burned and unburned zones. According to Heywood, unburned gas density is approximately four times that of the burned gas [1]. Based on this assumption, unburned gas density can be calculated by Equation (40).

$$\rho_{unburned} = \frac{m_{total} + 3m_b}{V} \tag{40}$$

CHAPTER FOUR

MODEL BASED ENGINE COMBUSTION PHASING PREDICTION

The previous chapters have described the critical input models for the combustion prediction. In this chapter a quasi-dimensional turbulent flame entrainment rate model based combustion phasing prediction algorithm is proposed and the validation results are presented.

Different from the previous work from other researchers [1,2,43,70], in this research, the combustion phasing prediction is separated into two stages. The first stage calculates the duration from spark to start of combustion (SOC) (defined by CA00, or when heat release is first observed) and the second stage computes the flame propagation event after CA00. This two-stage combustion phasing prediction structure has two key advantages (over a single stage combustion approach) for real-time control applications; (1) reduced computational effort for both the flame propagation and flame kernel development stages, (2) improved the accuracy of the duration of each stage.

4.1 Flame Kernel Development Duration Prediction

For SI engines, the flame starts from a spot, called flame kernel and then propagates outwards to the unburned area. The start of combustion does not happen right after spark. Instead, there is a period between spark and CA00 where only a little unburned mixture is burned and the cylinder pressure has not been affected yet by the heat release. This period is called the flame kernel development process. In the flame

kernel development period energy is accumulated and the unburned mixture around the kernel is heated.

Quasi-dimensional or one dimensional SI combustion models are difficult to apply during the flame kernel development period due to the very small burned mixture during that period. Previous researchers used experimentally calibrated flame front area lookup tables to match the flame kernel development duration from spark to start of combustion [2][43], but the results are not promising. In this research, the quasi-dimensional combustion model is only applied from the start of combustion and the duration from spark to CA00 is predicted from the flame kernel development model.

4.1.1 Energy Based Physical Flame Kernel Models

Energy balance based physical flame kernel models consider thermodynamic and chemical energy [71][73]. These models account for all fundamental properties of the ignition system, for example; supplied electrical power and energy, energy transfer efficiency to spark plasma, discharge mode, plasma temperature distribution, heat losses to electrodes and chamber walls and gaps width. They also consider combustible mixture properties, for instance pressure, temperature, air fuel ratio, residual gas fraction, laminar flame speed and fuel type. Flow field properties such as; mean flow velocity, turbulence intensity, characteristic time, strain and length scales are accounted as well. The flame kernel model is based on the strained flamelet combustion model or turbulent flame entrainment combustion model and predicts kernel growth consistently under various relevant physical/chemical conditions.

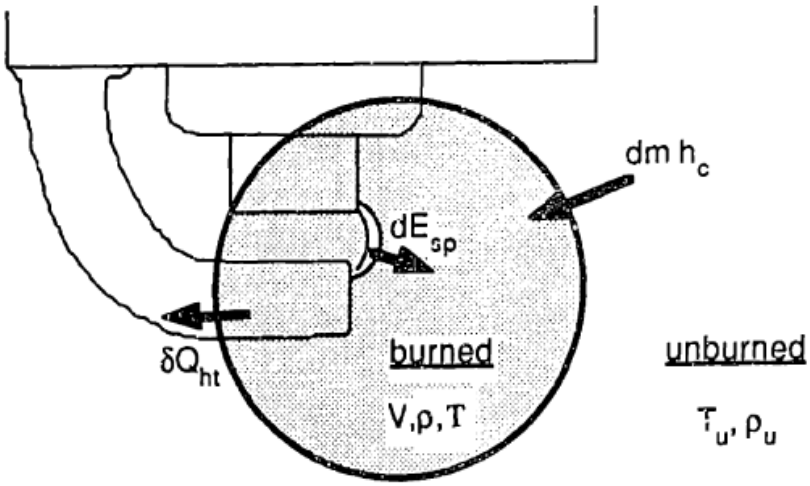

Figure 57: Spark ignition engine flame kernel energy distribution (Figure comes from [71])

Figure 57 show the SI engine flame kernel energy distribution. Spark energy from the electrode transfers to the spark plug and becomes accumulated energy in the flame kernel. Based on the First Law of Thermodynamics, the energy balance is shown as Equation (41).

$$-\delta Q_{ht} + dE_{sp} - pdV + dmh_c = dU \tag{41}$$

Where Q_{ht} is the heat transfer loss to spark plug. E_{sp} is energy from the spark. p is flame kernel mixture pressure and V is kernel volume. m is kernel mass and hc is heat capacity. This detailed energy balance flame kernel model demonstrates relatively accurate prediction results. However, this process requires relatively high calculation effort and is not suitable for the real-time combustion phasing calculation.

4.1.2 Control Oriented Flame Kernel Development Model

For this project, a control oriented flame kernel development model is required to realize the real-time spark to CA00 duration prediction. Different from the crank angle resolution flame kernel development models, the control oriented model needs to be

simplified for real-time application. In the meantime, the critical physics have to be considered and applied to the model to increase the physical meaning and adaptive ability of the model. In this research, two kinds of control oriented flame kernel development models will be shown.

4.1.2.1 Semi-Physical Neural Network Based Flame Kernel Development Prediction

The first control-oriented flame kernel development model is based on an artificial neural network (ANN). Different from the regular ANN which is a kind of a "Black Box" model, the semi-physical ANN proposed in this project is a physics-based "Grey Box" model, where the input is not simply the operating conditions. Instead the inputs are physics that are critical for flame kernel development. The critical physics are selected by sensitivity analysis and the finalized set of physical parameters are cylinder pressure, unburned gas density at spark timing and engine speed, fuel injected and residual gas fraction. Then these physical parameters are used as the inputs, and the crank angle duration from spark timing to CA00 is generated as an output from the ANN. About 300 steady-state operating points were used to train the ANN, Figure 58 and Figure 59 show the ANN training results.

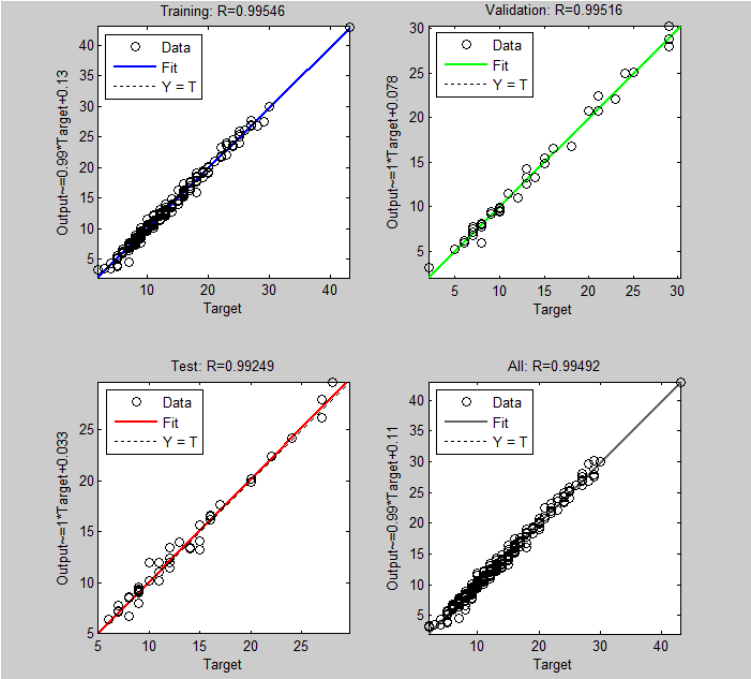

Figure 58: Semi-physical neural network training results

Results

	Samples	MSE	R
Training:	201	3.50428e-1	9.95464e-1
Validation:	43	4.80215e-1	9.95156e-1
Testing:	43	5.78813e-1	9.92492e-1

Figure 59: Semi-physical neural network training, validation and testing results

For this semi-physical ANN, only three neurons are used to train the network. Three neurons could guarantee the stability of the ANN prediction. The training results show this control oriented flame kernel development model could give very accurate prediction results (R is 0.995) and the computational effort for the ANN is relatively very small.

4.1.2.2 Semi-Physical Single Step Flame Kernel Development Model

The second control oriented flame kernel development model in this project is a semi-physical single step model. It is relatively more physical and therefore clearer for engineers. This model also uses the critical physics as shown in the previous section and the model equation is shown below.

$$Duration_{SPK-CA00} = e^{k0} \cdot {P_{SPK}}^{k1} \cdot {\rho_{SPK}}^{k2} \cdot RPM^{k3} \cdot {M_{fuel}}^{k4} \cdot RGF^{k5} \quad (42)$$

P_{SPK} is the cylinder pressure at the spark timing, and ρ_{SPK} is unburned gas density at the time of spark. RPM is engine speed, M_{fuel} is injected fuel and RGF is residual gas fraction. The same data set is used to calibration the constants (k0~k5) in the semi-physical single step flame kernel development model and Table 4 shows the calibrated constants.

Table 4: Calibrated constant for the single step flame kernel development model

k0	k1	k2	k3	k4	k5
13.62	-0.126	-1.817	-0.0041	2.098	0.422

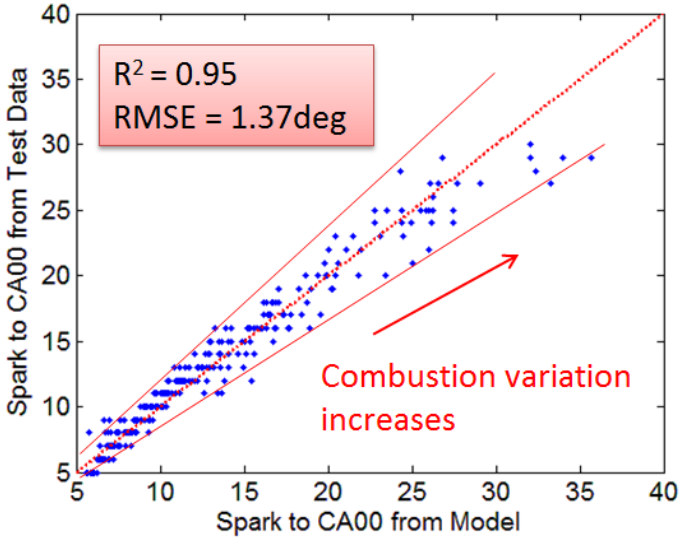

Figure 60: Semi-physical single step flame kernel development model validation result

Calibrated model validation results are shown in Figure 60. The x-axis is crank angle duration from spark to CA00 from the model prediction results and y-axis is that from test data. R^2 is 0.95 and the root-mean-square-error (RMSE) is 1.37 crank angle degrees.

4.2 Physical Model Based Combustion Phasing Prediction

Once all the required input models are ready, the main task for the implementation of the physical models for combustion phasing prediction is to correctly integrate all the input models together and setup the algorithm. In this section, the combination steps are described in detail.

According to chapter 3, the quasi-dimensional turbulent flame entrainment combustion model is mainly consisted of two steps: unburned mixture entrained into small eddies and then the entrained eddies burn in a characteristic time. The two equations (Equation (1) and Equation (2)) show entrainment rate and burning rate for this combustion model. In the first equation, the inputs are flame front area (Chapter 3.2.4 Flame Front Area), unburned gas density (Chapter 3.2.5 Unburned Gas Density), laminar flame speed (Chapter 3.2.2 Laminar Flame Speed Prediction Model) and turbulence intensity (Chapter 3.2.3 Turbulence Intensity Prediction Model). The gas density and laminar flame speed models, they require cylinder pressure as input. However, the cylinder transducer is not available for most production engines. A cylinder pressure calculation model is needed. In Chapter 3 section 3.2.2 Laminar Flame Speed Prediction Model, a cylinder pressure at IVC and pressure during compression stroke prediction model is proposed. But after the start of combustion, the burned gas releases energy

which could significantly increase the cylinder pressure. To capture this phenomenon, a thermodynamic first law based cylinder pressure calculation model is described below.

In Equation (43), P_{cyl} is cylinder pressure, V_{cyl} is instantaneous cylinder volume, n_{comb} is polytrophic coefficient during combustion and Q is the combination of heat release from burned mixture and heat transfer loss.

Heat transfer loss is calculated based on Woschni heat transfer model [74] and the model is defined by Equation (**44**). h_c is convective heat transfer coefficient, A is surface area, T_g is gas temperature and T_w is wall temperature.

$$\dot{P}_{cyl} = -\frac{n_{comb} P_{cyl}}{V_{cyl}} \dot{V}_{cyl} + \frac{n_{comb} - 1}{V_{cyl}} \dot{Q} \tag{43}$$

$$\dot{Q}_w = h_c \cdot A \cdot (T_g - T_w) \tag{44}$$

$$\dot{Q}_{fuel} = LHV \cdot \dot{m}_{fuel} \tag{45}$$

$$n_{comb} = \frac{0.2888}{c_v} + 1 \tag{46}$$

$$c_v = 0.7 + T_{cyl} \cdot (0.155 + k) \cdot 10^{-3} \tag{47}$$

Heat release rate from burned mixture can be calculated by Equation (**45**). LHV is fuel lower heating value. For gasoline, LHV is used as 44.7MJ/Kg. $\dot{m}_{fuel}$ is the fuel flow rate. The polytrophic coefficient during combustion can be defined by Equation (**46**). cv is the specific temperature at a constant volume and it is defined as Equation (**47**). T_{cyl} is cylinder temperature and k is a constant and equals to 0.1 for gasoline.

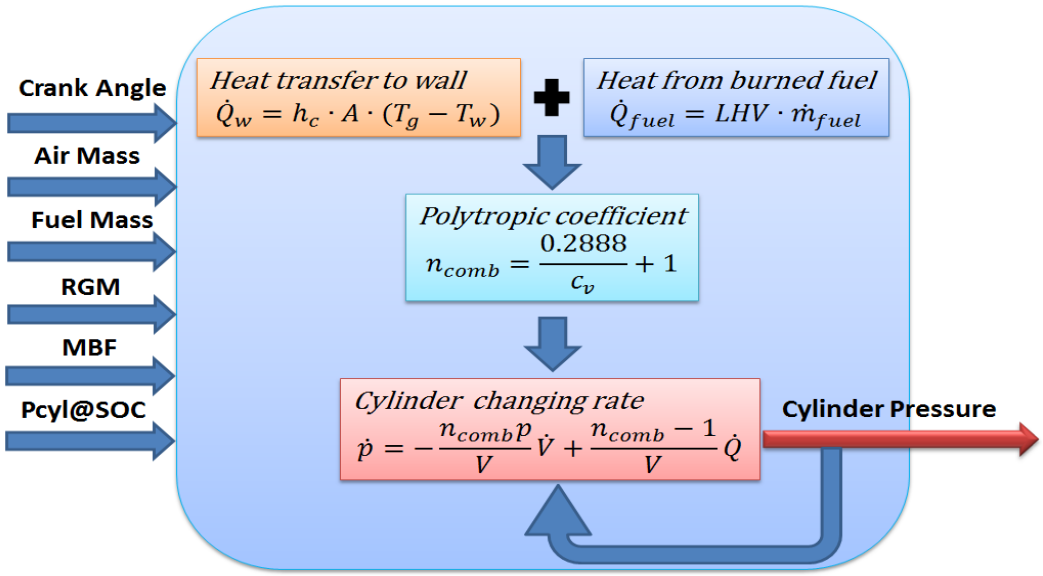

Figure 61: Block diagram of cylinder pressure calculation model

Figure 61 shows the cylinder pressure calculation model. It consists of models for heat transfer, heat release, polytrophic coefficient and cylinder pressure calculation. For instantaneous cylinder pressure calculation, the cylinder pressure value at the start of combustion is calculated from the previous cylinder pressure model for the compression stroke and used as the initial value for cylinder pressure calculation after combustion.

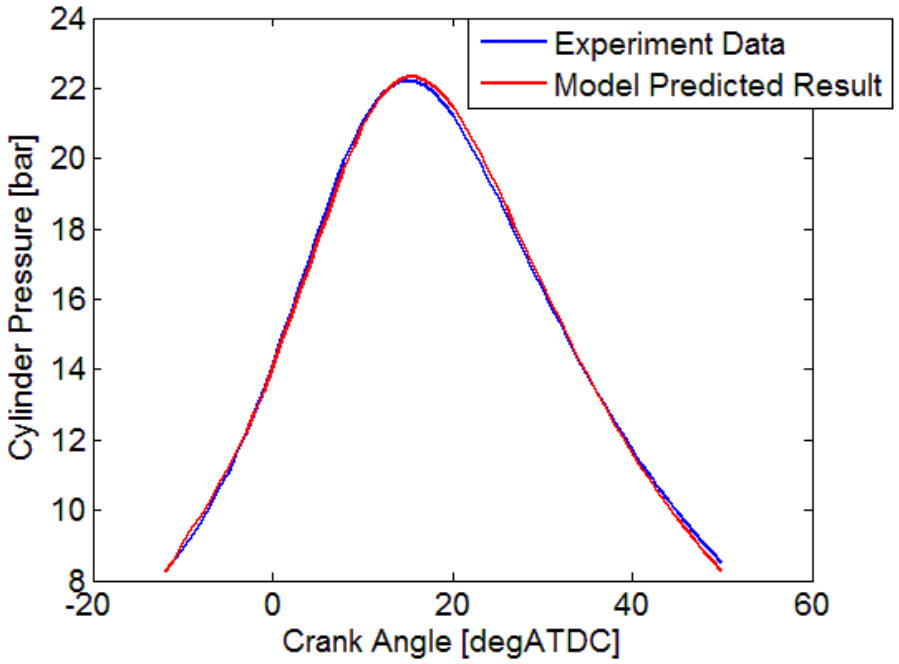

Figure 62: Cylinder pressure calculation comparison result (1500RPM, 0.5 bar MAP, 128ICL, 117ECL, Lambda = 1)

The cylinder pressure comparison result are shown in Figure 62. The blue curve is from experimentally measured data and the red curve is from the cylinder pressure prediction model. Results show the model is capable of accurately representing the cylinder pressure.

The intake air mass and fuel injection mass can be read directly from the ECU (from existing control models and/or sensor measurements) and are not discussed in this project. The residual gas mass is modeled in Chapter 3.2.1 Residual Gas Mass Prediction Model. Instantaneous cylinder volume is calculated based on crank angle location. Flame kernel development model proposed in Chapter 4.1 Flame Kernel Development Duration Prediction predicts the crank angle duration from spark to start of combustion.

All models are combined together to set up the combustion phasing prediction system. Figure 63 shows the layout of the combustion phasing prediction system. Outside of the black box are the flame kernel development model (which gives CA00) and residual gas model (which provides residual gas mass into the combustion model). Both models only need to be run once per engine cycle. Inside the black box, all the models run every crank angle. Combustion model generates burned mass and gives it to the cylinder pressure model to calculate heat release and then the cylinder pressure model feeds cylinder pressure value back to combustion model.

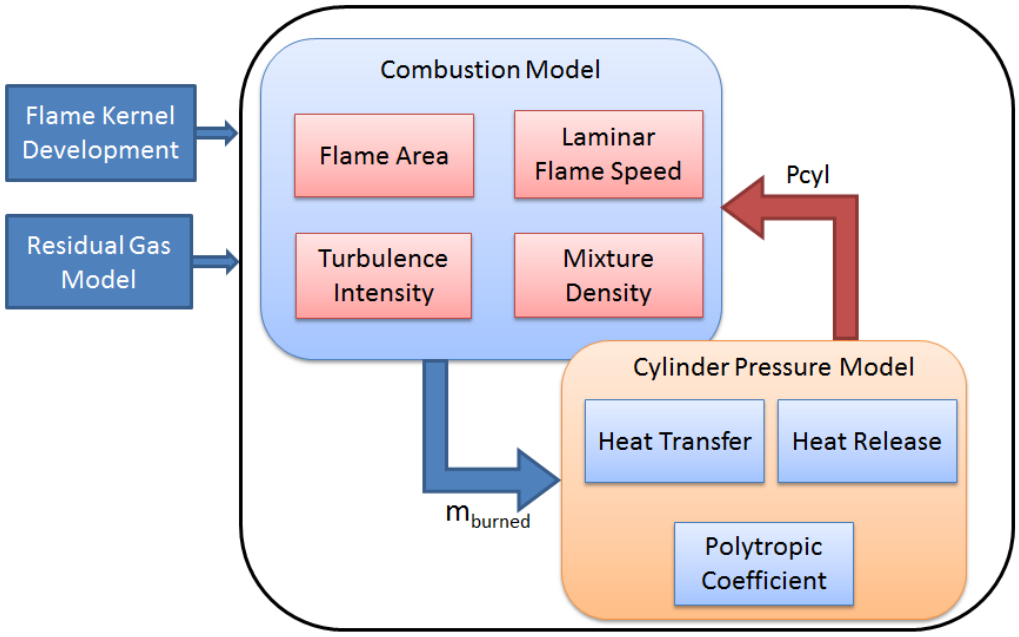

Figure 63: Layout of the combustion phasing prediction system

Figure 64 shows an example of the combustion model prediction results. It is a comparison of burned mass curves between experimental measurements and model predicted results. The combustion phasing prediction system is capable of accurately

calculating rate of heat release and producing mass fraction burned curves. The corresponding cylinder pressure comparison results are shown in Figure 65. The red curve shows the model predicted cylinder pressure and blue curve is from measured data.

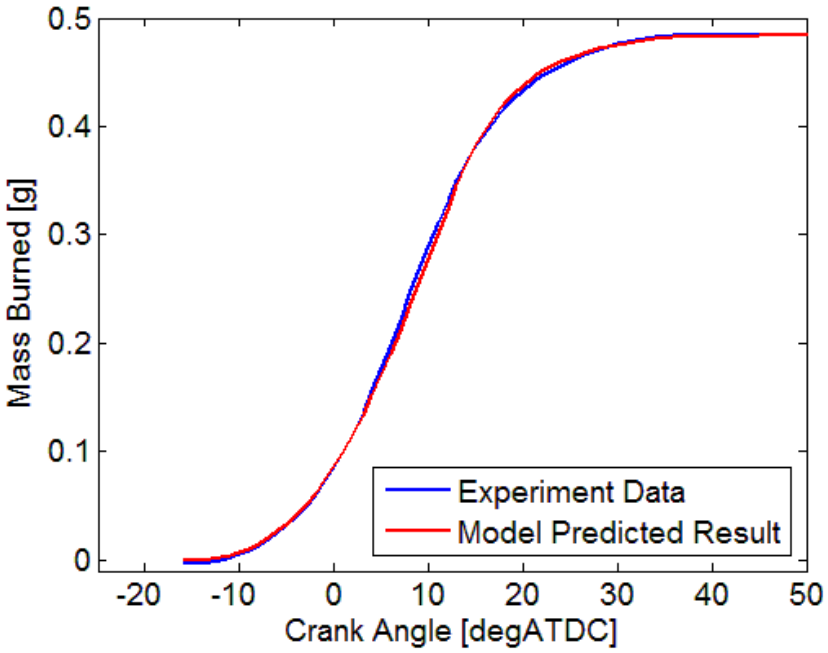

Figure 64: Burned gas mass comparison (3000RPM, 0.9bar MAP, 128ICL, 117ECL, Lambda = 1)

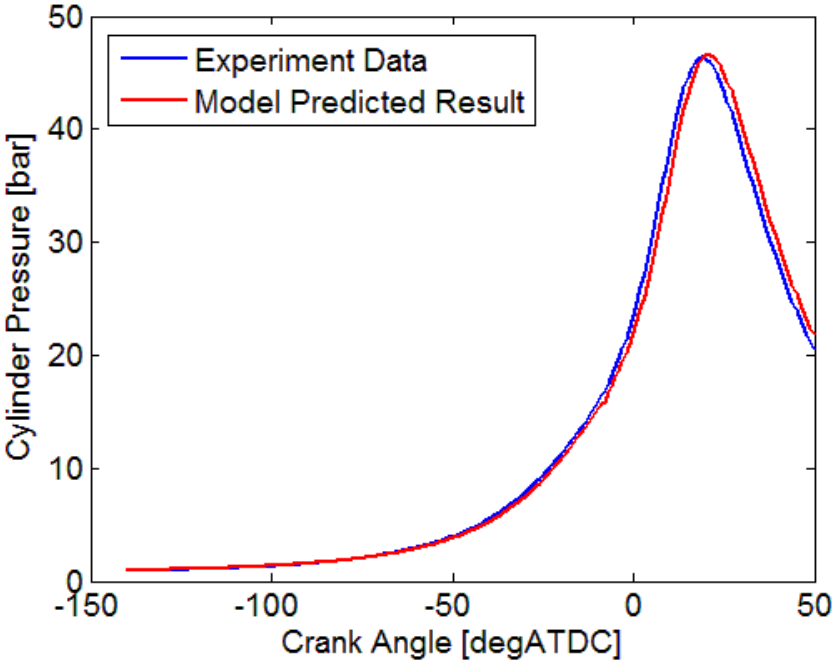

Figure 65: Cylinder pressure comparison (3000RPM, 0.9bar MAP, 128ICL, 117ECL, Lambda = 1)

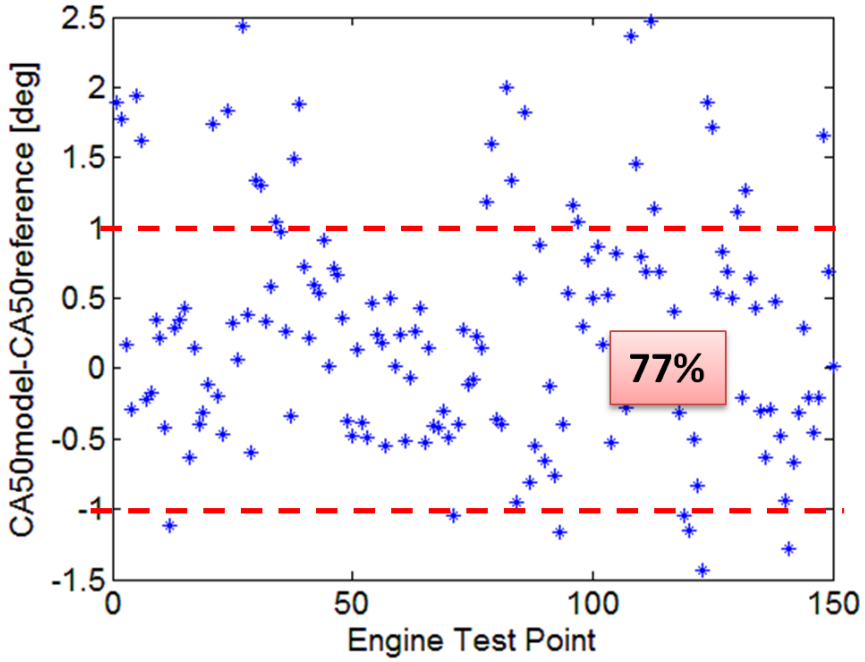

Figure 66: CA50 prediction error under different engine operation conditions (500 engine cycle average values are used for CA50 reference decision under every engine operation condition)

For SI engine combustion phasing control, CA50 (50 % of mixture mass burned crank angle location) is a widely used combustion phasing reference point. So here, CA50 error results are shown in Figure 66. The blue dots are CA50 error values under different engine operation conditions (see Table 5). These offline calculated results show 77% of the predicted CA50 values can be located within a 1 degree error band.

Table 5: Combustion model validation data set operation conditions

Engine Speed	Manifold Pressure	ICL	ECL
1000-3000RPM	0.35-0.95MAP	98-128degATDC	87-117degBTDC

CHAPTER FIVE

COMBUSTION PHASING OPERATIONAL RANGE LIMITATIONS

Combustion phasing is critical for SI engine efficiency, emissions, drivability and durability. To improve engine efficiency, the target combustion phasing point (CA50) should be located around MBT. However, in the meantime, the engine operational range limitations need to be considered to protect the engine. Two primary limitations for SI engines are knock and cycle-to-cycle combustion variability. Advancing combustion phasing increases peak pressures and temperatures in-cylinder, which can lead to abnormal end gas auto-ignition called knock. Heavy knock is dangerous for the engine because the high pressures and temperatures can damage the piston, cylinder wall and cylinder head. Combustion variability happens when the combustion phasing is too advanced or retarded. When the combustion phasing is advanced the compression stroke is far from completion and the cylinder pressure and temperature are relatively low, and under this condition the unburned mixture is relatively more difficult to ignite. On the other hand, when the combustion phasing is retarded, most of the combustion happens during the expansion stroke, the cylinder pressure and temperature keeps decreasing in this period and this exacerbates the impact of combustion variations on pressure and IMEP. The highly variable combustion under these conditions can influence the drivability, emissions, and engine durability. To realize reasonable combustion phasing control, combustion phasing should be limited within the operational limitation range.

5.1 Knock Prediction Model

Abnormal auto-ignition in SI engines can be separated into surface ignition and end gas auto-ignition [1]. The surface ignition is caused by high temperature surfaces in cylinder and is uncontrollable by combustion phasing adjustment. In this project, the end gas auto-ignition type knock is considered. This knock is defined as the unburned end gas auto-ignition before the spark ignited flame reaches, shown in Figure 67. It is mainly caused by the expanded burned gas pressing the unburned end gas to auto-ignition. It happens when the cylinder peak pressure and temperature is very high (combustion phasing is advanced).

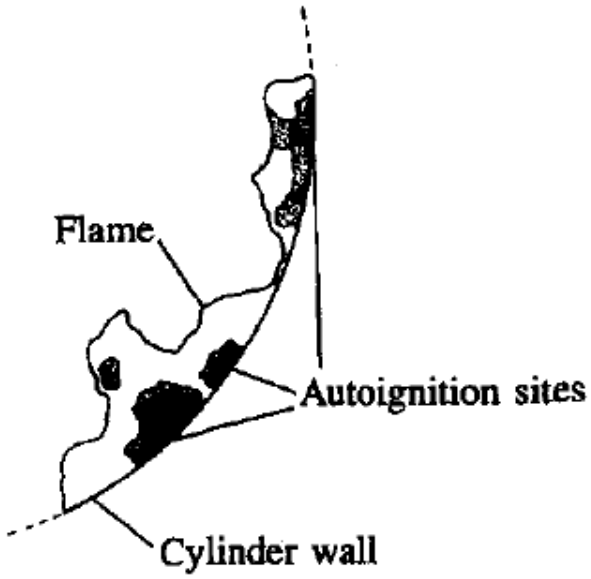

Figure 67: Unburned gas auto-ignition (Figure comes from [1])

Varieties auto-ignition characteristic modeling methods are available, from comprehensive chemical kinetic based simulations [79], to a global single step Arrhenius

function describing all hydrocarbon oxidation reactions [125]. Reduced chemical kinetics descriptions are available [80] as well. Among the methods above, the single step Arrhenius function is recognized as the most practical way of predicting the ignition delay for control purposes due to its simplicity and relatively good physical representation [81]. It is widely studied based on experimental data for auto-ignition prediction in constant volume bombs, steady flow reactors, rapid compression machines and IC engines [82][83]. Phenomena for ignition delay are observed both experimentally, in rapid compression machines (RCM) [84] and in detailed chemical kinetics simulations [85].

A typical commercial automotive gasoline contains approximately seven hundred types of molecules [86]. For highly detailed chemical kinetic modeling ignition characteristics of each individual molecule in the temperature and pressure domain is required. This information is rarely available and time consuming to calculate, so a global reaction that describes all the hydrocarbon oxidation processes in a single-step Arrhenius function is favored in this research. The equation relates the rate of reaction of an auto-ignition product as a function of pressure and temperature, assuming single-step chemical kinetics:

$$\frac{d[x]}{dt} = A'_G[x]p^n \exp(-\frac{B_G}{T}) \tag{48}$$

The ignition delay, in milliseconds, can be expressed as the inverse of the reaction rate of the global single-step mechanism:

$$r_G = A_G p^{-n} \exp(\frac{B_G}{T}) \tag{49}$$

Equation (49) is developed to represent the ignition delay in a RCM with coefficients extracted from experimental data. In a RCM, the pressure is assumed approximately constant until combustion occurs. However, for a spark-ignited engine, the end gas is compressed by the propagating flame and the temperature rises following a polytropic process. Livengood and Wu [125] proposed that the end gas auto-ignition chemistry is cumulative and can be predicted by integrating the reaction rate of the end gas at discretized pressure and temperature time steps until the critical time when the integral value is equal to one, as shown in Figure 68.

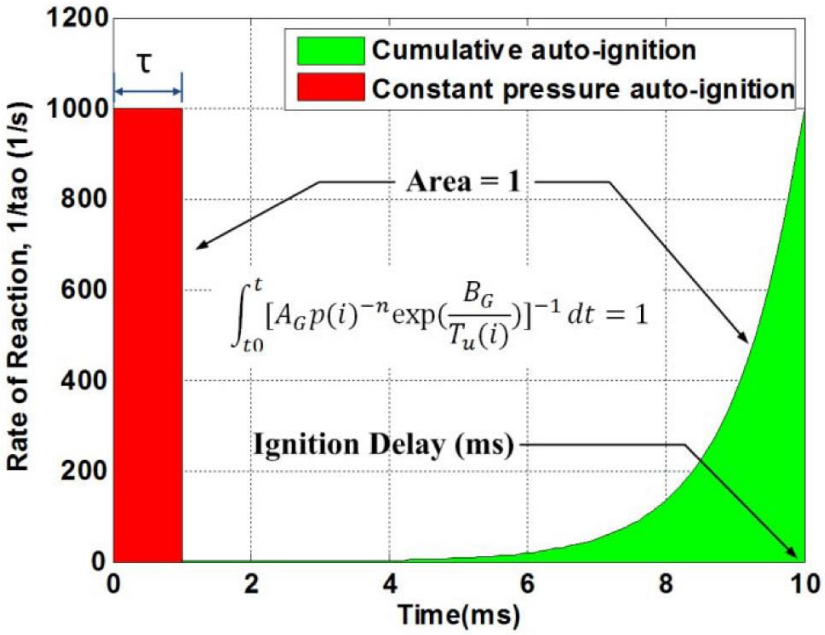

Figure 68: Illustration of the Livengood-Wu Integral for predicting auto-ignition in a changing pressure andtemperature environment.

Several researchers have fit coefficients of the L-W integral by polynomial regression to a chemical kinetic model for ignition delay prediction [86][88][89]. These

techniques are empirical, but have proven capable of adapting to changing octane number. In this project, the calibration constant values are shown in Table 6.

Table 6: Calibration constants in ignition delay model

A_G	n	B_G
$17.68(\frac{ON}{100})^{3.402}$ (ON is fuel octane)	1.7	3800

To validate this global single step knock model, experimentally recorded test data is applied as inputs into the model equations and the following figures show the results.

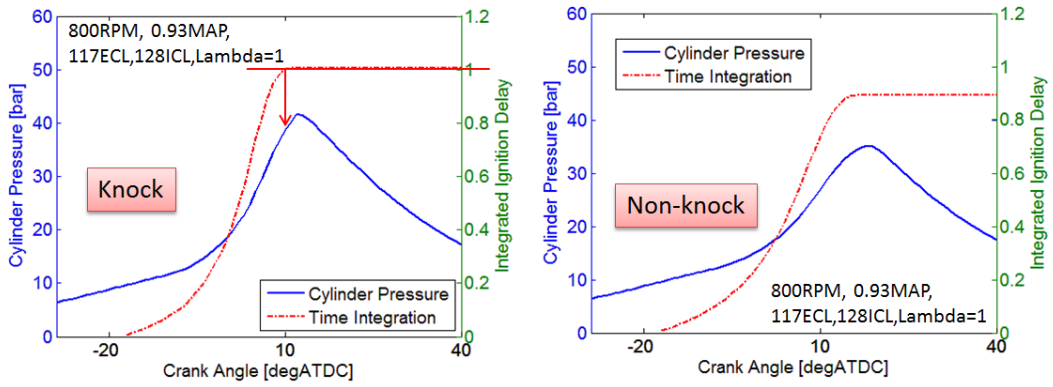

Figure 69: Comparison between knocking and non-knocking cycles under the same engine operation conditions (800RPM, 0.93barMAP, 117ECL, 128ICL, Lambda=1)

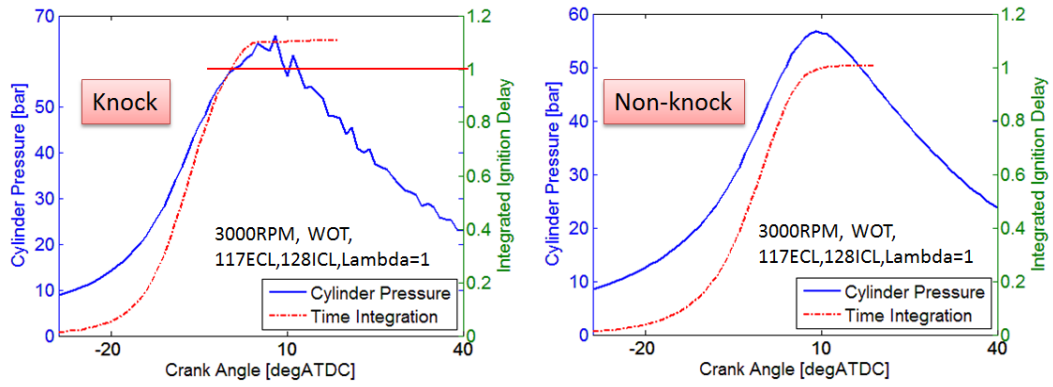

Figure 70: Comparison between knocking and non-knocking cycles under the same engine operation conditions (3000RPM, WOT, 117ECL, 128ICL, Lambda=1)

Figure 69 and Figure 70 show the validation results for the global single step knock prediction model. They respectively present knocking and non-knocking engine cycles under the same engine operation conditions. Figure 69 shows light knocking event, the L-W integral reaches 1 when the knock happens (even this minor knock event). Figure 70 shows heavy knock event and the knock model accurately capture the knock event as well. For both engine operation conditions, when knock does not happen, the integral is smaller then 1, which precisely give a knock prediction result.

The knock model is implemented into ETAS ES910 rapid prototype ECU to calculate knock integral real-time and the dyno cell test data is recorded. The knock model real-time results will be described in detail in Chapter 7.2 Real-Time Engine Test Results.

5.2 Combustion Variation Prediction Model

High Combustion variation of Internal Combustion (IC) engines induces many mechanical control and design issues. These variations could shift the combustion phasing and increase the chance of the engine to run outside the target operation range. Covariance of Indicated Mean Effective Pressure (IMEP) is commonly used to indicate the level of combustion variation for IC engine. For SI engine, the risk of knock and misfire is the most critical issues related to combustion variation. Most knock control considers this effect and further retard the spark timing to reduce the chance of knock 91. This also leads to lower thermal efficiency of the engine. A high-fidelity prediction of combustion variation can reduce the conservativeness of spark retard during the knock limited operation conditions. Un-intentional retarded combustion phasing could cause

reduction of torque output, risk of misfire and NO_x emission due to high combustion temperature. Moreover the IMEP variation leads to engine speed fluctuation and powertrain vibrations, which could worsen the vehicle NVH (Noise, Vibration and Harshness) performance and lead to engaging issues of modern transmissions with interlocking mechanisms like dog clutches. In summary, combustion variation is usually not desirable for IC engine operations. However, for the turbulent combustion, the combustion variation is unavoidable. Furthermore, it is inevitable for the engine on vehicles to run at conditions with high combustion variations. For instance during shift event, the spark timing changes significantly to track the fast transitions of torque demand, often resulting in high COV of IMEP. Under these engine operation conditions, the control engineers have to weigh between combustion variation and other performance demands. An accurate online estimation of COV of IMEP can be beneficial to this process. A calibrated map of COV of IMEP versus some engine operation conditions can be an option for engine with few actuators. However, the map based calibration becomes cumbersome when the freedom of IC engines increases and the physics based model of combustion variation becomes favorable due to less calibration effort.

Most previous literatures studying the cause of IMEP variation is founded upon the theories of turbulent combustion stability [92][105]. It can be summarized that the cyclic combustion variation is caused by charge composition variation [94][95] and in cylinder flow variation [97]. Some of the literatures concluded that the stochastic properties of the flame kernel development stage affect the rest of the combustion propagation significantly so that it should be the primary consideration for investigation

of COV of IMEP [101]. The reasoning and logic of these approaches are without questions. However, most of these works explain the cause of COV of IMEP at concept level without giving a practical accurate prediction of COV of IMEP. This situation is a result of modeling COV of IMEP, a stochastic value, with other stochastic variables like the variation of some properties. These measurements are only available for experiment environment where the engine can be controlled to run at steady states for multiple cycles, which is not a common situation for actual driving scenarios. There is literature relating the combustion variations to deterministic properties. High Speed Particle Image Velocimetry (HSPIV) was applied by *Long et al.* [104] to capture real time turbulence levels in cylinder. It was concluded that high frequency turbulent motion contributed to the COV (Covariance of IMEP). *Abdi Aghdam et al.* [105] incorporated this concept to his quasi-dimensional combustion model by adding a cyclic random factor *K* to the calculation of turbulence intensity. The simulation results showed cylinder pressure variations close to experimental observation. Without further discussion that correlated the random factor *K* to measureable engine parameters, the practicality of this model was undermined. Furthermore, relating the IMEP variation to only one contributing factor, turbulence intensity, is considered an over-simplification of the issue. *Galloni* [103] proposed to estimate the COV of IMEP with laminar flame speed (S_L), turbulence intensity (u') and magnitude of the mean flow velocity (U) in the spark region. These three variables were calculated at the time of spark. CFD methods were applied to estimate U making this method unsuitable for online application.

Regime diagrams were created to categorize flame propagation of premixed turbulent combustion [106]. These diagrams showed different time scale combination of turbulent motion and flame propagation can significantly affect the combustion stability. These diagrams are separated into several zones with different flame regimes. Zones with continuous laminar flame sheet tend to have stable combustion, while others indicates possible combustion instability (flame quench). *Russ et al.* [109] relates the COV of IMEP to the Leeds diagram inputs, u'/S_L and L/δ_L (turbulent integral length scale/laminar flame thickness). Results of this work indicated that COV of IMEP is high when the engine is operated close to the "flame quench" zone. Another important conclusion can be drawn from this research is that the beginning of combustion is the most unstable phase of the entire reaction process. Once the flame kernel is developed inside the cylinder, the combustion is going to become more stable because of the formulation of continuous laminar flame sheet. *Dai et al.* [110] stated similar conclusion with slightly different explanations. Even though combustion stability is the fundamental reason of IMEP variation, treating COV of IMEP as an extension topic of combustion stability did not yield reasonably good prediction of its exact value under various engine operation conditions.

Although COV of IMEP is used as an indicator of combustion variation, these two concepts are not equivalent to each other. It is not reasonable to use models and variables directly from studies of turbulent combustion variation to predict COV of IMEP without considering how combustion affects cylinder pressure. The exact quantification of combustion variation is ambiguous to some extent since combustion can be considered

as a series of heat release event in crank angle or time domain. For each event, the released heat is then transformed into cylinder pressure corresponding to the current in-cylinder air states (e.g. volume and pressure). This synchronization between piston motion and combustion process significantly affects how sensitive the COV of IMEP is to the combustion variation. *Lee et al.* [111] suggested that the COV of IMEP has strong correlation with combustion duration (CA10 to CA90). By regression analysis, this research work identified clear ascending tendency of COV of IMEP as the duration between CA10 and CA90 increases. The significant impact of combustion phasing on COV of IMEP is discussed in this document.

Many methods were proposed to capture the combustion variation by adding randomness to the combustion model [112]. These models were designed to regenerate the stochastic behavior of the IC engines through Monte Carlo simulations instead of estimate the COV of IMEP directly. Few literatures demonstrated models with COV of IMEP as output. *Young* [92] applied linear regression methods to predict COV of IMEP. A polynomial model was proposed by [115]. By introducing combustion phasing as inputs, the model has decent accuracy. However, the reasoning and physics for selecting the model inputs were weakly discussed. *Galloni* [103] employed a nonlinear regression model to predict COV of IMEP. Although the accuracy is satisfying for all the test points, validation results shows that the model can capture the tendency of COV change with different engine operation conditions.

Qilun Zhu proposes a prediction model of COV of IMEP combining the combustion phasing information and premixed turbulent combustion stability theory. In this project, this combustion variation prediction model is applied.

A semi-physical "Grey Box" ANN based COV prediction algorithm is shown in Figure 71.

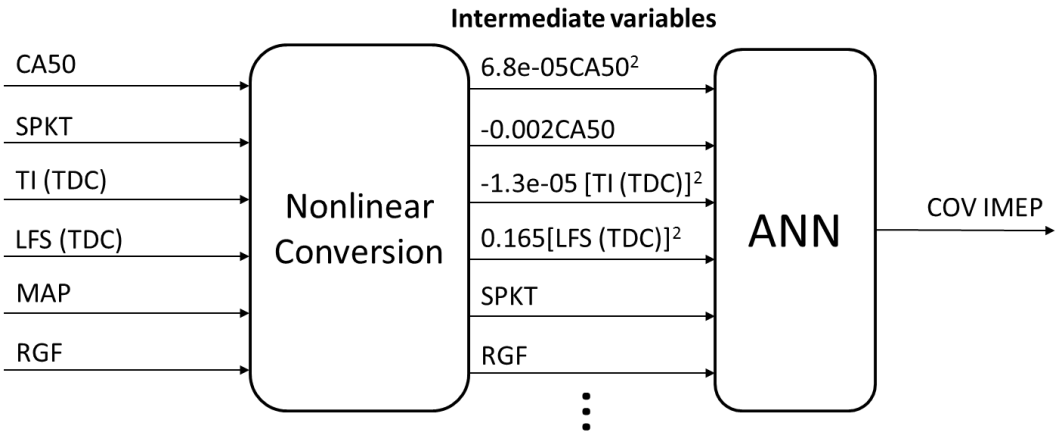

Figure 71: Block diagram of the proposed COV of IMEP model.

The inputs into this COV model are not simple engine operation conditions. Instead, it uses important physics, which could significantly affect combustion stability, as inputs. Then the nonlinear conversion process helps eliminate the nonlinear characteristic of the input physics. The linearized inputs are sent into the COV ANN to predict the engine combustion COV of IMEP.

The important physics are selected based on turbulent flame combustion theory and the Leed's diagram [106]. Artificial Neural Network (ANN) is an efficient "black box" modeling method for systems with nonlinear inter-correlation characteristics. However, the robustness of ANN prediction outside the training region is not guaranteed.

Although it is difficult to find techniques to ensure extrapolation stability with strict mathematical proof, it has been acknowledged that decreasing number of hidden layers and neurons can improve the stability of ANN outside the training region. The inevitable cost of reducing neural network size is loss of accuracy in terms of capturing nonlinear correlations. A simple polynomial regression based nonlinear conversion is applied to the original model inputs, transforming them into intermediate variables. These variables are used as inputs to the ANN, which only has 1 hidden layer and 3 neurons.

The ANN is trained and validated with 248 and 106 data points correspondingly. It can be observed from Figure 72 that the model performs well with data other than the training set.

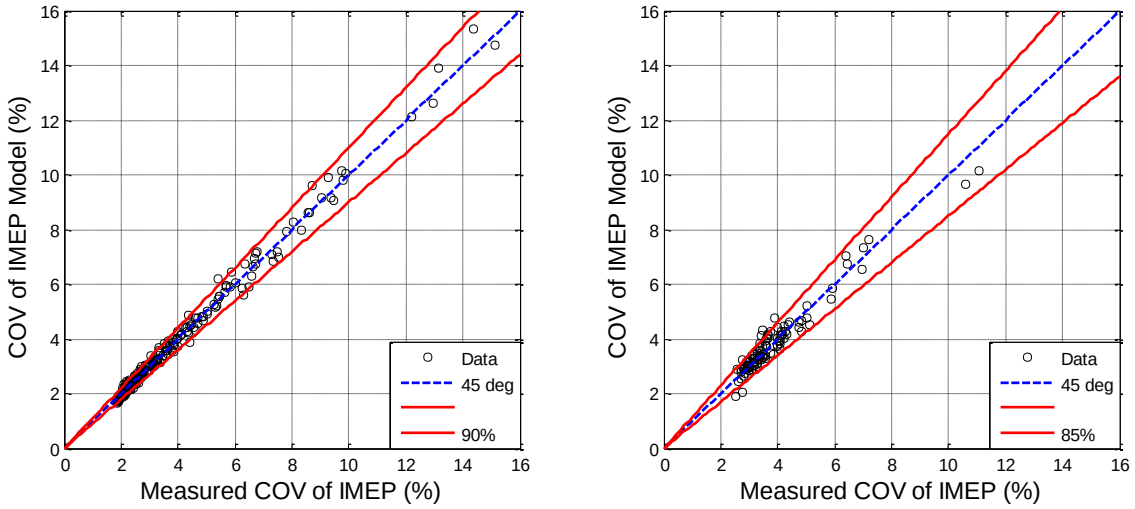

Figure 72: Comparison between measured COV of IMEP and ANN. Left is training data and right is validation with different data set.

This model was implemented with prototype ECU and test under FTP driving cycle, during which the engine operates frequently outside the training region. Figure 72 shows that the predicted COV of IMEP from the model is within reasonable range.

Figure 73 plots the contour of the predicted COV of IMEP on top of CA50 and MAP. It shows that the high COV of IMEP happens at low MAP and late combustion situation.

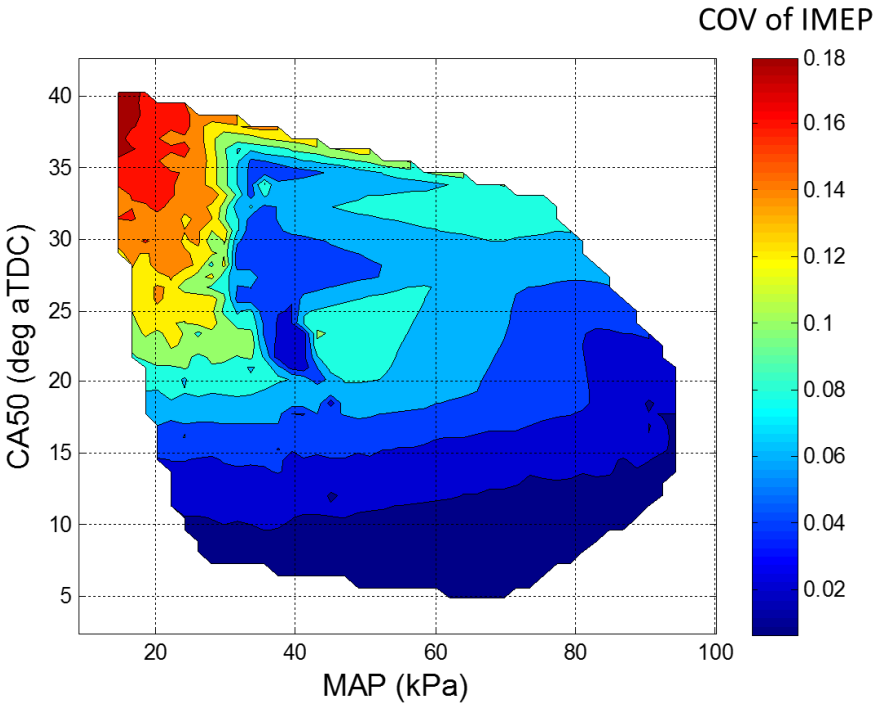

Figure 73: Contour plot of COV of IMEP vs. CA50 and MAP.

CHAPTER SIX

SPARK SELECTION

In this project, the combustion phasing control needs to be realized by determining the spark timing that achieves the desired combustion phasing. Although the main task in this project focuses on physical model based combustion phasing prediction, the real-time on-engine control is actually the spark timing determination process. Based on combustion phasing calculation results and target combustion phasing requirement, ideal spark timing needs to be selected and sent to ECU to realize phasing control.

6.1 Target Combustion Phasing

To select the ideal spark timing the target combustion phasing is required. According to specific engine operation conditions and special requirements (fuel economy improvement, emission reduction, catalyst protection, transmission gear shift management and etc.), desired CA50 values can be pre-stored in a look up table or determined by a model for real-time application. Because the main objective for this project is not to select ideal CA50 values (a calibration task), the desired CA50 is randomly selected within a reasonable SI engine operational range.

6.2 Spark Selection Algorithm

Once the target combustion phasing (i.e. CA50) is obtained, the next step is to select the ideal spark timing to achieve that CA50 location. In this project, physics based models enable the prediction of detailed combustion processes in-cylinder for each combustion cycle. However, the combustion model and other sub-models are forward

calculations, which means the spark timing is required to calculate the combustion process. Although theoretically it is possible to invert all models to back calculate spark timing from target combustion phasing, it would lead to a lot of differential equations and take extensive computational effort to solve. Therefore, it is unsuitable to apply the backward spark timing calculation algorithm to real-time engine combustion control. Consequently, an iterative forward spark timing selection method is needed.

The algorithm first carries out a sensitivity analysis to determine the relationship between spark timing and combustion phasing. The following figures show the comparison between spark timing and CA50. Figure 74 shows the spark timings and their corresponding CA50 values at 1500 RPM. The spark sweep is from 10 to 60 degree BTDC and their CA50 locates between -15 and 30 degree ATDC. The blue line in the plot shows a quadratic fitted line and the relationship between spark timing and CA50. Similar trends can be observed for different engine operation conditions, and additional example is shown in Figure 75.

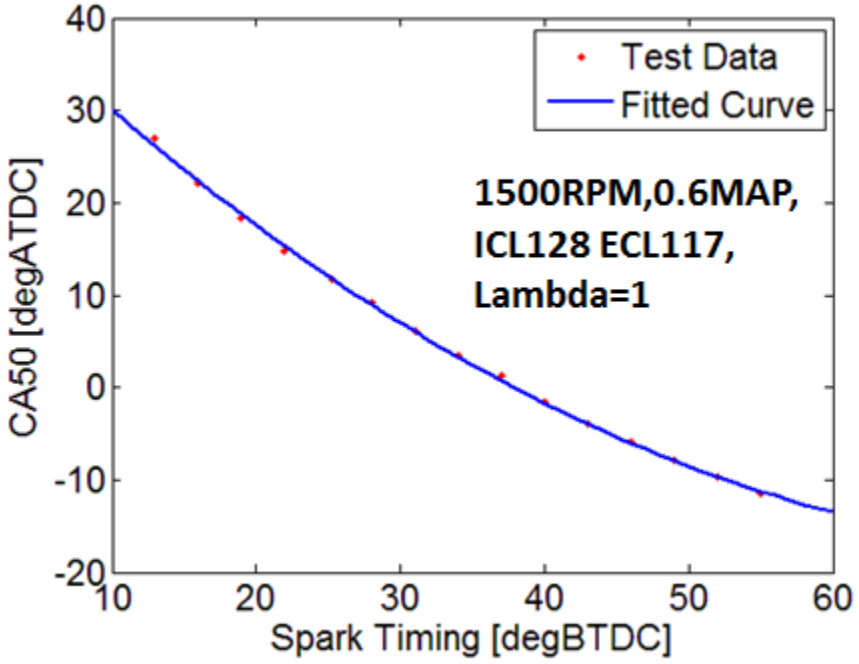

Figure 74: Spark timing vs. CA50 (1500RPM, 0.6bar MAP, ICL128, ECL117, Lambda=1)

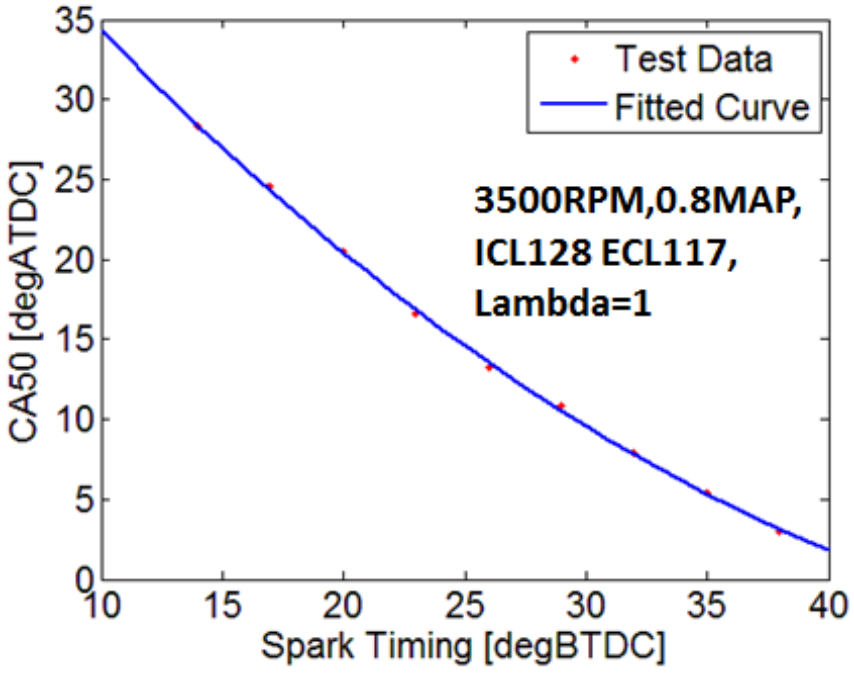

Figure 75: Spark timing vs. CA50 (3500RPM, 0.8 bar MAP, ICL128, ECL117, Lambda=1)

Once the spark timing and combustion phasing relationship is determined, the spark timing selection algorithm is derived from that. The quadratic curve fitting algorithm is firstly considered. Three different spark timings are given and sent into combustion phasing prediction model to calculated CA50 values. Then, the three spark timings and corresponding calculated CA50 values are set to be the input and output. The quadratic curve fitting uses these values to fit a 2^{nd} order equation. Finally, the ideal spark timing is calculated from this fitted equation with the desired CA50 as the input. However, it is observed that the fitting result is heavily affected by the accuracy of the combustion phasing prediction. The quadratic fitting result can drift a lot with minor inaccuracy from CA50 prediction values and this situation makes this quadratic fitting based spark selection algorithm unsuitable for most operating conditions.

To replace the quadratic fitting based spark selection, a two iteration direct-search spark selection algorithm is proposed. In Figure 74 and Figure 75, it can be observed that while the relative more precise relationship between spark timing and CA50 is second order that the second order term of the fitted curve is very small. This means the relationship between spark timing and CA50 is quite linear, especially near the MBT location. Then, the linear relationship for CA50 and spark timing is assumed. Based on this assumption, a direct-search spark selection algorithm is developed. Figure 76 shows the block diagram of this algorithm. Firstly, an initial guess spark timing is sent into the combustion phasing prediction model. In this project, the initial spark timing is set to 30 degree BTDC because it is a reasonable spark timing value for most engine operation conditions. Next, the calculated CA50 value is compared with target CA50 and the CA50

difference is used as feedback. This CA50 error is directly added (based on the linear relationship assumption, gain set to be 1) to the initial spark timing value (30 degree BTDC) and the second spark timing value is generated. Then, the second spark timing value is sent to the combustion phasing model and similarly the predicted CA50 is used to get the new CA50 error. The new CA50 error and second spark timing value together can generate the final spark timing. For this direct search spark selection the combustion phasing prediction model is only operated twice before obtaining the target spark timing.

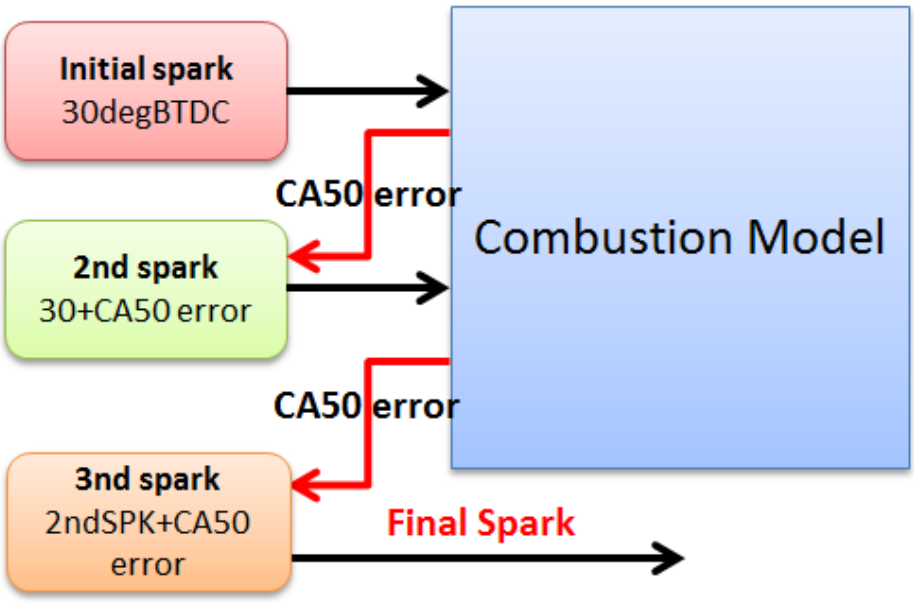

Figure 76: Block diagram of the spark selection algorithm (without engine operational limitations)

Figure 77 shows an example of spark selection algorithm validation results. The engine test data set is compiled with 300 steady-state operating conditions. The constant result is averaged value of 500 consecutive engine cycles under a specific constant engine operation. Different color markers show different validation results with different target

CA50 values. It can be observed. For most CA50 targets, the selected spark could give very accurate CA50 values, within 1 degree error. But for further retarded combustion phasing (here target CA50 is 30 degATDC), the CA50 error is relatively larger. This is caused by the increasing nonlinear characteristic of the CA50 and spark timing relationship for retarded combustion phasing (can be observed in Figure 74 and Figure 75).

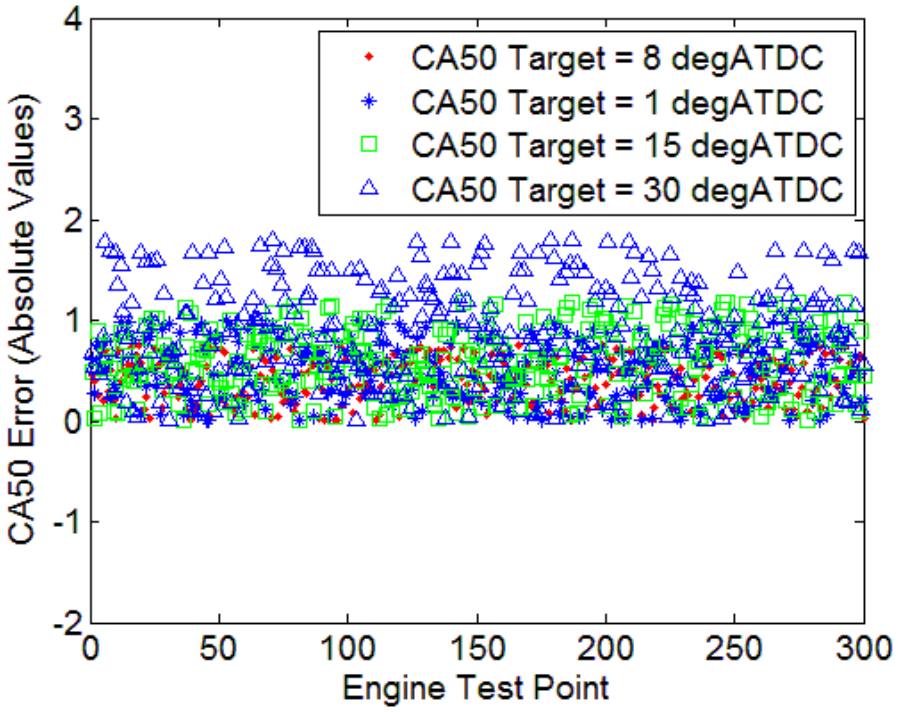

Figure 77: Validation results for direct searching spark selection algorithm

CHAPTER SEVEN

PHYSICS BASED MODEL IMPLEMENTATION IN ECU AND REAL-TIME ENGINE TEST RESULTS

7.1 System Implementation in Rapid Prototype ECU

In this research, an ETAS Rapid Prototype ECU ES910 is used to test for rapid model prototyping on engine real-time combustion phasing control [116]. Figure 78 below shows the real-time engine control implementation process. In this project, all the models are built in Simulink first. The real-time workshop in Simulink could convert the Simulink model into executable code and the code file is sent into INTECRIO. The ETAS INTECRIO is applied to link the coded Simulink model and the control or measurement signals from engine sensors or engine control/calibration windows. Then INTECRIO complies all elements and generate executable file into ES910 (the rapid prototype ECU) to realize engine control. The software INCA is set up with a graphical user interface to communicate with the ES910 to send control signals and read/record engine test measurement data. The ETAS ES910 communicates with ETK (a programmable hardware) in ECU and realizes the engine control. In this project, the combustion phasing control/prediction system models are implemented into ES910.

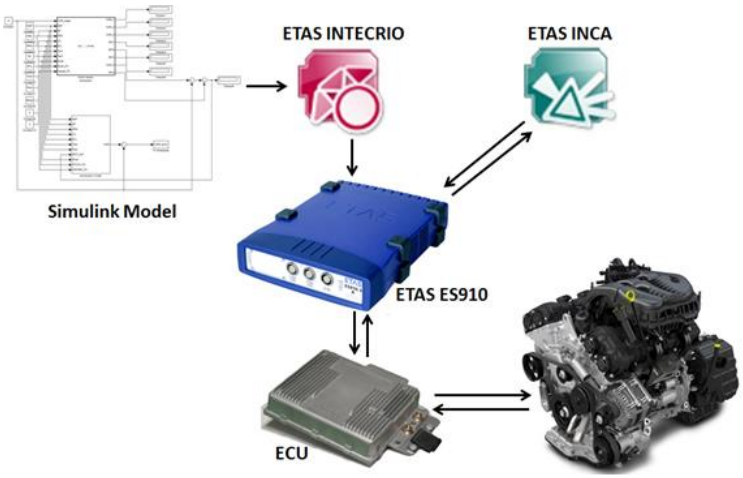

Figure 78: Real-time engine control implementation process structure

7.2 Real-Time Engine Test Results

All the physics based models are developed in Simulink first and then compiled into ETAS ES910 by INTECRIO for real-time engine test application. In this section, the first part shows real-time validation results for the RGM, knock and COV models separately. Then in the second part, combustion phasing prediction and real-time control results are described.

7.2.1 Residual Gas Mass Prediction Model Real-Time Validation Result

The following figures show real time RGF prediction results from the ES910 under transient engine operating conditions. In Figure 79, it shows the engine operating conditions (manifold pressure and engine speed) and the right plot.

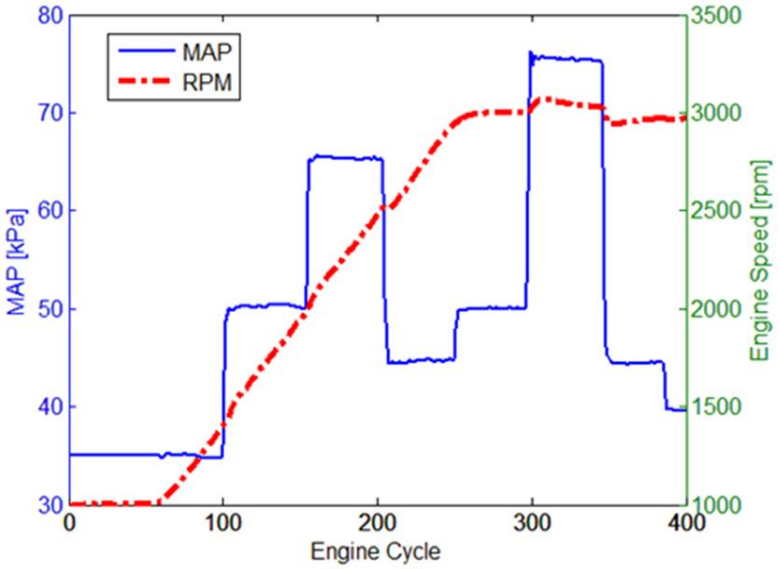

Figure 79: Engine operation conditions for RGF model validation (test 1)

Figure 80 shows the comparison between RGF from GCA (reference, off-line calculation) and the real-time RGF from the model. During this transient condition, the RGF model accurately predicts the reference values (calculated off-line with GCA) with a 0.84% RGF RMSE and a maximum of 1.9 % RGF error (with worst case relative estimation error of 24%). Similarly, Figure 81 and Figure 82 show engine operating conditions where engine speed was decreased from 3500RPM to 1000RPM at varying manifold pressures. The RGF comparison results show good real time residual gas fraction predictions with a RMSE of 0.71% RGF and a maximum error of 2.0% RGF (worst case relative estimation error of 13.5%). Figure 83 and Figure 84 present engine operating conditions with transient intake and exhaust camshaft phasings. Figure 83 shows the valve phaser positions while the engine speed and intake manifold pressure are held constant. The results in Figure 84 shows the RGF model predictions of residual gas mass/fraction for different camshaft phasings under transient engine operation. The

RMSE for 550 transient engine cycles is 0.83 % RGF with a maximum error of 2.3% RGF (worst case relative estimation error of 9.8%).

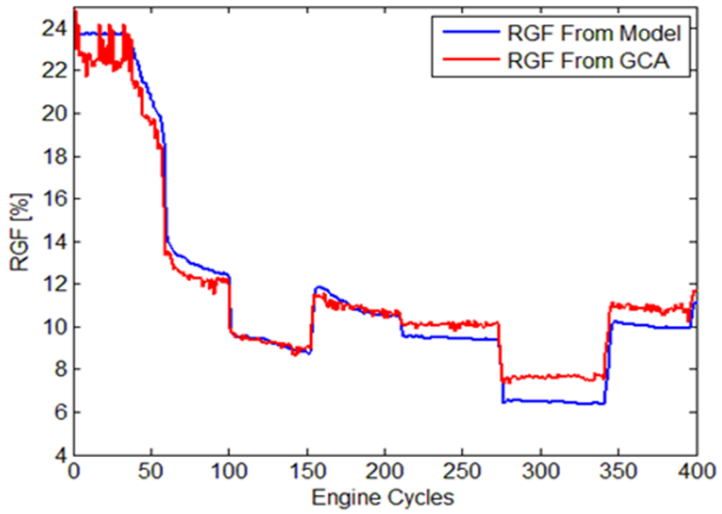

Figure 80: Real time residual gas fraction prediction validation results (1000RPM-3000RPM, fixed camshaft position)

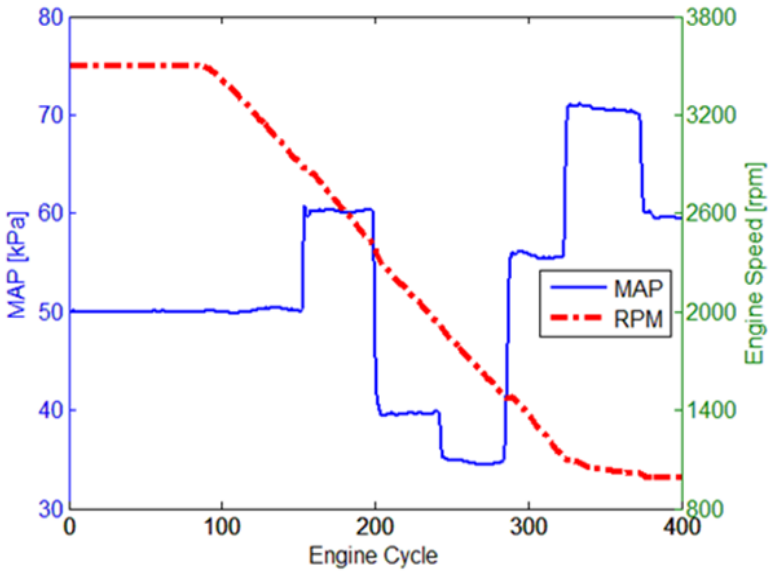

Figure 81: Engine operation conditions for RGF model validation (test 2)

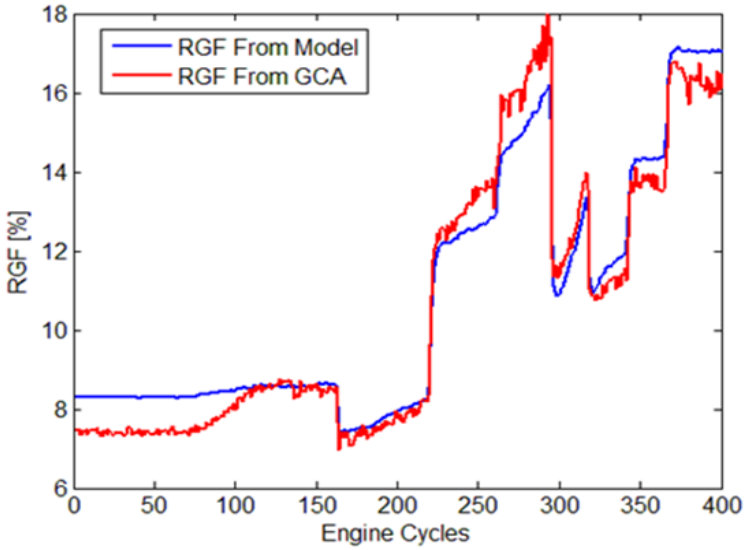

Figure 82: Real time residual gas fraction prediction validation results (3500RPM-1000RPM, fixed camshaft position.

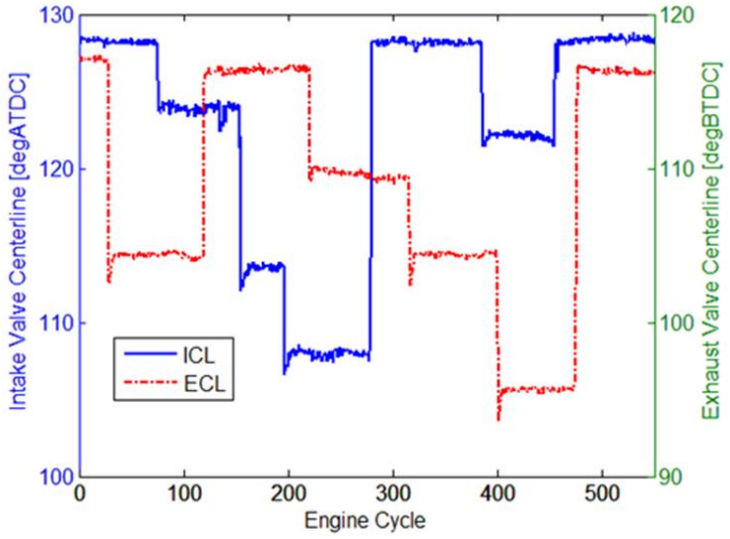

Figure 83: Engine operation conditions for RGF model validation (test 3)

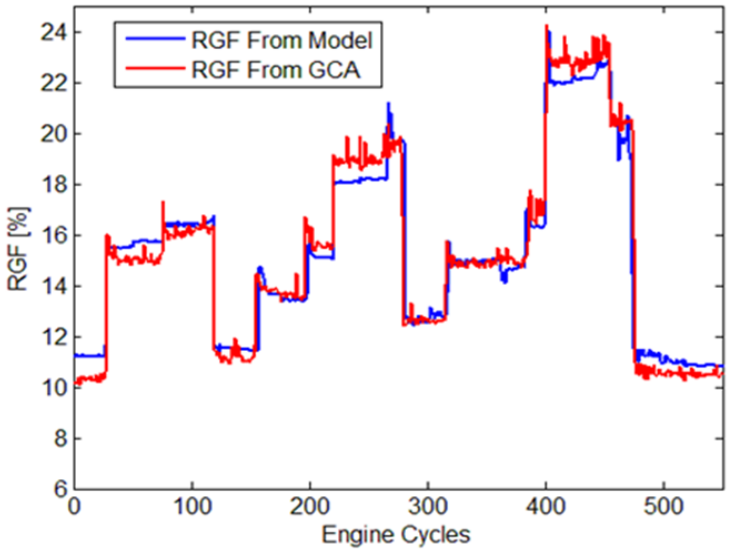

Figure 84: Real time residual gas fraction prediction validation results for transient intake and exhaust camshaft phasings (engine speed is 2000RPM and MAP is 50kPa).

7.2.2 Knock Model Real-Time Validation Result

The global single step knock prediction model is implemented into ES910 for real-time test. The following figures describe the engine operation conditions during the real-time engine test and the knock intensity values are compared.

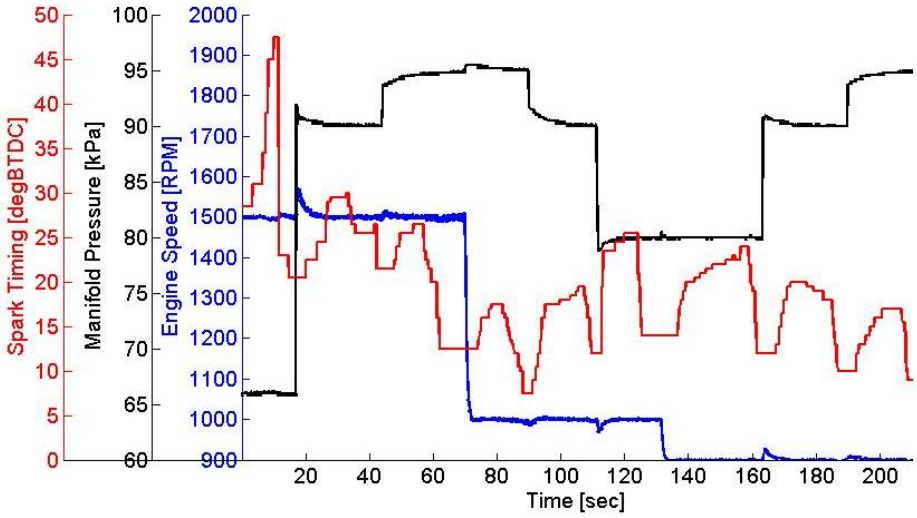

Figure 85: Engine operation conditions of knock model validation data set

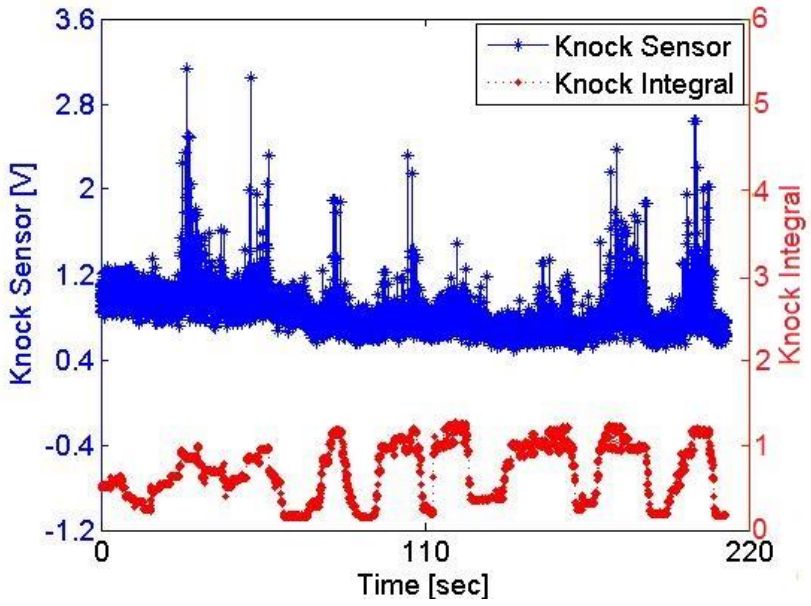

Figure 86: Knock sensor voltage and model calculated knock integral comparison

Figure 85 shows the engine operating conditions (i.e. engine speed, manifold pressure and spark timing) during the knock model validation process and Figure 86 shows the comparison between knock sensor readings and model predicted knock

integral. In Figure 86 blue stars show the sensor voltage and read dots are knock integral. It can be observed when the knock sensor values reach peaks (means engine is knocking), the knock integral also reaches its peak value. This result validates the accuracy of the knock prediction model and the model could very precisely capture engine knock events.

7.2.3 Combustion Variation Prediction Model Real-Time Validation Result

Figure 87 presents model predicted COV values, engine spark timing and engine speed and manifold pressure during the transient engine test (part of FTP driving cycle).

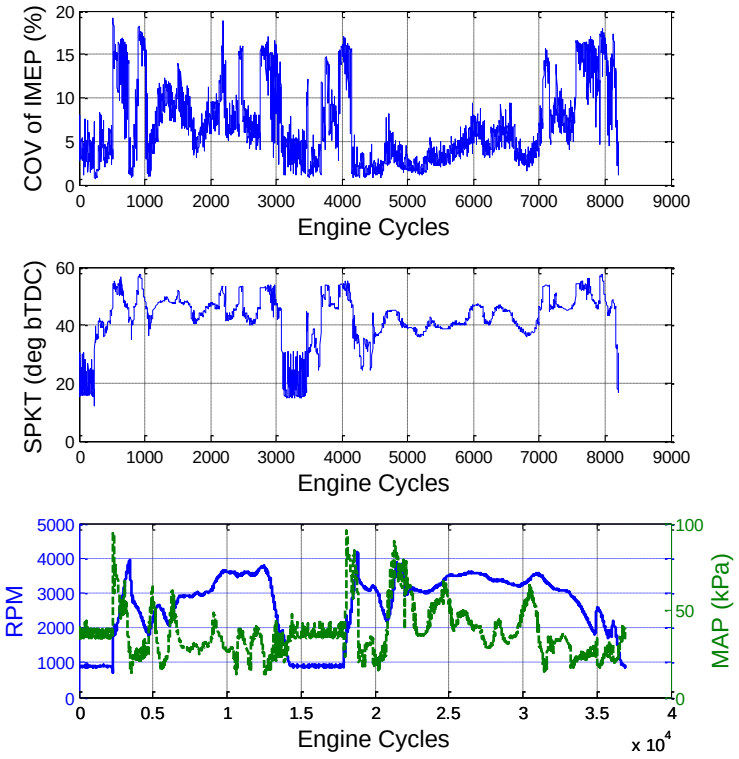

Figure 87: Real-time validation results of COV model under FTP driving cycle test

The result shows the COV model could accurately predict reasonable COV of IMEP values for transient engine operations. When engine load is very low (below 30

kPa), the combustion becomes very unstable and the combustion variation increases where the model gives relatively high COV values.

7.3 Physical Models Based Combustion Phasing Prediction and Control System Real-Time Engine Test Validation Results

The physics-based combustion phasing prediction and control system models are implemented into rapid prototype ECU ES910 to realize real-time engine tests. In this project, several engine tests are taken to show the validation results of this research.

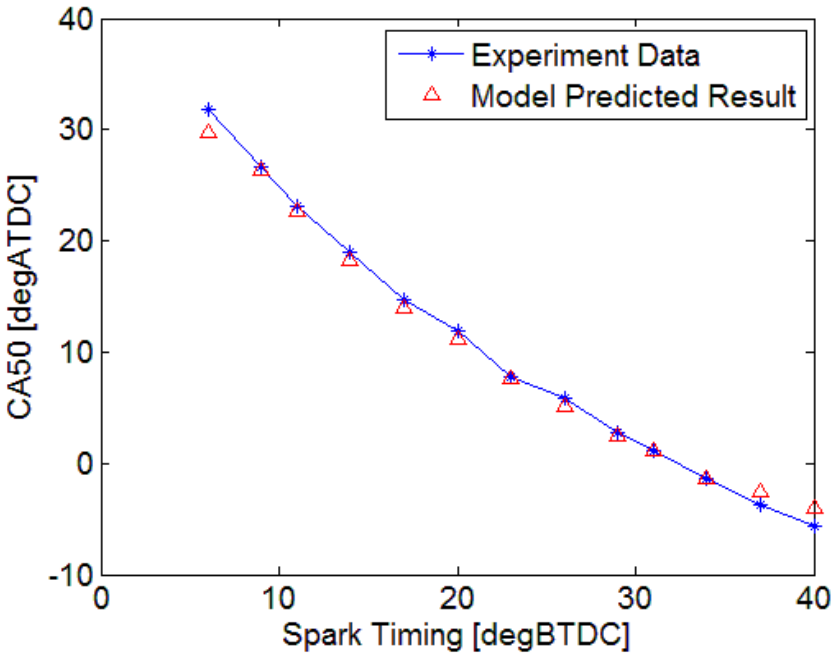

Figure 88: Steady-state engine test results for spark sweep (1200RPM, 0.7bar MAP, 128ICL, 117ECL, Lambda=1)

Spark sweep engine test results are shown in Figure 88. Blue stars show the CA50 values from experiment data and red triangles represents CA50 prediction results. The

CA50 errors are shown in Figure 89. From the results, the combustion phasing control system could very accurately predict CA50 values under different engine operations.

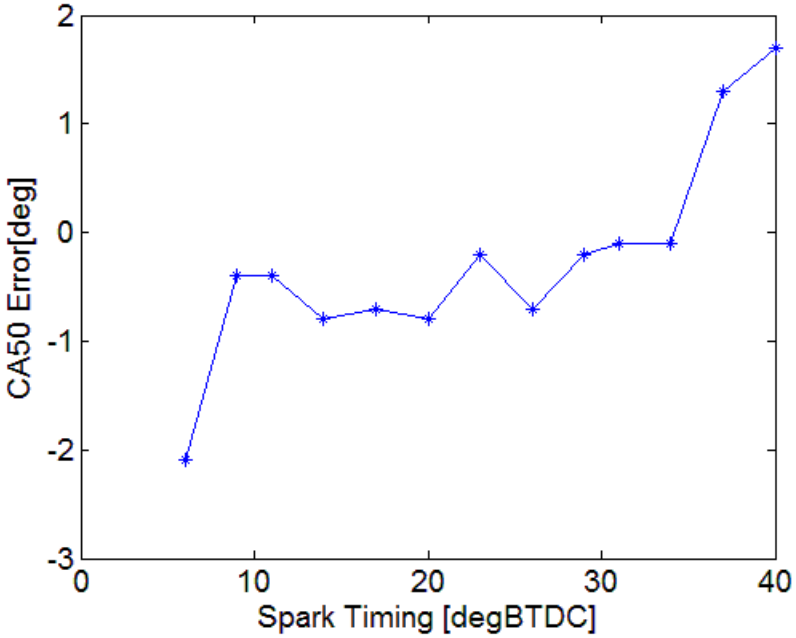

Figure 89: CA50 errors for spark sweep constant test

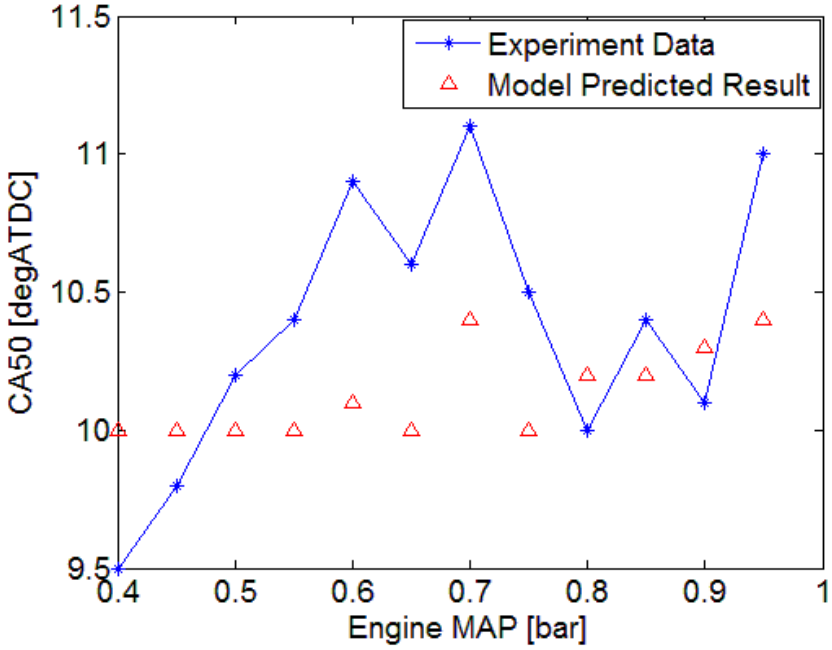

Figure 90: Engine steady-state operation test results for engine load sweep (1500RPM, CA50=10degATDC, 128ICL, 117ECL, Lambda=1)

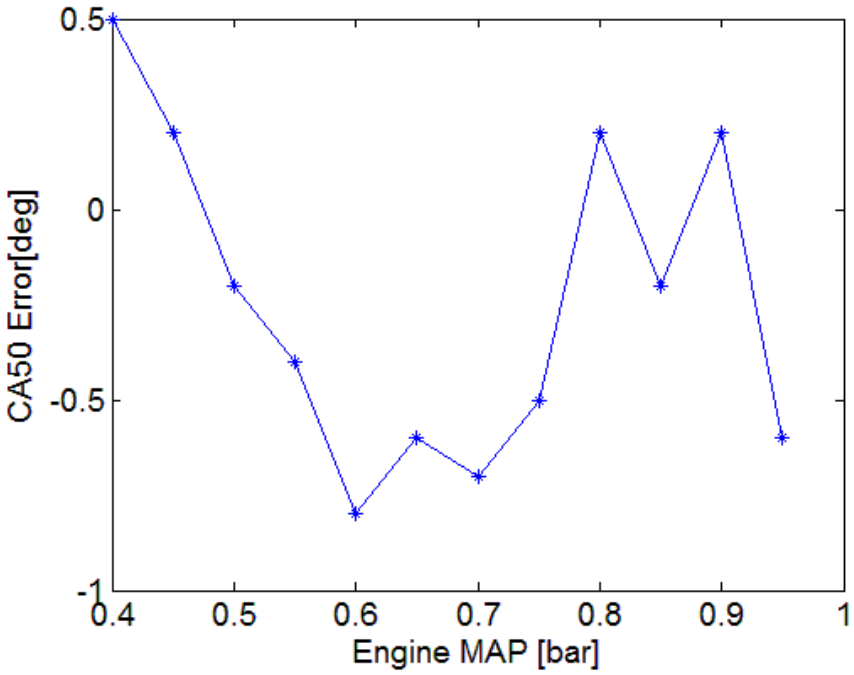

Figure 91: CA50 error for load sweep

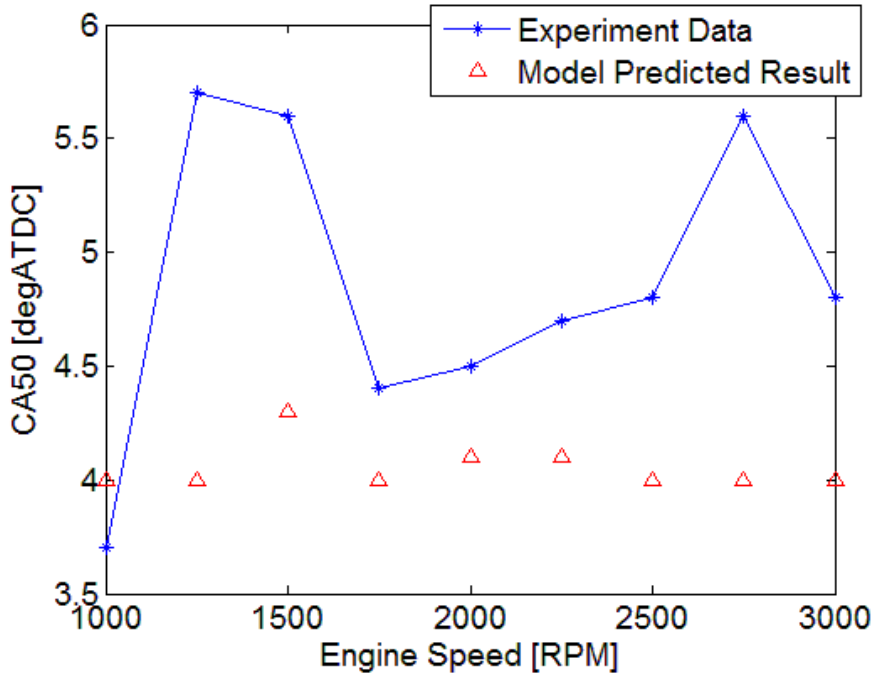

Figure 92: Engine steady-state operation test results for engine speed sweep (0.5 bar MAP. CA50=4, 128ICL, 117ICL, Lambda=1)

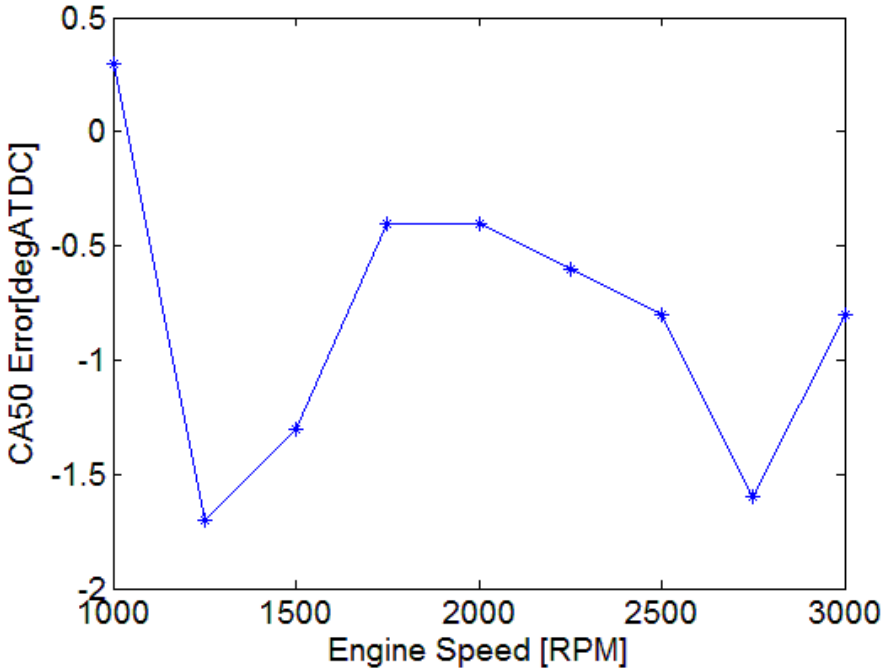

Figure 93: CA50 error for engine speed sweep

Similarly, the engine constant operation test results for engine load and speed are respectively shown in Figure 90 and Figure 92 and their CA50 errors are plotted in Figure 91 and Figure 93. The data set shows the real-time engine test result under constant engine operation conditions. Table 7 below shows the engine operations.

Table 7: Engine operation conditions for constant real-time engine test

Engine Speed	Manifold Pressure	Intake Valve Timing	Exhaust Valve Timing
1000-3000rpm	0.35-0.95bar	98-128degATDC	87-117degBTDC

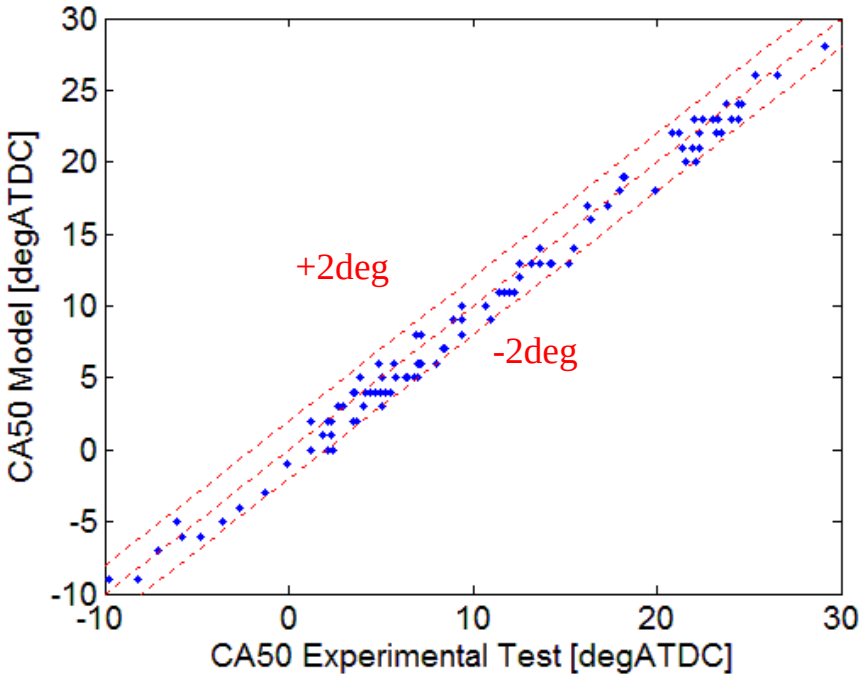

Figure 94: CA50 comparison between experiment data and model prediction results under constant engine operation conditions (102 conditions)

Figure 94 above shows the validation results for the constant engine operation combustion phasing prediction results. It is the comparison between the experimentally recorded CA50 values (from CPDC) and the CA50 value calculated from combustion

phasing prediction models. The x-axis is the experimentally measured/calculated CA50 and the y-axis is the model predicted CA50. The blue dots represent 102 test point results under steady-state engine operating conditions. The red dash line in the middle is the 0 error line and the other two on its two sides form the +/-2 degree error bands. The results show the physics-based combustion phasing prediction system could very accurately calculate the CA50 values for various engine operations.

In the following part, the transient real-time engine test data will be shown to validate the physical model based combustion phasing prediction and control system accuracy.

In Figure 95, the upper plot shows the engine operation conditions (engine speed and manifold pressure) for the transient engine test data (FTP driving cycle) set and the lower plot shows the corresponding engine spark timing and CA50 comparison results for each engine cycle. The black line represents the CA50 values measured real-time from CPDC and is set as the reference CA50. The red line is the model calculated CA50 values for each engine cycle.

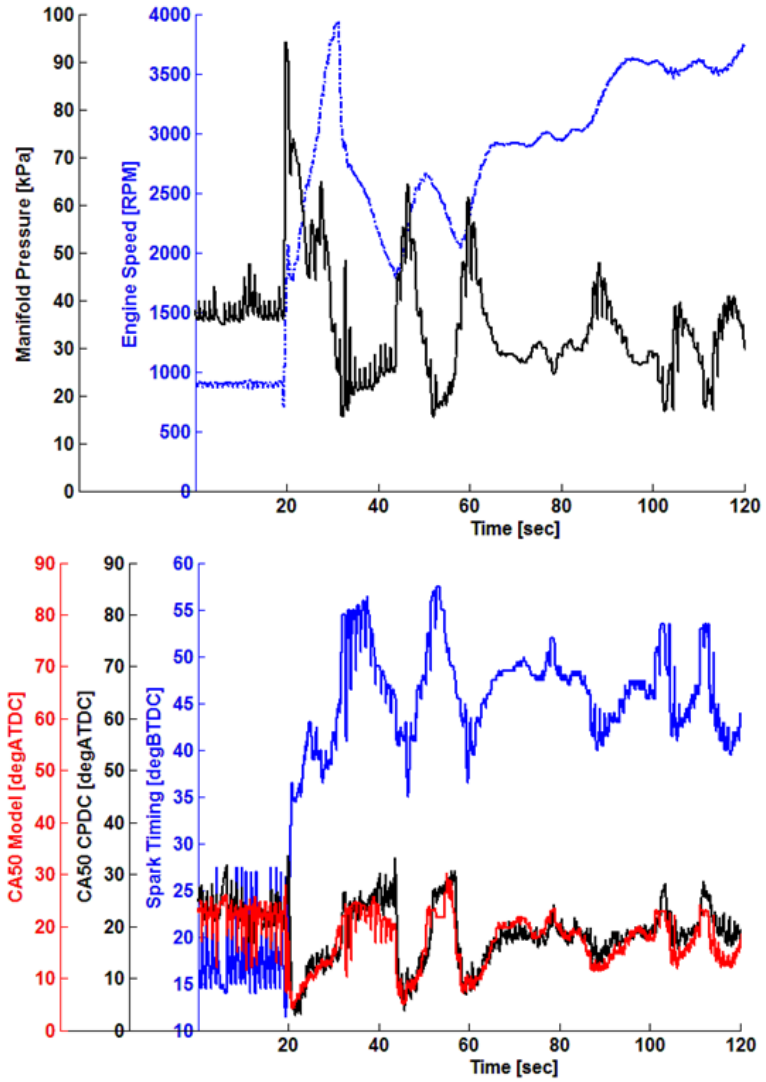

Figure 95: Real-time combustion phasing prediction system validation results (first 120 seconds of FTP driving cycle)

The figure shows the two lines are close which means the combustion prediction system accurately calculates the CA50 value under very transient engine operation conditions. The root-mean-square-error (RMSE) of CA50 for this test data set is 3 crank angle degrees.

In Figure 96, it can be observed that the manifold pressure has many spikes during the FTP driving cycle test. This can be explained by the engine dyno torque control. Because for the driving cycle test, the reference engine operation is the engine speed (calculated from vehicle speed and gear ratio) and engine break torque (calculated from vehicle operations and driving cycle profile). The dyno should control the engine speed and torque to simulate the engine operations during the FTP driving cycle. This could make the engine operation significantly transient. From the results, it can be seen that even under this heavy transient engine operation conditions, the physical model based combustion phasing prediction system accurately calculates the CA50 values.

Figure 96 is the zoom-in results for the first 50 seconds of FTP driving cycle. In the lower plot, the black curve is 5 cycle moving average values from CPDC. Moving average could help smooth the feedback CA50 values, but the response latency during transient can also be observed.

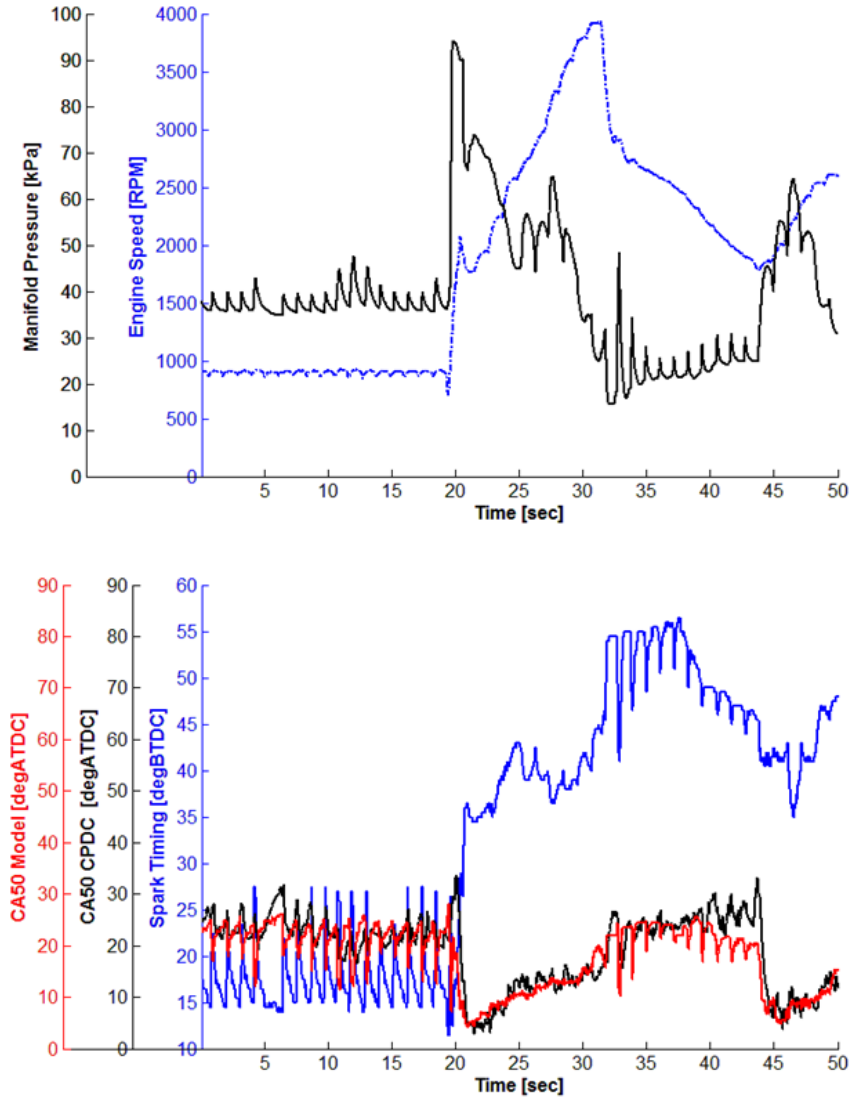

Figure 96: Real-time combustion phasing prediction system validation results (first 50 seconds of FTP driving cycle)

The following figures will show the transient engine test results for the physical model based combustion phasing control validation. Figure 97 shows the engine operation conditions (engine speed, manifold pressure and spark timing) for the transient engine test data set. In this figure, the black line is the manifold pressure, the blue line represents the engine speed and the black line shows the spark timing for each engine

cycle under the transient engine test. It can be seem the engine condition is changing a lot the various engine speed, load induces significant transient engine operation conditions.

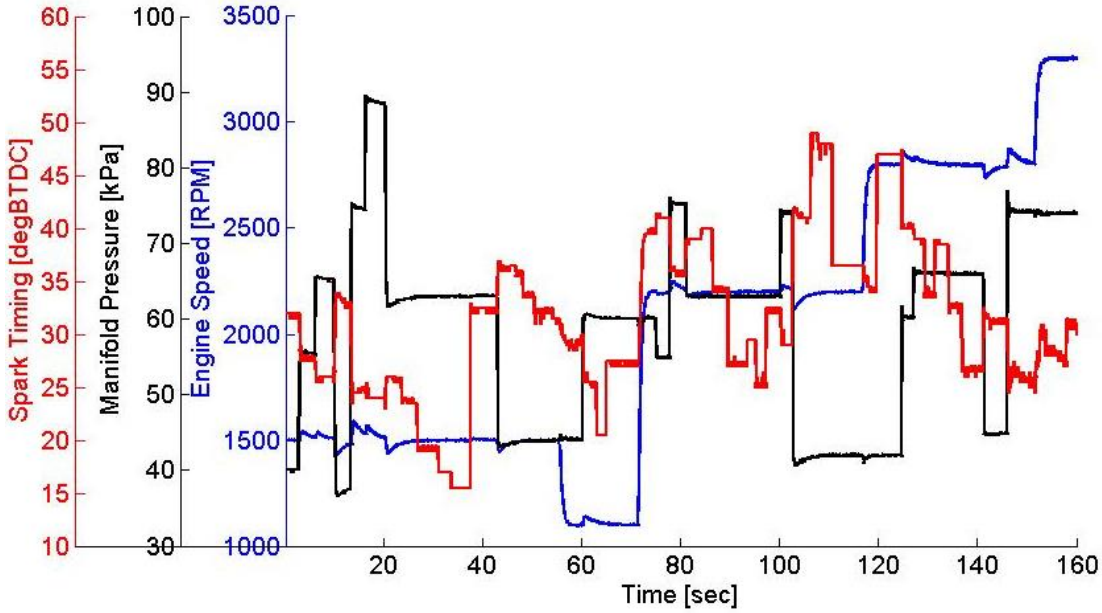

Figure 97: Engine operation conditions for the transient combustion phasing prediction and control validation.

Figure 98 shows the validation results for CA50. In this figure, the blue dots are the experimentally recorded CA50 values from CPDC. The black triangles represent the model predicted CA50 values and the red line shows the target CA50 value. For this transient engine test data set, different from the previous test set, the spark timing is not given as a input. Instead, the spark timing is calculated by the spark selection system. For this transient test, the given input is the target CA50 values. Based on the target CA50 value, the proposed physical model based combustion phasing control system will calculate CA50 value from a given spark timing. Then the spark selection system will run the combustion prediction models twice to generate the desired spark timing and send the spark timing to ECU. In Figure 98, the results show the physical model based combustion

phasing control (spark selection included) can very accurately generate the desired spark timing to achieve the target CA50 values. The RMSE of CA50 from experimentally recorded data and target CA50 values is 2 crank angle degrees. RMSE of CA50 from the model predicted CA50 and the target CA50 is 0.75 crank angle degrees, which means the spark selection algorithm could limit the selected spark timing leaded CA50 error within 1 crank angle degree.

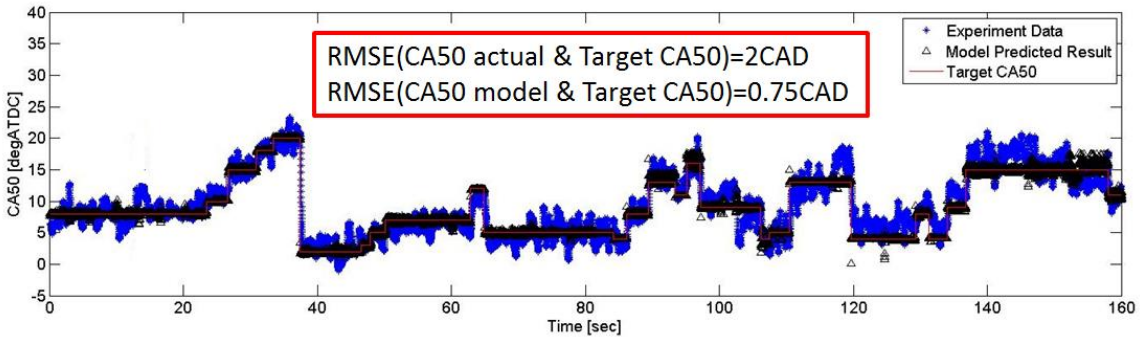

Figure 98: Transient combustion phasing prediction and control validation results.

The following Figures show anther transient engine real-time test results. For this test data set, the main task is to validate the accuracy of the physical models based combustion phasing prediction and control system for variable valve timings.

In Figure 99, it shows engine speed, manifold pressure and selected spark timing for the valve timing validation data set. In the plot, the blue line presents engine speed during the test, the red curve describes the spark timing which is calculated from the physical models based combustion phasing prediction and control system. The black line shows the manifold pressure values. Figure 100 shows the intake and exhaust valve timing situations during the same engine operation conditions shown in Figure 99. The

red circles represent intake valve centerline location and the blue circle shows exhaust valve centerline location.

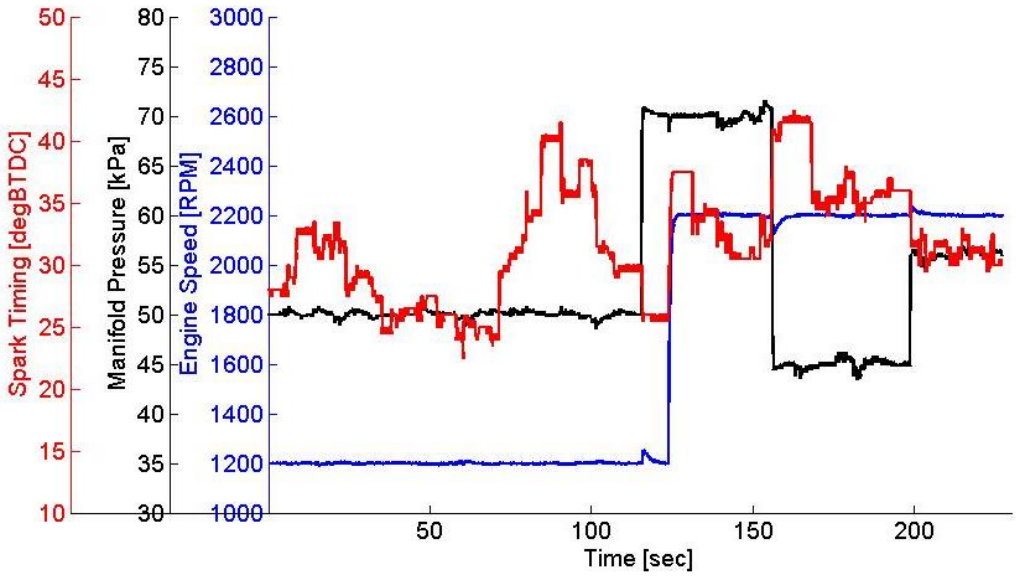

Figure 99: Engine operation conditions

The Figure 101 shown below presents the real-time transient engine test results for the validation of the system combustion phasing control accuracy during transient valve timing test. In this plot, the blue stars show the experimentally recorded CA50 values from CPDC, the black triangle presents the model prediction CA50 values and the red line is the target CA50 values. From the result, it can be observed that under some engine operation conditions (e.g. 20 sec, 55sec and 90 sec), the physical models based combustion phasing control system has relatively large errors (maximum 10 degree). The corresponding engine valve timings under these engine cycles have very large valve overlap, which could lead to high internal residual gas remains in cylinder. The higher

fraction of residual gas could significantly decrease the combustion rate and retard the combustion phasing.

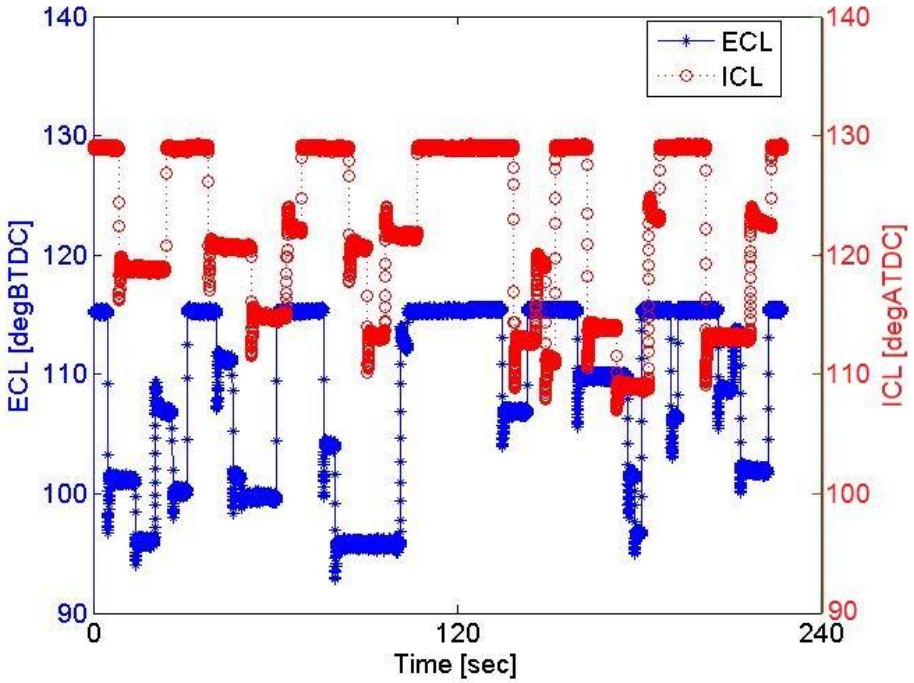

Figure 100: Intake and exhaust valve timing

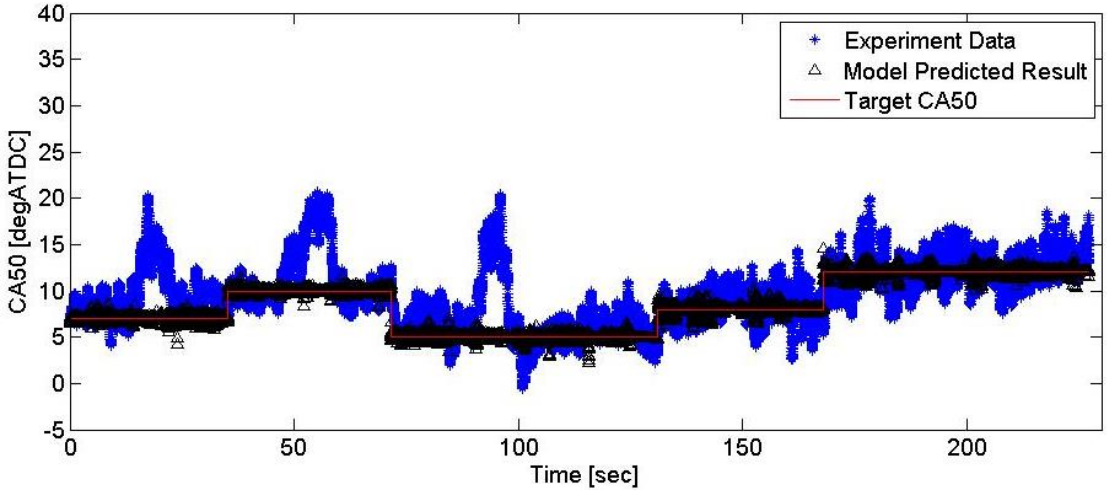

Figure 101: Transient real-time engine test results for CA50 control

The inaccuracy in this test data set could be caused by high residual gas remaining in cylinder and this could retard the combustion phasing, which can be observed from Figure 101. In order to finding out the factor which caused the combustion phasing control inaccuracy, more test data have been recorded.

Figure 102 and Figure 103 shows the test results and both figures present the comparison between predicted residual fraction values and CA50 errors (between model prediction and experiment data). Figure 102 shows the test data under 1000 RPM and Figure 103 shows engine test results under 2000RPM. The blue, red and black lines respectively show the test results under 0.4, 0.6 and 0.8 bar manifold pressure.

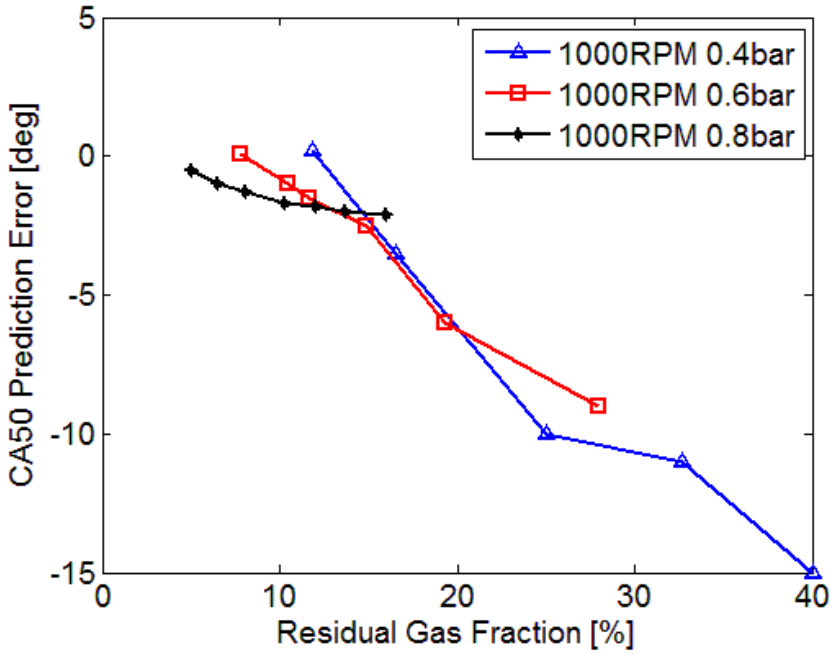

Figure 102: CA50 prediction error from RGF (1000RPM)

It can be observed from Figure 102 and Figure 103 that the CA50 prediction errors are relatively larger for lower engine load and higher residual gas fraction (larger

valve overlap) for both engine speeds. For higher engine load, the residual gas fraction effect on CA50 prediction is relatively smaller which is very reasonable because the combustion rate is higher under higher engine manifold pressure.

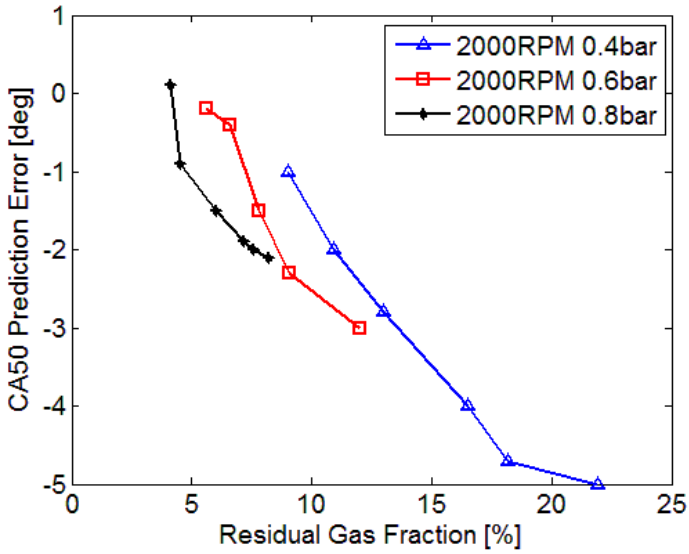

Figure 103: CA50 prediction error from RGF (2000RPM)

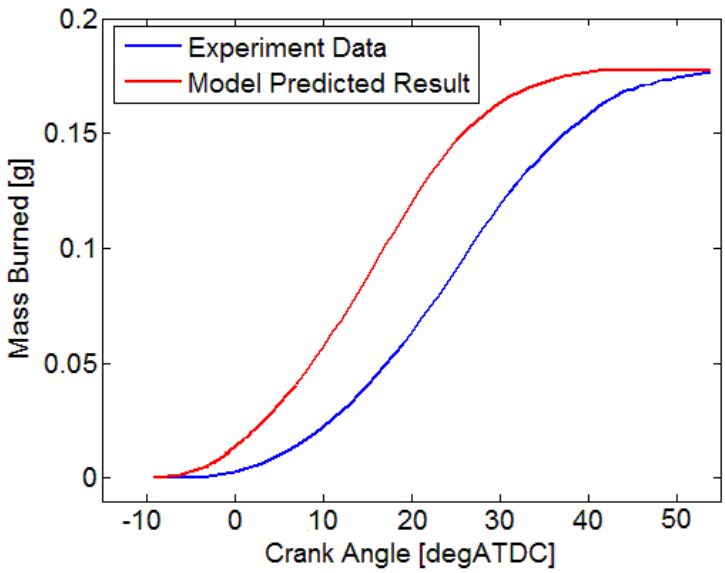

Figure 104: Mass fraction burn (MFB) comparison (1000RPM,0.4bar MAP,87ECL,95ICL,Lambda=1)

Figure 104 shows the mass fraction burn curve comparison between experiment data and model prediction result. The red curve is the result calculated from model and the blue line shows the experimental test data. The result shows that the model has faster combustion rate than real situation and this could be caused by the inaccuracy of the laminar flame speed prediction result (the reason is: MFB curve slopes are similar, but the combustion phasing is too advanced from model prediction result. CHAPTER will describe the laminar flame speed effect on MFB curve in detail). The laminar flame speed can be significantly affected by residual gas fraction (reasons shown in Chapter 3.2.2 Laminar Flame Speed Prediction Model). The error could be the inaccuracy of the RGF prediction result or the calibrated constant for RGF term in laminar flame speed model. The combustion phasing prediction inaccuracy could also come from flame kernel development duration prediction result, which is strongly affected by RGF as well. The discussion and research in this topic can be the future work to improve the combustion phasing prediction accurate under large valve overlap conditions.

CHAPTER EIGHT

COMBUSTION MODEL INPUTS ADAPTATION BASED ON FEEDBACK CYLINDER PRESSURE

To realize physics-based engine combustion phasing control, an accurate prediction model is required. This chapter introduces physics-based control-oriented laminar flame speed and turbulence intensity models that can be used in a quasi-dimensional turbulent entrainment combustion model. The influence of laminar flame speed and turbulence intensity on predicted mass fraction burned (MFB) profile during combustion is analyzed. Then a rule based methodology for laminar flame speed and turbulence intensity correction is proposed. The combustion model input adaptation algorithm can automatically generate laminar flame speed and turbulence intensity correction multipliers based on cylinder pressure feedback for different engine operating conditions. The correction multipliers can be stored into maps or regression equations that then feed into the main combustion model to improve overall prediction accuracy.

SI engine combustion rate is mainly decided by turbulent flame entrainment rate, mixture laminar flame speed and engine cylinder chamber geometry [70]. Knowledge of laminar flame speed is critical for both flame entrainment and burn-up [1]. For laminar flame speed (S_L), the key factors are air-to-fuel ratio (AFR), pressure, temperature, fuel type, and residual gas fraction (RGF) [117]. S_L is very sensitive to RGF, but accurate residual gas mass (RGM)/RGF measurement and modeling in real-time is challenging [2].

Turbulent flame entrainment models generally rely on turbulence intensity, u', to describe and approximate in-cylinder charge motion. Turbulence intensity is defined by the root-mean-squared velocity fluctuation in-cylinder, and has a primary effect on the turbulent flame entrainment process. The predicted magnitude of u', therefore, has a significant influence on combustion phasing prediction accuracy. Direct experimental turbulence intensity measurement during combustion is difficult due to the extreme atmosphere in-cylinder [118-121]. Without easily accessible empirical data to validate models, turbulence intensity predictions intended for real-time control can have limited prediction accuracy over a wide range of engine operating conditions.

8.1 S_L and U' effects on combustion analysis

Considering the combustion model adopted for this research both laminar flame speed and turbulence intensity have significant effects on burn rate. Laminar flame speed influences the unburned mixture entrainment rate and partially determines entrained eddy burn-up velocity. Turbulence intensity has a strong effect on the turbulent flame entrainment progress and also dictates entrained eddy size during burn-up. Both laminar flame speed and turbulence intensity are linked in their influence on combustion rate. In order to better understand how laminar flame speed and turbulence intensity influence the combustion process individually, a sensitivity analysis for both parameters is performed.

Figure 105 shows turbulence intensity sensitivity analysis results where the value changes from 70% to 130% of the base level. The results show that higher turbulence intensity increases combustion rate, especially during the rapid combustion phase (CA10-

CA90). It is further observed that u' mainly changes the MFB curve 'slope' during the rapid burning phase.

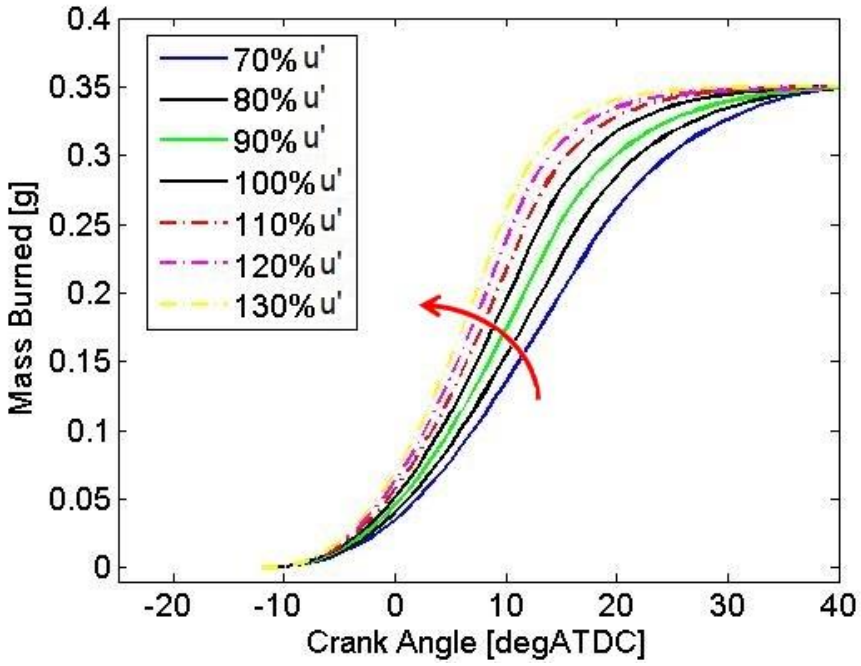

Figure 105: Turbulence intensity sensitivity analysis (1500RPM, 0.7bar MAP, 118ICL, 97ECL, Lambda=1)

Laminar flame speed sensitivity analysis results are shown in Figure 106. The S_L also changes from 70% to 130% of the base value from the prediction model. With an increase in laminar flame speed combustion rate increases, but at a lower amount than a similar change in turbulence intensity (S_L is often one magnitude smaller than u'). S_L mainly affects the early stage of combustion and has a relatively minor influence on MFB curve 'slope' during the rapid combustion phase.

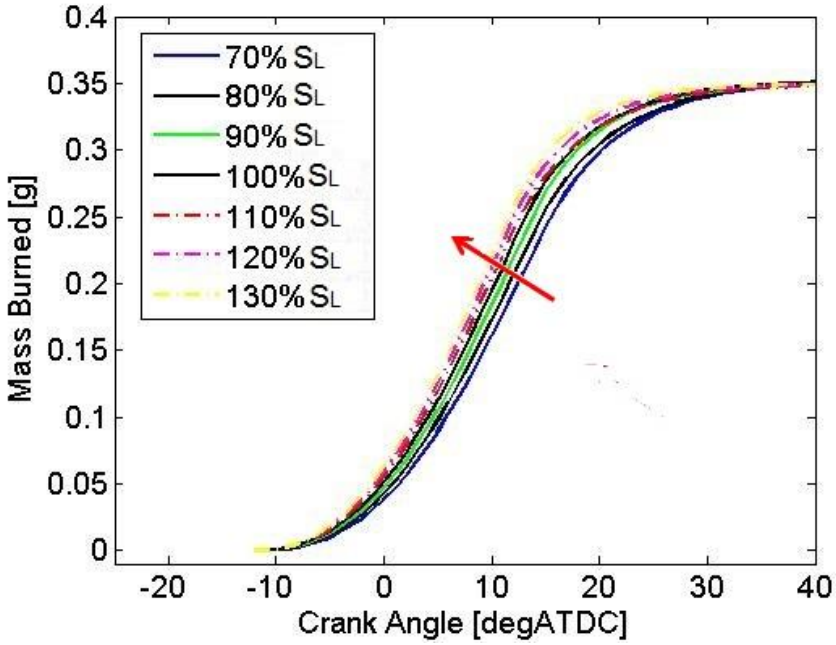

Figure 106: Laminar flame speed sensitivity analysis (1500RPM, 0.7bar MAP, 118ICL, 97ECL, Lambda=1)

In the semi-physical combustion model, laminar flame speed and turbulence intensity directly affect unburned mixture entrainment rate and burn up characteristic time (S_L decides the eddy burning speed and u' decides the eddy size). Figure 107 shows that the laminar flame speed value is relatively high at the start of combustion (SOC) and increases to the maximum value around TDC where it then decreases during the expansion stroke. As for turbulence intensity, it begins with a relatively low value and increases with combustion progress (unburned gas density increases due to burned gas expansion) and decreases near the end of combustion (where instantaneous cylinder volume change rate increases and cylinder pressure decreases). These observations suggest that u' primarily influences the MFB curve 'slope' during rapid burning and S_L influences the early combustion stage.

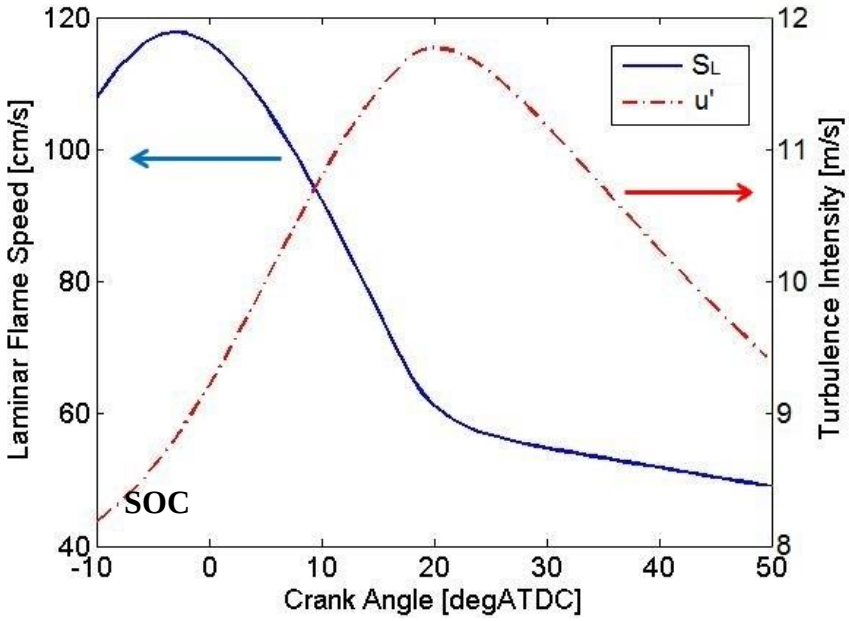

Figure 107: Laminar flame speed and turbulence intensity during combustion progress (2500RPM, 0.5bar MAP, 98ICL, 117ECL, Lambda=1)

8.2 Rule based S_L and U' correction algorithm

Sensitivity analysis results suggest that turbulence intensity mainly influences the MFB curve 'slope' during rapid combustion and laminar flame speed has a stronger influence on early combustion. Based on these characteristics, a rule based S_L and u' correction is introduced in Figure 108.

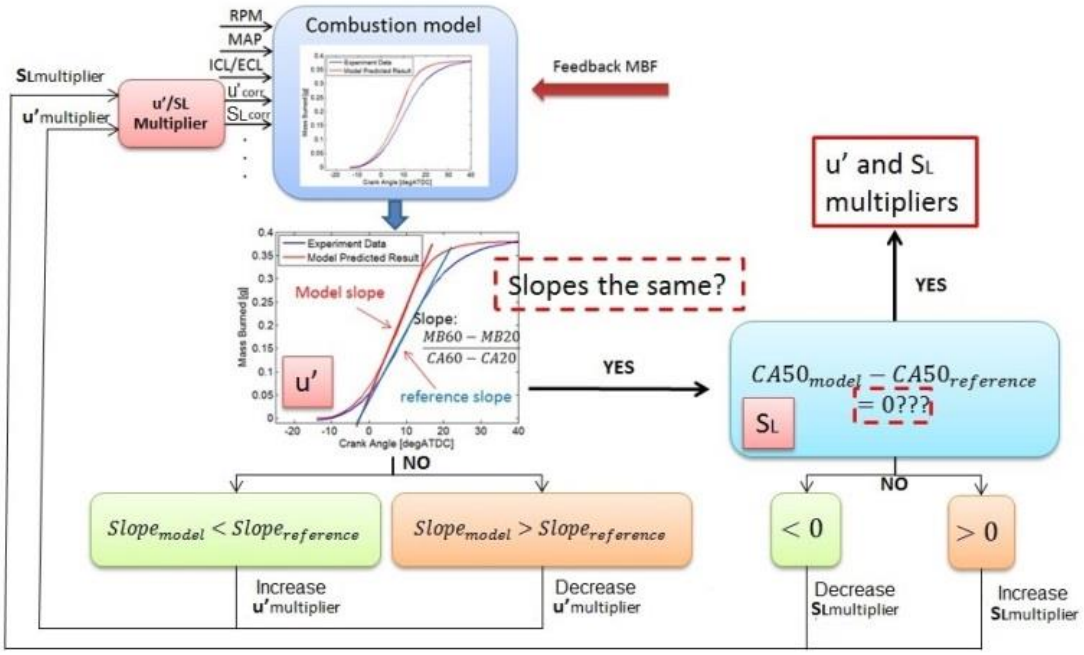

Figure 108: Block diagram of SL and u′ automatic calibration algorithm

8.2.1 Step 1: Mass fraction burned (MFB) curve generation from cylinder pressure

In order to calibrate S_L and u' a MFB curve is required as a reference for comparison. Cylinder pressure is the experimentally measured feedback signal and MFB characteristics must first be calculated. There are several available methods to realize the transformation. The Rassweiler and Withrow method is the simplest solution [122], but it requires special treatment of polytropic coefficients to accurately account for heat transfer. Thermodynamics based MFB calculation methods are more complex [1], but accuracy is expected to be higher due to more detailed system modeling. For this research a single-zone First Law of Thermodynamics based method that accounts for heat transfer is used to generate MFB information from cylinder pressure.

8.2.2 Step 2: MFB curve calculation from combustion model

The combustion model in Figure 108 is used to calculate 'predicted' MFB that is compared with the reference generated in step 1. Combustion rate is calculated based on Equations (1) and (2) and mass burned fraction is determined by Equation (50). The laminar flame speed and turbulence intensity values are calculated from the S_L and u' models described previously.

$$MFB = \frac{m_{burned}}{m_{total}} \tag{50}$$

8.2.3 Step 3: Turbulence intensity calibration

The turbulence intensity calibration process is performed next, while holding laminar flame speed constant. Based on the u' sensitivity analysis results, the rapid burning portion 'slopes' of the reference and modeled MFB curves are compared. The slope value is defined by the burned mass rate (g/CAD) during rapid combustion, and is calculated using Equation (51). In this equation MB60 is 60 percent of the total burned mass (g) and MB20 is 20 percent. CA60 is the corresponding crank angle location (CAD) where 60 percent of mixture mass burned and CA20 is where 20 percent of the mass is burned.

$$Slope_{MFB} = \frac{MB60 - MB20}{CA60 - CA20} \tag{51}$$

If the two slope values are the same (or a difference smaller than 2%), the turbulence intensity calibration is completed. Otherwise, the u' value is adjusted and applied back into the combustion model to re-calculate the 'predicted' MFB curve iteratively until the error tolerance is satisfied. Scaling of the u' value is based on the slope difference; a smaller 'predicted' slope means combustion rate is too low so

turbulence intensity is increased, and a larger slope corresponds to faster combustion and requires a decrease in turbulence intensity. Once a new u' value is reached the calibration multiplier is calculated by Equation (52).

$$M_{u'} = \frac{u'_{calibrated}}{u'_{model}} \tag{52}$$

$u'_{\text{calibrated}}$ is the newly calibrated turbulence intensity value and u'_{model} is the initial model calculation. Figure 109 shows a u' calibration example. The blue line is the reference MFB calculated from measured cylinder pressure. The black line represents the original MFB curve calculated with the base models for u' and S_L. The red line shows the MFB curve with re-calibrated turbulence intensity. Before calibration the model predicted MFB 'slope' is smaller than that of experimental data, so the turbulence intensity value is increased to match 'slopes' of the rapid combustion period.

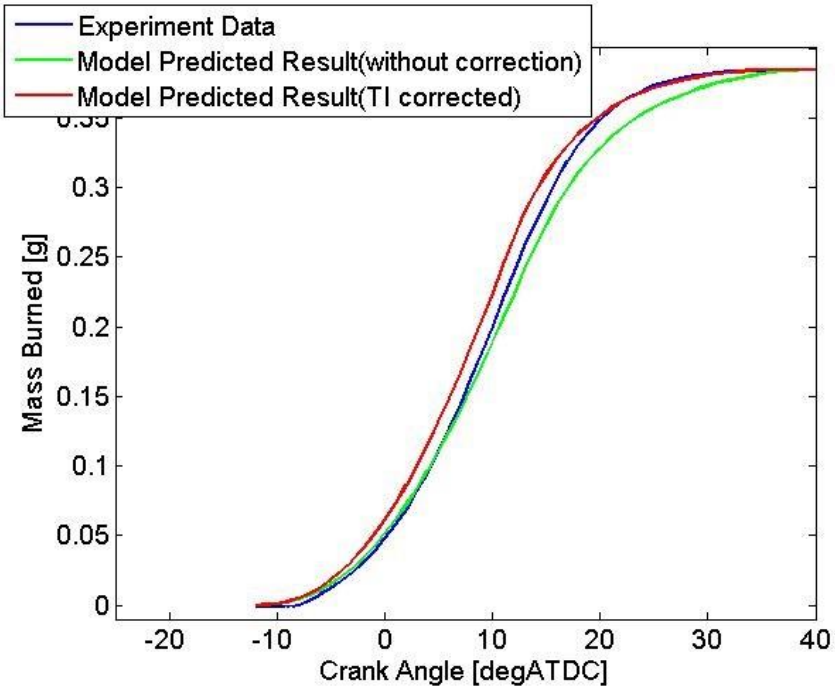

Figure 109: Turbulence intensity calibration result (1500RPM, 0.7bar MAP, 98ICL, 117ECL, Lambda=1)

8.2.4 Step 4: Laminar flame speed calibration

After the MFB curve slope is matched, S_L is adjusted to eliminate CA50 error. During the S_L calibration process the newly calibrated u' value is used. If model predicted CA50 is the same (or has a difference smaller than 0.2 deg) S_L calibration is complete. A later CA50 prediction than the reference implies a slower combustion rate and S_L should be increased (the opposite holds if predicted CA50 is earlier than the reference). After a satisfactory S_L is achieved the laminar flame speed multiplier is calculated by Equation (53).

$$M_{S_L} = \frac{S_{L_{calibrated}}}{S_{L_{model}}} \tag{53}$$

Figure 110 shows an example of S_L calibration results; the blue line is the reference MFB curve generated from cylinder pressure, the black line is the MFB curve with calibrated u', and the red line is the MFB curve with calibrated u' and S_L. After u' calibration, the MFB curve 'slopes' are matched but the combustion model calculated mass burn rate is larger (red line and blue line). To eliminate the error, S_L is decreased to offset CA50 error. Final results show the calibrated combustion model prediction (pink line) closely represents the measured reference through early and mid-combustion.

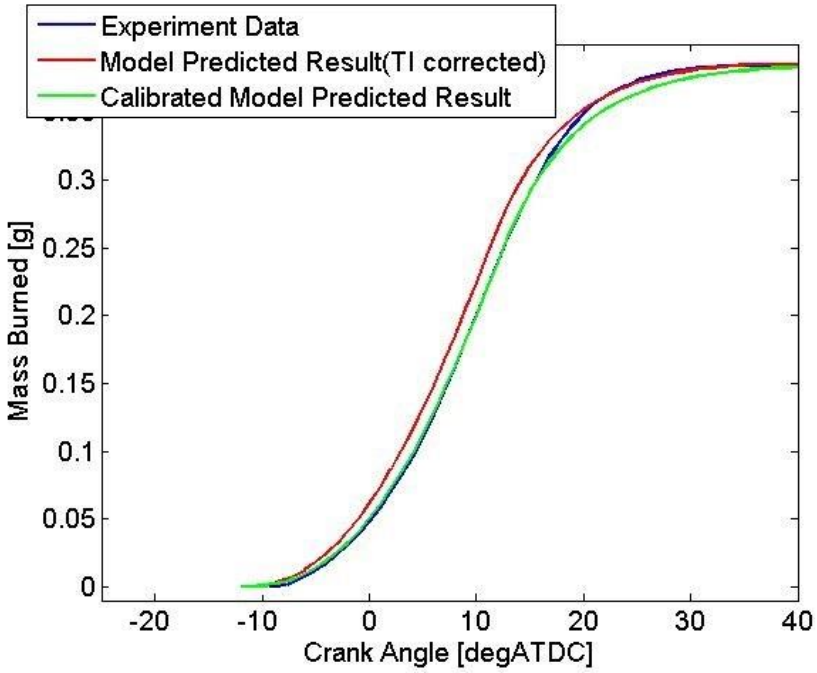

Figure 110: Laminar flame speed calibration result (1500RPM, 0.7bar MAP, 98ICL, 117ECL, Lambda=1)

8.3 Validation Results

Two sets of experimental data are used to validate the proposed input adaptation algorithm. Engine operating condition ranges for the experimental data sets are shown in Table 8. Data set 1 contains engine speeds from 1000 to 3000, MAP (as an indirect indicator of load) from 0.4 bar to 0.9 bar, intake valve centerline positions from 98 to 128 degree ATDC firing and exhaust valve centerline positions from 87 to 117 degree BTDC firing. Data set 1 includes 150 data points and is used to calibrate u' and S_L values to improve combustion phasing prediction accuracy. Then the calibrated u' and S_L multipliers are stored in a look up table. Data set 2, which has a slightly wider engine operating range, is used to demonstrate the feasibility of using u' and S_L multipliers calculated from data set 1 on new/unseen data.

Table 8. Engine experiment test points

Data set	Engine Speed (RPM)	MAP	ICL (degATDC)	ECL (degBTDC)
Data 1 (150 points)	1000-3000	0.4-0.9bar	98-128	87-117
Data 2 (200 points)	1000-3000	0.3-0.9bar	88-128	80-117

Figure 111 demonstrates calibration results for data set 1. This figure shows the comparison between the reference CA00-CA50 combustion duration and combustion model predicted values (the combustion model starts calculation at the same CA00 values for both reference and combustion model prediction data). In Figure 111, blue dots signify combustion model prediction results without u' and S_L calibration. The root-mean-square-error (RMSE) is 0.8 CAD with a maximum error of 2.2 CAD. Black stars are calibrated prediction results. The accuracy improvement is obvious and the RMSE is decreased to 0.1 CAD and maximum error becomes 0.2 CAD.

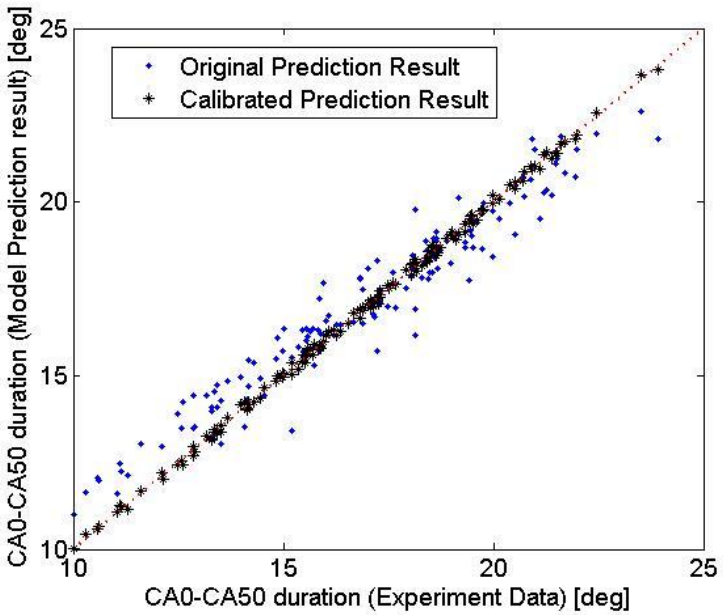

Figure 111: Combustion phasing prediction results comparison (w/o calibration the RMSE of CA0-CA50 is 0.8 CAD and maximum error of 2.2 CAD; the calibrated RMSE is 0.1 CAD with maximum error of 0.2 CAD).

Figure 112 and Figure 113 show calibrated turbulence intensity and laminar flame speed multipliers for different engine speeds and intake manifold pressures with fixed intake and exhaust valve timing. For simplification, valve timing effects on u' and S_L multipliers are not discussed here. The newly calibrated u' multipliers show that the base model ignores engine load (with higher manifold pressure, intake mass flow will increase, thus increasing turbulence in cylinder). These results suggest that the process is reasonable and has the capability to improve combustion rate prediction accuracy in a reasonable manner.

Similarly, Figure 113 shows S_L multipliers for different engine speeds and loads. The results give a clear indication that the base S_L model overestimates S_L values for higher manifold pressures. This may be caused by inaccurate residual gas fraction input or could be the S_L model itself (i.e. inaccurate fit constants or neglected physics).

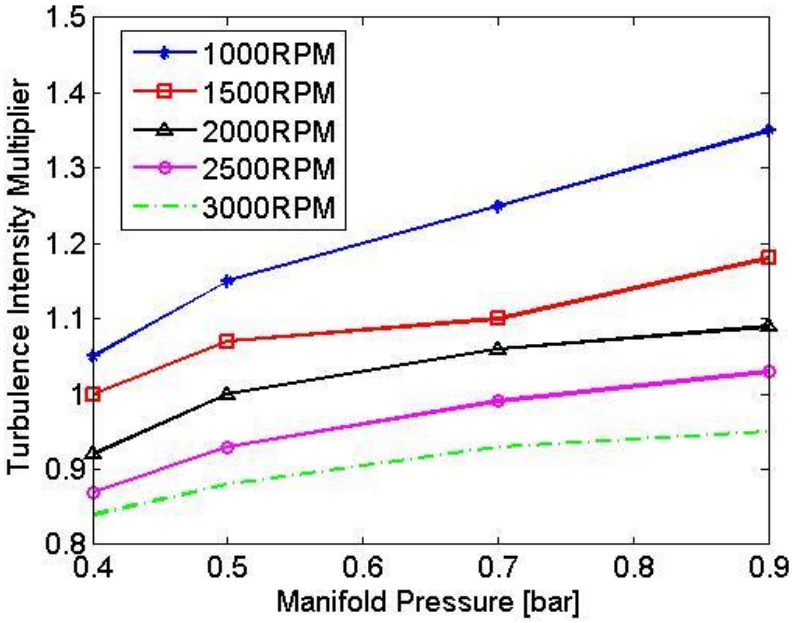

Figure 112: Calculated u' multipliers from sample data

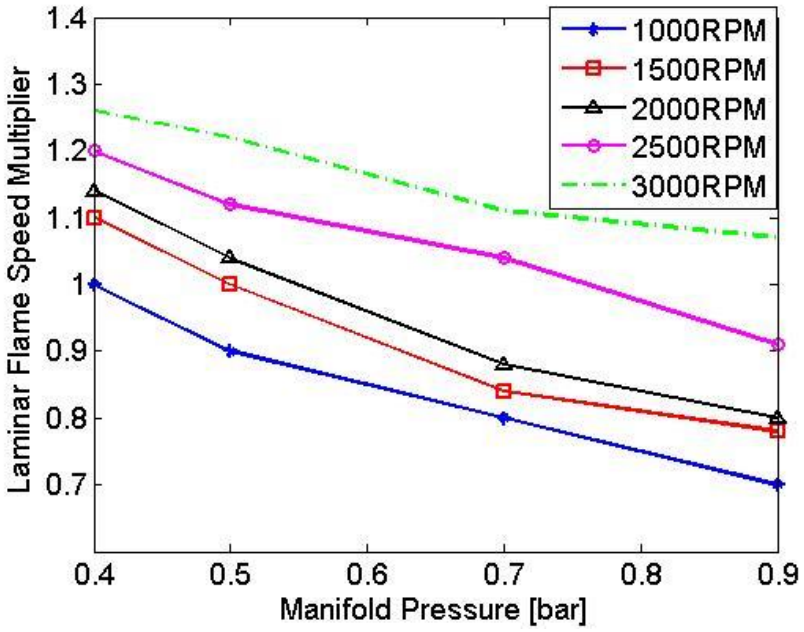

Figure 113: Calculated SL multipliers from sample data

Theoretically, the S_L and u' multipliers for different engine speeds and engine loads can be stored into look up tables and applied for future use. Data set 2 is used to validate the adaptive ability of these multipliers. Figure 114 shows the validation results. The blue dots are the uncorrected combustion model prediction results (RMSE is 1.2 CAD and maximum error of 3.4 CAD). Baseline prediction accuracy is lower than the previous data set 1, possibly caused by wider engine operating conditions for data set 2 (some points have really large overlap and high residual gas). The black stars are combustion prediction results with u' and S_L multipliers looked up from pre-stored tables generated from data set 1. Applying u' and S_L multipliers from data set 1 to data set 2 effectively improved prediction accuracy. In this case, RMSE is decreased to 0.5 CAD and maximum error reduced to 1.2 CAD.

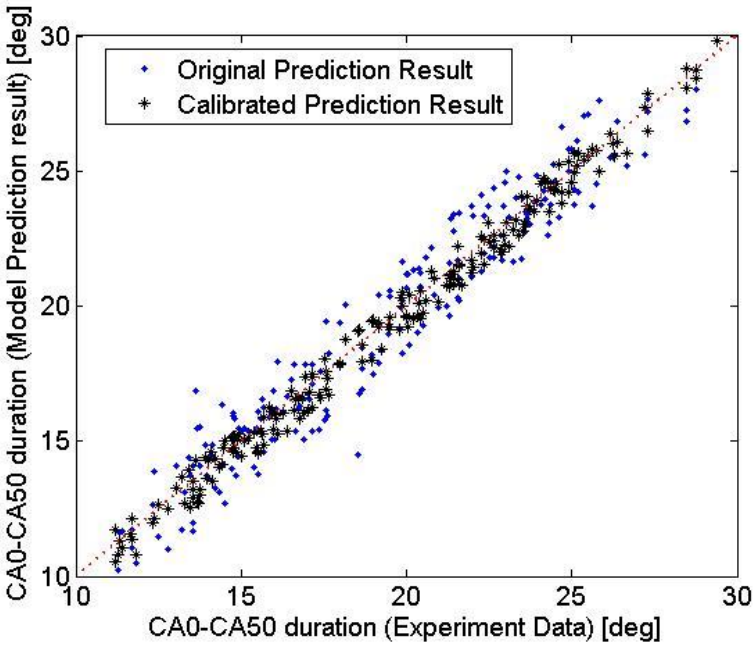

Figure 114: Validation results for combustion phasing prediction (RMSE is 1.2 CAD w/o calibration, maximum error 3.4 CAD; with u' and SL multipliers (calibrated from data set 1), RMSE is 0.5 CAD and maximum error is 1.2 CAD)

CHAPTER NINE

SUMMARY AND CONCLUSIONS

9.1 Thesis Summary

The objective of this thesis is to realize real-time SI engine combustion phasing prediction and control based on physics-based models. The models presented are suitable for high degree of freedom engine applications due to their adaptive ability for various engines. Considering the realization of the real-time combustion phasing prediction and control, model complexity could significantly affect the computational effort. In this project, several experimental data based semi-physical models are developed to balance computational efforts and physics based model accuracy. The semi-physical models reasonably combine critical physics and experiment data to effectively and accurately predict critical input values for combustion phasing prediction. The quasi-dimensional turbulent flame entrainment combustion model is applied for the combustion rate calculation in this project. It is suitable for SI engine combustion where the unburned premixed mixture is ignited by the spark and propagates outwards at a turbulent flame speed. This model accurately captures impact of critical physical parameters, like turbulence intensity, laminar flame speed, gas density, flame front area and length scales, to simulate the combustion event process in a SI engine.

In this research, a physics based flame kernel development duration prediction model is proposed to calculate the duration from the spark to the start of combustion. This approach could significantly improve the combustion phasing prediction at the early stage of combustion and also reduce computational effort. The spark selection algorithm

realizes combustion phasing control without inverting the physical models which saves modeling and calculation time. A new cylinder pressure feedback based turbulence intensity and laminar flame speed automatic adaptation method is also proposed in this project. The new method separates different physics effects on combustion rate based on experimentally measured cylinder pressure. It effectively adjusts calibration constants to correct the turbulence intensity and laminar flame speed models and compensate for model error, engine variation and engine aging effects on combustion phasing prediction inaccuracy.

The physics based combustion phasing prediction and control system combines the input models, turbulent flame entrainment combustion model, flame kernel development model and spark selection algorithm to realize the real-time engine control. Steady-state and transient real-time test data show that accurate combustion phasing prediction and target CA50 control is achieved. A significant contribution of this research is the validation which indicates that physics-based feedforward engine combustion phasing control can be realized. The accuracy of the physics-based approach challenges that of state of art map based combustion phasing control algorithms, and the new method requires significantly less calibration (due to its physics-based nature).

9.2 Significant Conclusions and Findings

Contributions and improvements are realized in five distinct areas: (1) physics based internal residual gas mass prediction, (2) physics based flame kernel development duration calculation, (3) real-time cylinder pressure prediction, (4) cylinder pressure based combustion model input automatic calibration, and (5) the realization of physics-

based real-time engine combustion phasing prediction and control. Significant findings in each category are described separately in the following sections.

9.2.1 Physics Based Internal Residual Gas Mass Prediction

In this research, a physics-based control oriented residual gas mass (RGM) prediction method has been proposed. The RGM model is based on Bernoulli's principle and considers engine operating conditions, valve timing and geometry, and piston motion effects. Moreover, to more accurately estimate the burned gas back flow, this model captures gas wave dynamic effects in intake and exhaust manifold pressures which have been ignored for the other presented methods. This RGM model requires minimal experimental data for calibration due to its physics-based structure. As for the result, the model is described in detail and its prediction accuracy is compared to that of a high fidelity simulation that utilizes experimentally measured crank angle resolved intake, exhaust, and cylinder pressures as boundary conditions. For this RGM model validation, the model is incorporated into a rapid-prototype control system for real-time operation during transient and steady-state engine operation. The results show that the proposed RGM model provides real-time predictions within 1.9-2.3% RGF, creating relative estimation errors in the range of 10-24%, and is capable of running real-time for engine control.

9.2.2 Physics Based Flame Kernel Development Duration Calculation

A physics based flame kernel development duration model is developed in this research. This model is control oriented and simplified for real-time calculation. It is

based on the critical physics for gas density, fuel mass, cylinder pressure, engine speed and residual gas fraction, all of which can significantly affect flame kernel development. Then, experiment test data is applied to calibrate the model constants.

Different from the previous physical and chemical energy balance based flame kernel models, the new model has much less computational effort but retains predictive capability due to its physics foundation. The proposed flame kernel development model also helps the realization of the separate engine combustion rate prediction (before and after start of combustion). The model validation results show the proposed flame kernel development duration prediction method can accurately calculate the time from spark to start of combustion. The successful development of this flame kernel model significantly helps improve the accuracy of the combustion phasing prediction and reduce the computational effort of the physical models based combustion phasing prediction and control system (low flame area conditions are difficult to model accurately with the rapid-burning model, the flame kernel model replaces that model to more accurately predict early combustion).

9.2.3 Real-Time Cylinder Pressure Prediction

Engine cylinder pressure plays a critical role in many models for the engine combustion phasing prediction, for instance laminar flame speed calculation, flame kernel duration prediction, cylinder temperature calculation, expansion work calculation and so on. For production engines, installing a transducer to experimentally measure cylinder pressure could significantly increase the cost. In this research, in order to realize

combustion phasing prediction and control a real-time physics based cylinder pressure prediction model is proposed.

The real-time cylinder prediction model is consisted of two sections. The first section is calculating cylinder pressure before the start of combustion. For this section, the cylinder pressure model is a semi-physical model which captures the critical physics and based on experimental data to predict the cylinder pressure at the intake valve closing. Then the cylinder pressure during the compression can be calculated based on ideal gas law. The second section calculates cylinder pressure for the part after the start of combustion. In this section, ideal gas law and thermodynamic first law are applied to calculate cylinder pressure from the initial cylinder pressure condition and the detail combustion burning rate. The validation results how the proposed real-time cylinder pressure prediction model could very accurately calculate crank angle resolution cylinder pressure for the required models.

9.2.4 Turbulence Intensity and Laminar Flame Speed Model Adaptation

This research proposes a rule based combustion model adaptation algorithm for turbulence intensity and laminar flame speed that utilizes cylinder pressure feedback. A sensitivity analysis was performed to separate laminar flame speed and turbulence intensity effects on combustion rate (predicted from a semi-physical turbulent flame entrainment combustion model). Rules to adjust turbulence intensity and laminar flame speed values to achieve more accurate burn rate prediction were then developed. Results show the proposed algorithm is effective in improving combustion phasing prediction over a wide range of operating conditions. The calibrated inputs generate an accurately

shaped MFB curve (accurate for most of the mass burn points), instead of just matching specific combustion phasing points, like CA50. Validation results show the calibration multipliers adapt to a wide range of engine operating conditions and effectively improve combustion rate prediction accuracy. Research results show the combustion model prediction error (RMSE) decreased by 88% (from 0.8 CAD to 0.1CAD) for fitting data and 58% (from 1.2 CAD to 0.5 CAD) for validation data when this method was utilized.

This automatic combustion model inputs calibration algorithm can help improve the accuracy of the combustion phasing prediction. This method can automatically correct model prediction inaccuracy in physics-based input models and also capture engine aging effects on the combustion phasing prediction.

9.2.5 Realization of Physical Model Based Real-Time Engine Combustion Phasing Control

As engines are equipped with an increased number of control actuators to meet fuel economy targets they become more difficult to control and calibrate. The additional complexity created by a larger number of control actuators motivates the use of physics-based control strategies to reduce calibration time and complexity. However, to realize the physical models based combustion phasing prediction and control is not easy. The most obvious difficulty could be the computation capability of the current ECU. As a result, the physical models based combustion phasing prediction and control system is required to be developed control oriented. The simplification of the models could more or less influence the predictive ability and accuracy of the models, so it is a challenge to

reasonably develop a high fidelity physical model based combustion phasing prediction and control system which can be operated real-time in an ECU.

In this research, a quasi-dimensional turbulent flame entrainment phasing prediction and control system is proposed. The system includes critical physics based control oriented models to support the combustion model combustion rate prediction. Each model has been validated and the prediction accuracies are very good. Finally, all the combustion phasing prediction models, knock and COV models and the spark selection model are combined together to setup the completed physical models based combustion phasing prediction and control system. The real-time validation results show the accurate and robust combustion phasing control from this proposed system (CA50 RMSE is about 2-3 CAD).

The realization of the physics-based real-time combustion phasing control in this research paves the way for the future model based engine control techniques which could significantly increase the adaptive ability of the control system and reduce calibration time and labor.

9.3 Future work

Future research on several key topics could improve the robustness and predictive capability of the physics based models for combustion phasing control routine discussed in this thesis. A list of suggested areas of improvement is as follows:

- Development of an improved residual gas fraction prediction method specifically for high valve overlap. Better reference residual gas

mass/fraction data could help improve the accuracy of the RGM model prediction.

- Laminar flame speed model modification for residual gas fraction term. The calibration constant for residual gas fraction term in the laminar flame speed model might not be accurate and experiment data are required to re-calibrate the constant.
- Implement the combustion model inputs adaptation system into ECU to realize online combustion phasing prediction system calibration. A storage method is required to record all the useful feedback data to setup the reference MFB curve for calibration application. A reasonable data record routine is required to correctly and effectively pick out useful measurement data.

REFERENCE

1. *Heywood J.B. , Internal Combustion Engine Fundamentals, MacGraw Hill, 1988*

2. *Prucka R., "An Experimental Characterization of a High Degree of Freedom Spark-Ignition Engine to Achieve Optimized Ignition Timing Control", Dissertation for the degree of Doctor of Philosophy,2008*

3. *Ayala F. A., Gerty M. D. and Heywood J. B., "Effects of Combustion Phasing, Relative Air-fuel Ratio, Compression Ratio, and Load on SI Engine Efficiency",SAE 2006-01-0229, 2006*

4. *Hu E. and Huang Z., "Optimization on Ignition Timing and EGR Ratio of a Spark-Ignition Engine Fuelled with Natural Gas-Hydrogen Blends", SAE 2011-01-0918, 2011*

5. *Lee S. and Bae C., "Effects of Engine Operating Conditions on Catalytic Converter Temperature in an SI Engine", SAE 2002-01-1677, 2002*

6. *Choi M., Sun H. Lee C., Myung C., Kim W. and Choi J., "The Study of HC Emission Characteristics and Combustion Stability with Spark Timing Retard at Cold Start in Gasoline Engine Vehicle", SAE 2000-01-1082, 2000*

7. *Lupescu J. A., Chanko T. B., Richert J. F. and Mauti A. A., "The Effect of Spark Timing on Engine–Out Hydrocarbon Speciation and Hydrocarbon Trap Performance", SAE 2009-01-1068, 2009*

8. *Xiao B., Wang S. and Prucka R., "Virtual Combustion Phasing Target Correction in the Knock Region for Model-Based Control of Multi-Fuel SI Engines", SAE 2013-01-0307*

9. *Wildman C. B., Cheng W. K., "The Effects of Charge Motion and Laminar Flame Speed on Late Robust Combustion in a Spark- Ignition Engine", SAE 2010-01-0350, 2010*

10. *Adb-Alla T., Pucher G. R., Bardon M. F. and Gardiner D. P., "Effects of Spark Characteristics on Engine Combustion with Gasoline and Propane", SAE 2003-01-3264, 2003*

11. *Andrie M. J., "Non-Intrusive Low Cost Cylinder Pressure Transducer for Internal Combustion Engine Monitoring and Control", SAE 2009-01-0245, 2009*

12. *Toth D., Shaw T., Wlodarczyk M. and Cummings C., "Cylinder Head Gasket with Integrated Combustion Pressure Sensors for Advanced Engine Controls", SAE2011-01-0938,2011*

13. *Schoop U., Reeves J., Watanabe S. and Butts K., "Steady-State Engine Modeling for Calibration: A Productivity and Quality Study", Design of Experiments (DoE) in Vehicle and Engine Development: 2nd U.S. Conference, 2012*

14. *Jiang S., Nutter D. and Gullitti A., "Implementation of Model-Based Calibration for a Gasoline Engine", SAE 2012-01-0722, 2012*

15. *Ropke K., Schaum S., Kraschinski S. and Berlin IAV," Current Focus for Model based Calibration", Design of Experiments (DoE) in Vehicle and Engine Development: 2nd U.S. Conference,2012*

16. *Godward T., Schilling H. and Schaum S., "Use of Dynamic Testing and Modeling in the Engine Calibration Process", Design of Experiments (DoE) in Vehicle and Engine Development: 2nd U.S. Conference,2012*

17. Zhu, G., Daniels, C., and Winkelman, J., "MBT Timing Detection and its Closed-Loop Control Using In-Cylinder Pressure Signal," SAE Technical Paper 2003-01-3266, 2003

18. Zhu, G., Daniels, C., and Winkelman, J., "MBT Timing Detection and its Closed-Loop Control Using In-Cylinder Ionization Signal," SAE Technical Paper 2004-01-2976, 2004

19. Zhu, G., Haskara, I., and Winkelman, J., "Stochastic Limit Control and Its Application to Knock Limit Control Using Ionization Feedback," SAE Technical Paper 2005-01-0018, 2005

20. Pipitone, E. and Beccari, A., "A Study on the Use of Combustion Phase Indicators for MBT Spark Timing on a Bi-Fuel Engine," SAE Technical Paper 2007-24-0051, 2007

21. A and Naber, J., "Ionization Signal Response during Combustion Knock and Comparison to Cylinder Pressure for SI Engines," SAE Int. J. Passeng. Cars - Electron. Electr. Syst. 1(1):349-364, 2009

22. Xiao B., Wang S. and Prucka R., "A Semi-Physical Artificial Neural Network for Feed Forward Ignition Timing Control of Multi-Fuel SI Engines", SAE 2013-01-0324

23. Vibe, I.I., "Semi-empirical expression for combustion rate in engines", Proceedings of Conference on piston engines, USSR Academy of sciences, Moscow, pp. 186-191, 1956.

24. Wiebe I.I., "Brennverlauf und Kreisprozeb von Ver-brennungsmotoren". In VEB-Verlag Technik, Berlin, 1970.

25. Lindström, F., Ångström, H., Kalghatgi, G., and Möller, C., "An Empirical SI Combustion Model Using Laminar Burning Velocity Correlations," SAE Technical Paper, 2005-01-2106, 2005.

26. Longwic, R., "Modelling the Combustion Process in the Diesel Engine with the Use of Neural Networks," SAE Technical Paper 2008-01-2446, 2008, doi:10.4271/2008-01-2446.

27. Maass, B., Deng, J., and Stobart, R., "In-Cylinder Pressure Modelling with Artificial Neural Networks," SAE Technical Paper 2011-01-1417, 2011, doi:10.4271/2011-01-1417.

28. Perhinschi, M., Wayne, W., Clark, N., and Lyons, D., "Neural Network Modeling of Emissions from Medium-Duty Vehicles Operating on Fisher-Tropsch Synthetic Fuel," SAE Technical Paper 2007-01-1080, 2007.

29. De Cesare, M. and Covassin, F., "Neural Network Based Models for Virtual NOx Sensing of Compression Ignition Engines," SAE Technical Paper 2011-24-0157, 2011, doi:10.4271/2011-24-0157.

30. Xiao B., Wang S. and Prucka R., "A Semi-Physical Artificial Neural Network for Feed Forward Ignition Timing Control of Multi-Fuel SI Engines", SAE 2013-01-0324

31. Cavina N. and Suglia R., "Spark Advance Control based on a Grey Box Model of the Combustion Process", SAE 2005-01-3760, 2005

32. Schlosser, A., Kinoo, B., Salber, W., Werner, S. et al., "Accelerated Powertrain Development Through Model Based Calibration," SAE Technical Paper 2006-01-0858, 2006

33. N. C. Blizard and J. C. Keck, "Experimental and Theoretical Investigation of Turbulent Burning Model for Internal Combustion Engines", SAE Paper 740191.

34. Tabaczynski, R., Ferguson, C., Radhakrishnan, K., "A Turbulent Entrainment Model for Spark-Ignition Engine Combustion," SAE Paper No. 770647, 1977.

35. Tabaczynski, R., Trinker, F., Shannon, B., "Further Refinement and Validation of a Turbulent Flame Propagation Model for Spark Ignition Engines," Combustion and Flame, 39, 111-121, 1980.

36. Filipi, Z., Assanis, D., "The Effect of the Stroke-to-Bore Ratio on Combustion, Heat Transfer and Efficiency of a Homogenous Charge Spark Ignition Engine of Given Displacement," Int. Journal of Engine Research, Vol. 1, No. 2, 191-208, 2000.

37. Wong, V., Hoult, D., "Rapid Distortion Theory Applied to Turbulent Combustion," SAE Paper No. 790357, 1979.

38. Durbin, P., Zeman, O., "Rapid Distortion Theory for Homogeneous Compressed Turbulence with Application to Modelling," J. Fluid Mechanics, Vol. 242, pg. 349-370, 1992.

39. Keck J. C., Heywood J. B. and Noske G., "Early Flame Development and Burning Rates in Spark Ignition Engines", SAE 870164, 1987

40. Boiarciuc A. and Floch A., "Evaluation of a 0D Phenomenological SI Combustion Model", SAE 2011-01-1894, 2011

41. Schmid, A., Grill, M., Berner, H., Bargende, M. et al., "Development of a Quasi-Dimensional Combustion Model for Stratified SI-Engines," SAE Int. J. Engines 2(2):48-57, 2010

42. Rakopoulos, C., Michos, C., and Giakoumis, E., "Thermodynamic Analysis of SI Engine Operation on Variable Composition Biogas-Hydrogen Blends Using a Quasi-Dimensional, Multi-Zone Combustion Model,"SAE Int. J. Engines 2(1):880-910, 2009

43. Lafossas, F., Colin, O., Le Berr, F., and Menegazzi, P., "Application of a New 1D Combustion Model to Gasoline Transient Engine Operation," SAE Technical Paper 2005-01-2107

44. Shi X., Li G. and Zhou L., "DI Diesel Engine Combustion Modeling Based on ECFM-3Z Model", SAE 2007-01-4138, 2007

45. Tan, Z. and Reitz, R., "Modeling Ignition and Combustion in Spark-ignition Engines Using a Level Set Method," SAE Technical Paper 2003-01-0722, 2003.

46. Chopp, D. L. and Sethian, J. A., Flow under curvature: Singularity formation, minimal surfaces, and geodesics, Journal of Experimental Mathematics, 2(4):235-255, 1993.

47. Tan, Z. and Reitz, R., "Development of a Universal Turbulent Combustion Model for Premixed and Direct Injection Spark/Compression Ignition Engines," SAE Technical Paper 2004-01-0102, 2004.

48. Sethian, J. A., Level Set Methods: Evolving Interfaces in Geometry, Fluid Mechanics, Computer Vision and Materials Sciences , Cambridge University Press, 1996.

49. Naoumov, V., Demin, A., and Sokolov, A., "Three - Zone Model of Combustion and Chemical Non-Equilibrium Ionization in the SI Engine," SAE Technical Paper 2004-01-0622, 2004.

50. Hassaneen A E., "Prediction of Optimum Ignition Timing in a Natural Gas-Fueled Spark Ignition Engine Using Neural Network", SAE 2006-01-1347, 2006

51. Boiarciuc A. and Floch A., "Evaluation of a 0D Phenomenological SI Combustion Model", SAE 2011-01-1894, 2011

52. *Ma F., Liu H., Wang Y., Ding S. and Zhao S., "A Quasi-Dimensional Combustion Model for SI Engines Fuelled by Hydrogen Enriched Compressed Natural Gas", SAE 2008-01-1633, 2008*

53. *MAGNUSSEN B. F., HJERTAGER B. H., "On mathematical modeling of turbulent combustion with special emphasis on soot formation and combustion", 16th Symp (Int) on Combust, 1977*

54. *Flohr P. and Pitsch H., "A turbulent flame speed closure model for LES of industrial burner flows", 2000*

55. *Boyde J. M., Clercq P. C. L., Domenico M. D. and Aigner M., "Extension of the turbulent flame speed closure model to ignition in multiphase flows", Combustion and Flame, 2012*

56. *Bougrine S., Richard S. and Veynante D., "Modelling and Simulation of the Combustion of Ethanol blended Fuels in a SI Engine using a 0D Coherent Flame Model", SAE 2009-24-0016, 2009*

57. *Teraji A., Tsuda T., Noda T., Kubo M. and Itoh T., "Development of a Novel Flame Propagation Model (UCFM: Universal Coherent Flamelet Model) for SI Engines and Its Application to Knocking Prediction", SAE 2005-01-0199, 2005*

58. *Amin E. and Celik I., "A Validation Study for a Turbulent Mixing Model Based on the Probability Density Function Approach", SAE 1999-01-0231, 1999*

59. *Mauviot G., Albrecht A. and Poinsot T. J., "A New 0D Approach for Diesel Combustion Modeling Coupling Probability Density Function with Complex Chemistry", SAE 2006-01-3332, 2006*

60. Bordet N., Caillol C. and Higelin P., "A Physical 0D Combustion Model Using Tabulated Chemistry with Presumed Probability Density Function Approach for Multi-Injection Diesel Engines", SAE 2010-01-1493, 2010

61. S. Russ, G, Lavoie, and W. Gai, "SI engine operation with retarded ignition: Part 1 – Cyclic vaiations", SAE Technical Papers, no. 90093, 1999.

62. Fox, J., Cheng, W., Heywood, J., "A Model for Predicting Residual Gas Fraction in Spark-Ignition Engines," SAE Paper No. 931025, 1993.

63. Shayler, P., Winborn, L., Hill, M., "The Influence of Gas/Fuel Ratio on Combustion Stability and Misfire Limits of Spark Ignition Engines," SAE Paper No. 2000-01-1208, 2000.

64. Shayler, P., Lai, W., Brown, N., Harbor, N., "Limits of Charge Dilution, Fuel and Air Proportions for Stable Combustion in Spark Ignition Engines," SAE Paper No. 2004-01-1533, 2004.

65. Amer, A., Zhong, L., "A Semi-Empirical Model for Fast Residual Gas Fraction Estimation in Gasoline Engines," SAE Paper No. 2006-01-3236, 2006.

66. Kale, V., Yeliana, Y., Worm, J., and Naber, J., "Development of an Improved Residuals Estimation Model for Dual Independent Cam Phasing Spark-Ignition Engines," SAE Technical Paper 2013-01-0312, 2013.

67. Senecal, J., Xin, J., Reitz, R., "Predictions of Residual Gas Fraction in IC Engines," SAE Paper No. 962052, 1996

68. Prucka, R., Lee, T., Filipi, Z., and Assanis, D., "Turbulence Intensity Calculation from Cylinder Pressure Data in a High Degree of Freedom Spark-Ignition Engine," SAE Technical Paper 2010-01-0175, 2010

69. LIU, C., JIANG, D., and OBOKATA, T., "A Simplified Turbulence Model for In-cylinder Gas Flow in Quasi-dimensional Turbulence Combustion Model for Spark-ignition Engines," SAE Technical Paper 2000-01-2803, 2000

70. Poulos, S.G. and Heywood, J.B., "The Effect of Chamber Geometry on Spark-Ignition Engine Combustion," SAE Technical Paper 830334, 1983.

71. Pischinger S. MIT PhD thesis 1989

72. Hinze P.C. MIT PhD thesis 1997

73. Herweg, R. and Maly, R., "A Fundamental Model for Flame Kernel Formation in S. I. Engines," SAE Technical Paper 922243, 1992

74. Woschni, G., "A Universally Applicable Equation for the Instantaneous Heat Transfer Coefficient in the Internal Combustion Engine," SAE Technical Paper 670931, 1967

75. Ma, F., Shen, H., Liu, C., Wu, D. et al., "The Importance of Turbulence and Initial Flame Kernel Center Position on the Cyclic Combustion Variations for Spark-Ignition Engine," SAE Technical Paper 961969, 1996

76. Mittal, V., Revier, B., and Heywood, J., "Phenomena that Determine Knock Onset in Spark-Ignition Engines," SAE Technical Paper 2007-01-0007, 2007

77. Liu, Y., Shi, X., Deng, J., Chen, Y. et al., "Experimental Study on the Characteristics of Knock under DI-HCCI Combustion Mode with Ethanol/Gasoline Mixed Fuel," SAE Technical Paper 2013-01-0544, 2013

78. Noda, T., Hasegawa, K., Kubo, M., and Itoh, T., "Development of Transient Knock Prediction Technique by Using a Zero-Dimensional Knocking Simulation with Chemical Kinetics," SAE Technical Paper 2004-01-0618, 2004

79. Westbrook, C.K., Warnatz, J., and Pitz, W.J., "A detailed chemical kinetic reaction mechanism for the oxidation of iso-octane and nheptane over an extended temperature range and its application to analysis of engine knock.", Twenty-second Symposium (Int.) on Combustion, The Combustion Institute, p.893-901, (1988).

80. Glassman, I., "Combustion", Academic Press, 1977.

81. Kasseris, E., "Knock Limits in Spark Ignited Direct Injected Engines Using Gasoline/Ethanol Blends", PhD dissertation, Massachusetts Institute of Technology, 2011.

82. Assanis D. N., Filipi Z. S., Fiveland S. B., Syrimis M., 'A predictive ignition delay correlation under steady-state and transient operation of a direct injection diesel engine.' J. Engng Gas Turbines Power 125(2003)

83. Douaud, A. and Eyzat, P., "Four-Octane-Number Method for Predicting the Anti-Knock Behavior of Fuels and Engines," SAE Technical Paper 780080, 1978,

84. Wo, S. K., "The Effects of Pressure, Temperature and Concentration on the Reactivity of Alkanes: Experiments and Modeling in a Rapid Compression Machine" 27th International Symposium on Combustion, University of Colorado at Boulder, September 2-7,1998

85. Kee, R. J.; Rupley, F. M.; Miller, J. A. "CHEMKIN-II: A Fortran Chemical Kinetics Package for the Analysis of Gas Phase Chemical Kinetics" Sandia Report no. SAND 89-8009B; Sandia National Laboratories, (1989).

86. Viljoen, C., Yates, A., Swarts, A., Balfour, G. et al., "An Investigation of the Ignition Delay Character of Different Fuel Components and an Assessment of Various Autoignition Modelling Approaches," SAE Technical Paper 2005-01-2084, 2005, doi:10.4271/2005-01-2084

87. Brecq, G., Ramesh, A., Tazerout, M., and Le Corre, O., "An Experimental Study of Knock in a Natural Gas Fuelled Spark Ignition Engine," SAE Technical Paper 2001-01-3562, 2001

88. Yates, A. and Viljoen, C., "An Improved Empirical Model for Describing Auto-ignition", SAE 2008-01-1629, 2008

89. Yates, A., Swarts, A., and Viljoen, C., "Correlating Auto-Ignition Delays And Knock-Limited Spark-Advance Data For Different Types Of Fuel," SAE Technical Paper 2005-01-2083, 2005

90. Thomas, S., Kannan, R., Saroop, A., and Sharma, S., "A Study on the Idle Combustion Stability of a CNG Powered Naturally Aspirated Engine," SAE Technical Paper 2013-26-0003, 2013

91. Bozza, F, De Bellis, V., and Siano, D, "A Knock Model for 1D Simulations Accounting for Cyclic Dispersion Phenomena", SAE Technical Paper 2014-01-2554, 2014, doi: 10.4271/2014-01-2554.

92. Young, M., "Cyclic Dispersion - Some Quantitative Cause-and-Effect Relationships," SAE Technical Paper 800459, 1980, doi: 10.4271/800459.

93. *Ozdor, N., Dulger, M., and Sher, E., "Cyclic Variability in Spark Ignition Engines A Literature Survey," SAE Technical Paper 940987, 1994, doi: 10.4271/940987.*

94. *Aleiferis, P.G Hardalupas, Y. Taylor, A.M.K.P., Lshii, K., and Urata, Y., "Flame chemiluminescence studies of cyclic combustion variations and air-to-fuel ratio of the reacting mixture in a lean-bun stratified-charge spark-ignition engine", Cobustion and Flame, vol. 136, no. 1-2, pp. 72-90, Jan., 2004.*

95. *Meyer, R. and Thring, R.H., "Mixture preparation measurements", SAE Technical Paper 950069, 1995. Doi: 10.4271/950069*

96. *Hill, P.G., "Cyclic variation and turbulence structure in spark-ignition engines", ombustion and Flame, vol. 72, no. 1, pp. 73-89, Apr., 1988.*

97. *J.F. Le Coz, "Cycle-to-cycle correlations between flow field and combustion initiation in an SI. Engine", SAE Paper no. 920517, 1992.*

98. *W. Cartellieri, F.G. Chmela, P.E. Kapus, R.M. Tatschl, "Mechanisms leading to stable and efficient combustion in learn burn gas engines", Proceedings of International Symposium COMODIA (1994).*

99. *S. Pischinger, J.B. Heywood, "How heat losses to the spark plug affect flame kernel development in an SI engine", SAE Paper no. 900021, 1990.*

100. *Lacour, C. and Pera, C., "An experimental database dedicated to the study and modelling of cyclic variability in spark-ignition engines with LES", SAE Technical Paper, no. 2011-01-1282, 2011.*

101. *Lee, K.H. and Kim. K., "Influence of initial combustion in SI engine on following combustion stage and cycle-by-cycle variations in combustion process", International Journal of Automotive Technology, 2(1): 25-31, 2001.*

102. Mantel, T., "Three dimensional sudy of flame kernel formation around a spark plug", SAE Technical Paper, no. 920587, 1992.

103. Galloni E., "Analyses about parameters that affect cyclic variation in a spark ignition engine", Applied Thermal Engineering ,29: 1131-1137, 2009

104. Long, E.J., Rimmer, J.E.T., Justham, T., Garner,C.P., Hargrave, G.K., Richardson, D. and Wallace, S. (2008)'The influence of in-cylinder turbulence upon engine performance within a direct injection IC engine', in Proc. of the 7th International Conference on Modeling and Diagnostics for Advanced Engine Systems, pp.213-220.

105. E. Abdi Aghdam, A.A. Burluka, T. Hattrell, K. Liu, C.G.W. Sheppard, J. Neumeister, and N. Crundwell, "Study of cyclic variation in an SI engine using quasi-dimensional combustion model", in Proc. of 2007 SAE World Congress, no. 2007-01-0939, April, 2007.

106. Abdel-Gayed, R.G., Bradley, D. and Lung, F.K.-K., "Combustion Regimes and the Straining of Turbulent Premixed Flames," Combustion and Flame 76: 213-218 (1989)

107. Abraham, J., Williams, F.A. and Bracco, F.V., "A Discussion of Turbulent Flame Structure in Premixed Charges," SAE Technical Paper no. 850345, 1985.

108. Peters, N., "Laminar Flamelet Concepts in Turbulent Combustion,", 21st Symposium (International) on Combustion, The Combustion Institute, pp 1231-1250, 1986.

109. Russ, S.G., Lavoie, G. and Dai, W., "SI engine operation with retarded ignition: Part 1 – cyclic variations", SAE Technical Paper, no. 1999-01-3506, 1999.

110. Dai, W, Russ, S.G., Trigui, N. and Tallio, K.V., "Regimes of premixed turbulent combustion and misfire modeling in SI engines", SAE Technical Paper, no. 982611, 1998.

111. Lee, T.K., Prucka, R.G. and Filipi, Z.S., "Real-time estimation of combustion variability for model-based control and optimal calibration of spark ignition engines", in Proc. of the

Institution of Mechanical Engineers, Part D (Journal of Automobile Engineering), vol. 223, no. D11, pp. 1361-1372, Nov., 2009.

112. Brehob, D.D., and Newman, C.E., "Monte Carlo Simulation of Cycle-to-Cycle Variability," SAE Technical Paper 922165, 1992.

113. Matthews, R.D., Sarwar, M.G., Hall, M.J., etc., "Predictions of Cyclic Variability in an SI Engine and Comparisons with Experimental Data," in Proc. of SAE International Fuels and Lubricants Conference, Toronto, Canada, 1991

114. Sjeric, M., Kozarac, D. and Taritas, I., "Experimentally supported modeling of cycle-to-cycle variations of SI engine using cycle-simulation model", SAE Technical Paper, no 2014-01-1069, 2014, doi: 10.4371/2014-01-1069.

115. Dai W., Trigui, N. and Lu, Y., "Modeling of cyclic variations in spark-ignition engines", SAE Technical Paper, no. 2000-01-2036, 2000.

116. ETAS official website

117. Turns, S., "An Introduction to Combustion: Concepts and Applications, 2nd Edition" McGraw-Hill, Boston, 2000.

118. Pitcher, G., "Multi-plane Airflow Measurements in the Cylinder of a Tumble Based Engine," SAE 2014-01-2705, 2014.

119. Jarvis, S., Justham, T., Clarke, A., Garner, C. et al., "Motored SI IC Engine In-Cylinder Flow Field Measurement Using Time Resolved Digital PIV for Characterisation of Cyclic Variation," SAE Technical Paper 2006-01-1044, 2006

120. Yu, R., Bai, X., Hildingsson, L., Hultqvist, A. et al., "Numerical and Experimental Investigation of Turbulent Flows in a Diesel Engine," SAE Technical Paper 2006-01-3436, 2006

121. Zeng, W., Sjöberg, M., and Reuss, D., "Using PIV Measurements to Determine the Role of the In-Cylinder Flow Field for Stratified DISI Engine Combustion," SAE Int. J. Engines 7(2):615-632, 2014

122. Rassweiler, G. M. and Withrow, L. Motion pictures of engine flames correlated with pressure cards. SAE Trans., 1938, 42, 185–204.

123. Xu, Z., Yi, J., Wooldridge, S., Reiche, D. et al., "Modeling the Cold Start of the Ford 3.5L V6 EcoBoostEngine," SAE Int. J. Engines 2(1):1367-1387, 2009

124. DeFilippo, A., Saxena, S., Rapp, V., Dibble, R. et al., "Extending the Lean Stability Limits of Gasoline Using a Microwave-Assisted Spark Plug," SAE Technical Paper 2011-01-0663, 2011

125. Livengood, J. C., Wu, P. C., "Correlation Of Auto-ignition Phenomena In Internal Combustion Engines And Rapid Compression Machines", 5th Symp. (Int.) on Combustion, p. 347, Reinhold Publishing Corp. (1955).

LIST OF ACRONYMS

A	Surface Area
AC	Alternative Current
A_{flame}	Flame Front Area
A_{flow}	Valve Flow Area
AFR	Air to Fuel Ratio
ANN	Artificial Neural Network
ATDC	After Top Death Center
Bm	Reference Fitting Constant
BTDC	Before Top Death Center
$B\phi$	Fitting Constant
CAD	Crank Angle Degree
CFD	Computational Fluid Dynamics
CFM	Coherent Flame Model
COV	Coefficient of Variation
CPDC	Cylinder Pressure Development Controller
Cv	Specific Temperature at a Constant Volume
CA00	Start of Combustion Crank Angle Location
CA50	50 Percent of Mass Burned Crank Angle Location
C_1	Residual Backflow Constant
C_2	Trapped Residual Constant
C_3	Constant in Turbulence Intensity Model

D_e	Exhaust Valve Diameter
$D_{FlameKenel}$	Duration for Flame Kernel Development
D_i	Intake Valve Diameter
DMT	Density Modifier Term
DPIK	Discrete Particle Ignition Kernel
deg	Degree
dmb	Mass Burned for One Time Step
dme	Mass Entrained for One Time Step
dh	Integration Height Step Size
dt	Time Step
ECL	Exhaust Valve Camshaft Phasing Centerline
ECU	Electronic Control Unit
EGR	Exhaust Gas Recirculation
E_{SP}	Energy from Spark
EVC	Exhaust Valve Closing (defined @ 0.15mm of lift)
FFM	Full Field Modeling
FTP	Federal Test Procedure
GCA	Gas Exchange and Combustion Analysis software
HSPIV	High Speed Particle Image Velocimetry
h	Distance to Flame Center
hc	Convective Heat Transfer Coefficient
IC	Internal Combustion

ICL	Intake Valve Camshaft Phasing Centerline
IMEP	Indicated Mean Effective Pressure
IVO	Intake Valve Opening (defined @ 0.15mm of lift)
k	Constant in Woschni Heat Transfer Model
k_0-k_5	Calibration Constants in Flame Kernel Development Model
L	Characteristic Length Scale
L_e	Exhaust Valve Lift
LES	Large Eddy Simulation
LHV	Lower Heating Value
L_i	Intake valve Lift
L_0	Characteristic Length Scale at CA00
MAP	Manifold Absolute Pressure
MBT	Maximum Brake Torque
MB20	20 Percent of Total Mass Burned
MB60	60 Percent of Total Mass Burned
MFB	Mass Fraction Burn
M_{fuel}	Fuel Mass
M_{MAP}	Manifold Pressure Effect Multiplier
M_{Pi_OL}	Multiplier for Intake Pressure during Overlap
MPS	Mean Piston Speed
$M_{u'}$	Turbulence Intensity Multiplier
m_b	Burned Mass

m_{burned}	Mass Burned
m_e	Entrained Mass
m_{ex}	Exhaust Flow Mass
m_{in}	Intake Flow Mass
m_{total}	Total Mass In Cylinder
$m_{trapped}$	Trapped Residual Gas Mass in Cylinder
$m_{unburned}$	Unburned Gas Mass
N	Engine Speed (rev/sec)
NVH	Noise, Vibration and Harshness
n_{comb}	Polytropic Coefficient during Combustion
n_{comp}	Polytropic Coefficient during Compression
OF	Overlap Factor
OF_{ns}	Overlap Factor (non-RPM/speed dependent)
OF_s	Overlap Factor (RPM/speed dependent)
OLC	Overlap Centerline
OLV	Overlap Volume
P	Turbulence Production Term
P_{cyl}	Cylinder Pressure
P_e	Exhaust Pressure
P_{eOL}	Exhaust Pressure During Valve Overlap
P_i	Intake Pressure
PiOL	Intake Pressure During Valve Overlap

P_{IVC}	Cylinder Pressure at IVC
$P_{IVC,MAP}$	Intake Valve Effect on P_{IVC}
P_{SPK}	Cylinder Pressure at Spark
P_0	Atmosphere pressure
Q	Heat Energy
Q_{fuel}	Heat Release from Fuel
Q_{ht}	Heat Transfer Loss
Q_w	Heat Transfer Loss
r_c	Engine Compression Ratio
R	Gas Constant
RCM	Rapid Compression Machine
RGF	Residual Gas Fraction
RGM	Residual Gas Mass
RMSE	Root Mean Squared Error
RSM	Reynolds Stress Models
RPM	Revolutions Per Minute
r	Flame Radius
r_b	Burned Gas Radius
SAE	Society of Automotive Engineers
SI	Spark Ignition
S_L	Laminar Flame Speed
$S_{Lcalibrated}$	Calibrated Laminar Flame Speed

$S_{L,0}$	Reference Laminar Flame Speed
S_{Lmodel}	Modeled Laminar Flame Speed
$Slope_{MAP}$	Manifold Pressure Effect on IVC Effect Slope
$Slope_{RPM}$	Engine Speed Effect on IVC Effect Slope
SOC	Start of Combustion
SPKT	Spark Timing
Te	Exhaust Gas Temperature
T_g	Gas Temperature
T_0	Atmosphere Temperature
$T_{unburned}$	Unburned Gas Temperature
T_w	Wall Temperature
UDDS	Urban Dynamometer Driving Schedule
V_b	Burned Gas Volume
V_c	Engine Clearance Volume
V_{cyl}	Instantaneous Cylinder Volume
V_d	Engine Displacement
V_{IVC}	Cylinder Volume at IVC
$V_{unburned}$	Unburned Gas Volume
WOT	Wide Open Throttle
u'	Turbulence Intensity
$u'_{calibrated}$	Calibrated Turbulence Intensity
u'_{CA00}	Turbulence Intensity at CA00

u'_{model}	Modeled Turbulence Intensity
ΔP_{eOL}	Overlap Exhaust Pressure Correction Term
ΔP_{iOL}	Overlap Intake Pressure Correction Term
$\alpha \; and \; \beta$	Laminar Flame Speed Fitting Constant
ρ_{CA00}	Mixture Density as CA00
ρ_{SPK}	Gas Density at Spark
$\rho_{unburned}$	Unburned Gas Density
ρ_{u0}	Unburned Gas Density at CA00
τ	Characteristic Timing
λ	Taylor Microscale
ξ	Constant (set to be 1)
ν	Kinetic Viscosity